

**Carbon nanofiber supported Pt nanoparticles with an
accurate size control through copolymer stabilization and
chemical reduction for PEM fuel cell application**

By

Mahdiah Shakoori Oskooie

Submitted to the Graduate School of Engineering and Natural Sciences

in partial fulfillment of

the requirements for the degree of

Master of Science

Sabanci University

Spring

2017

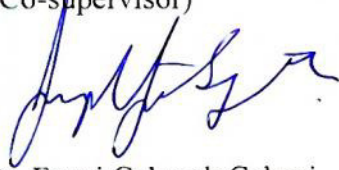
CARBON NANOFIBER SUPPORTED PT NANOPARTICLES
WITH AN ACCURATE SIZE CONTROL THROUGH
COPOLYMER STABILIZATION AND CHEMICAL REDUCTION
FOR PEMFC FUEL CELL APPLICATION

APPROVED BY:



Asst. Prof. Dr. Serkan Ünal
(Thesis Supervisor)

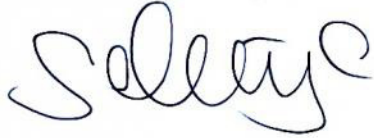
Dr. Serap Hayat Soytaş
(Thesis Co-supervisor)



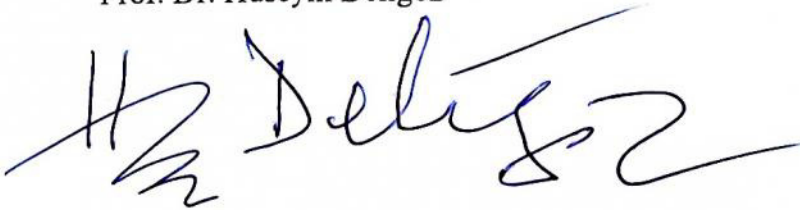
Assoc. Prof. Dr. Fevzi Çakmak Cebeci



Assoc. Prof. Dr. Selmiye Alkan Gürsel



Prof. Dr. Hüseyin Deligöz



DATE OF APPROVAL: 31/07/2017

© Mahdiah Shakoori Oskooie

All Rights Reserved

Abstract

A one-pot microwave-assisted synthesis method was developed to produce scalable carbon nanofiber (CNF) supported platinum nanoparticle catalysts through an in-situ polymer-based technique. CNF-supported Pt samples were synthesized through electrospinning of poly(acrylonitrile-*co*-N-vinylpyrrolidone) (P(AN-*co*-nVP)) copolymer containing PtCl₂ salt and consequent microwave reduction within hydrazine hydrate solution and carbonization. The aim of this study was to achieve a precise control on the size and distribution of the Pt nanoparticles by benefiting from a copolymer random templating and rapid microwave reduction. Prior to the application of microwave reduction on nanofibers, the pure effect of various carbonization temperatures (from 600 °C up to 1000 °C) on growth of Pt particles was studied. The carbonization at 800 °C was observed to represent a homogenous particle size distribution and the highest electroactive surface area (ECSA). Two types of samples were synthesized using microwave-assisted reduction – CNT-free and CNT-containing. The microwave irradiation for various time intervals (15s – 120s) was applied on both the CNT-free and the CNT-containing electrospun nanofibers with PtCl₂. By selectively changing the process conditions, the minimum average size of 1.751 nm in diameter was obtained in the case of CNT-free samples while 0.862 nm nanoparticles with a narrow size distribution was achieved for the CNT-containing samples for the first time. The mean Pt particle size was increased as a function of microwave irradiation time. The ECSA values obtained for CNT-free samples demonstrated a maximum activity for sample treated for 30 s, despite the smaller Pt particle size in the 15 s-treated sample. This behavior was attributed to the lower amount of accessible Pt particles on the fiber surface. In the case of CNT-containing samples the best catalytic activity (82.55 m²g⁻¹) was observed for 15s microwave reduction, which was hypothesized to be as a result of the significantly higher number of Pt cluster nucleated near the surface of the CNFs, a higher surface area due to the presence of CNTs and a higher electrical conductivity.

Keywords: Copolymer, electrospinning, platinum catalyst, carbon nanofiber, carbon nanotube, PEM fuel cell

Özet

Bu çalışmada, polimer-kökenli karbon nanofiber (CNF)/platin (Pt) nanoparçacık katalizör malzemelerin büyük ölçekli üretimini sağlayabilecek mikrodalga-esaslı bir yöntem geliştirilmiştir. CNF-destekli Pt katalizör örnekler, poli(akrilonitril-*co*-N-vinilpirrolidon) (P(AN-*co*-nVP)) ve PtCl₂ tuzunun birlikte elektrodokunması ve elde edilen nanofiber matlarının hidrazin çözeltisi içinde mikrodalga yardımıyla indirgeme ve sonradaki karbonizasyon işlemleriyle sentezlenmiştir. Bu çalışmanın amacı, kopolimerin Pt⁺ dağılımını sağlayacak yapısından ve mikrodalga yardımıyla ani indirgeme işleminde faydalanarak, Pt nanoparçacık boyut ve dağılımlarını kontrol edebilmektir. Mikrodalga ile indirgeme işleminden önce, karbonizasyon sıcaklığının (600 – 1000 °C) Pt parçacıklarının büyümesi üzerine etkileri incelenmiştir. Bu çalışma sonucu, 800 °C'deki karbonizasyon işlemi ile homojen parçacık dağılımı elde edilebildiği ve bu örneklerin, diğer sıcaklıklarda üretilen örneklerle karşılaştırıldığında, en yüksek elektroaktif yüzey alanına (ECSA) sahip örnekler olduğu gözlemlenmiştir. Mikrodalga yardımıyla iki tür örnek sentezlenmiştir: CNT-içermeyen ve CNT-içeren. Farklı sürelerde mikrodalga ışıması, her iki tür elektrodokunmuş nanofiber/PtCl₂ örneklerine uygulanarak nanoparçacık indirgemesi gerçekleştirilmiştir. Farklı süreç değişkenlerinin optimizasyonu sonucunda, CNT-içermeyen örnekler üzerinde ortalama çapı 1.751 nm olan, CNT-içeren örnekler üzerinde ise ortalama çapı 0.862 nm olan nanoparçacıklar başarıyla sentezlenmiştir. Ortalama Pt parçacık boyutunun uygulanan mikrodalga süresi ile arttığı gözlemlenmiştir. 15 s mikrodalga ışımasına maruz bırakılan örneklerde Pt parçacık boyutu daha küçük olmasına rağmen, 30 s işlem gören örnekler daha yüksek elektroaktif yüzey alanına sahiptir. Bu durum 15 s işlem gören örneklerde fiber yüzeyinde erişilebilir Pt parçacığının daha az olması ile açıklanabilir. CNT-içeren örneklerde ise en yüksek katalitik aktivite (82.55 m²/g) 15 s işlem görmüş örneklerde gözlemlenmiştir. Bu sonucun, CNT'nin de yardımıyla yüzeyde daha fazla Pt nanoparçacığının yer almasından ve elektriksel iletkenliğin daha yüksek olmasından kaynaklandığı düşünülmektedir.

Anahtar kelimeler: kopolimer, elektrodokuma, platin katalizör, karbon nanofiber, karbon nanotüp, PEM yakıt hücresi

To
my dear husband; Sina Abdolhosseinzadeh
and my family

Acknowledgments

I would like to express my deepest gratitude to my master thesis supervisors; Dr. Serap Hayat Soytaş, Dr. Serkan Unal and Prof. Dr. Yusuf Z. Mencilođlu, for their limitless patience and supports. During two years of working, not only I learned about the right way of research, but also, I could learn an even more worthwhile lesson of being tenacious and determined on my goals.

Furthermore, I would specially acknowledge dear Prof. Dr. Selmiye Alkan Gursel for her kind supports and endless helps about fuel cell performance of the catalyst materials and also various required experimental tests and materials. I also express thanks to Prof. Dr. Fevzi Cebeci for devoting his valuable time to give me suggestions to improve my work.

I also appreciate sympathetic supports and assistances of my friends Ali Ansari, Murat Gokhan Eskin, Damla Turanlı, Zeki Semih Pehlivan, Mirsajjad Mousavi, Ali Tufani, Sahl Sadeghi, Fuat Topuz and my husband Sina Abdolhosseinzadeh.

I should express my thankfulness to Sabancı University and all the faculty members, as well. It was a great honor and pleasure for me being as a member of Sabancı University's family and being able to work in a truly excellent academic environment.

This project was performed by a financial support granted by TUBITAK (Project no: 213M023). Therefore, I would also like to appreciate valuable supports of all the friends working at the TUBITAK Office.

Table of Contents

1. Introduction	1
1.1. Preventing nanoparticle agglomeration via polymer-assisted stabilization	5
1.2. Electrospinning of polymeric solutions	13
1.3. Proton exchange membrane fuel cell	15
2. Materials and experimental	24
2.1. Materials	25
2.2. Synthesis	25
2.2.1. Copolymer synthesis	25
2.2.2. Fiber preparation	25
2.3. Characterizations	27
2.3.1. Polymer characterization	27
2.3.2. Fiber characterization	28
2.3.3. Electrochemical Characterization	28
2.3.4. Fuel cell testing	29
3. Results and discussion	31
3.1. Polymer characteristics	32
3.2. Electrospinning parameters	35
3.2.1. Electrospinning of nanofibers without carbon nanotube	35
3.2.2. Electrospinning of nanofiber/carbon nanotube hybrid structures	36
3.3. Development of carbon nanofiber-supported Pt through carbothermal reduction	38

3.4. Development of Pt containing nanofibers through chemical reduction	49
3.4.1. Nanofibers containing 5 wt.% Pt	50
3.4.1.1. Effect of the reducing agent and the reduction time	50
3.4.1.2. Effect of microwave time and reducing agent	56
3.4.2. Samples with 20 wt.% Pt	57
3.4.2.1. Effect of microwave time and reducing agent	57
3.4.2.1.1. Ethyleenglycol, Sodium borohydride and Hydrazine	57
3.5. Microwave assisted reduced Pt in 20 wt.% Pt containing samples	61
3.6. Fuel cell testing	71
4. Conclusion	74
5. References	76

List of Figures

- Fig.1. Schematic image of a block copolymer, which is used to stabilize the nanoparticles. 7
- Fig.2. (a) SEM and (b) TEM images of the PVP nanofibers obtained from 47 wt.% PVP-0.5 wt.% AgNO₃. 8
- Fig.3. (a) SEM and (b) TEM images of the PVP nanofibers obtained from 47 wt.% PVP-15 wt.% AgNO₃. 9
- Fig.4. TEM images of the PVA nanofibers containing 5 wt.% of PVP-coated Ag nanoparticles with equivalent 0.5 wt.% of Ag within the nanofibers. 9
- Fig.5. TEM image and size distributions histogram of Au-(PEO-PPO-PEO), (scale bar=100nm). 10
- Fig.6. TEM images and size distributions of Au nanoparticles prepared through KBH₄ reduction in the presence of: a) PVP, b) PAN, and c) MMS-NVP. (Polymer/Au = 20:1 mol/mol, KBH₄/Au = 10:1 mol/mol, DMF/water = 9:1 v/v). 11
- Fig.7. SEM images of the PAN-AA-Pt nanofibers: (a) sample A, (b) sample B, (c) sample C, and (d) sample D. 13
- Fig.8. Schematic illustration of electrospinning system. 14
- Fig.9. Schematic illustration of PEMFC components. 16
- Fig.10. TEM images of the SC-CNFs/Pt containing: (a) 5 wt.%, (b) 10 wt.%, (c) 20 wt.% and (d) 30 wt.% of Pt. 18
- Fig.11. SEM micrographs of the (a) top surface of SC-CNF/Pt cathode, cross-section view of cathode layer with: (b) SC-CNFs/20 wt.%Pt (0.025 mg Pt/cm²), (c) SC-CNFs/5 wt.%Pt (0.025 mg Pt/cm²) and (d) SC-CNFs/20 wt.%Pt (0.2 mg Pt/cm²). 19
- Fig.12. PEMFC polarization curves of MEAs with different anode and cathode Pt/SC-CNFs electrode loading and catalyst loading. Test conditions: cell: 70 °C, 100% relative humidity; anode/cathode: H₂/O₂, 200/200 mL/min, 35/35 psi. 20

Fig.13. (A) SEM images of (a) CNF and (b) CNT. (B) TEM images of the Pt decorated (a) CNF and (b) CNT.	21
Fig.14. Fuel cell performances of catalyst materials before and after CV treatments, fuel cell test being performed at H ₂ and air flow of 0.4 and 2 ml/s respectively, at 70 °C.	22
Fig. 15. Schematic of CNF/Pt nanofiber synthesis.	26
Fig.16. (a) FTIR spectra of AN, n-VP and P(AN-co-nVP) copolymer and (b) high resolution FTIR characteristic stretching of C=O in P(AN-co-nVP) and P(AN-co-nVP) + PtCl ₂ .	33
Fig.17. (a) ¹ H NMR spectra of P(AN-co-nVP) as-synthesized copolymer, (b-d) schematic image showing the random copolymer and electrostatic interaction of Pt cations with polar groups of nVP.	34
Fig.18. SEM images of the electrospun nanofibers of P(AN-co-nVP)/5wt.% PtCl ₂ at different voltage applications.	36
Fig.19. SEM images of the electrospun fibers of P(AN-co-VPYR)/CNT-0.75% / PtCl ₂ -5% with different voltage applications.	37
Fig.20. TEM images of P(AN-co-nVP)- 5 wt.% PtCl ₂ - 0.75 wt.% CNT.	38
Fig.21. (a) ¹³ C-SSNMR spectr of electrospun fibers before and after carbonization at 600 °C, 800 °C and 1000 °C and (b) Raman spectra of carbonized samples at different temperatures.	39
Fig.22. SEM images of as-electrospun (a) and carbothermally reduced nanofibers at different temperatures; (b) 600 °C, (c) 700 °C, (d) 800 °C, (e) 900 °C and (f) 1000 °C. TEM (g) and HR-TEM (h) images of carbonized samples at 800 °C; (i) FFT pattern of the particles in (h).	41
Fig.23. Schematic images showing the sintering mechanism of Pt in nanofibers.	43
Fig.24. XRD spectrums of carbothermal reduced samples at various temperatures.	45
Fig.25. CV spectra of carbothermal reduced samples at various temperatures.	46

Fig.26. SEM image and EDX spectrum of as-electrospun nanofibers of P(AN-co-nVP)/5wt% PtCl ₂ .	51
Fig.27. SEM images and EDX spectra of P(AN-co-nVP)/5 wt.% PtCl ₂ nanofibers immersed in 5 vol.% hydrazine solutions for (a) 1 hour, (b) 24 hours.	52
Fig.28. SEM images and EDX spectra of P(AN-co-nVP)/5 wt.% PtCl ₂ nanofibers reduced in 10% hydrazine solution, (a) 1 hour, (b) 8 hours and (c) 24 hours.	53
Fig.29. EDX spectrum of P(AN-co-nVP)/5 wt.% PtCl ₂ sample reduced in 10% hydrazine solution, 116 hours.	54
Fig.30. SEM images of the carbonized samples at 800 °C containing 5 wt.% Pt reduced in 5 wt.% hydrazine hydrate solution for different periods of times.	55
Fig.31. XRD patterns of the carbonized samples at 800 °C containing 5 wt.% Pt reduced in 5 wt.% hydrazine hydrate solution for different periods of times.	55
Fig.32. P(AN-co-nVP)/5 wt.% PtCl ₂ reduced in 10% hydrazine solution, EDX spectrum, 46 hours (a) chemical reduction only, (b) chemical reduction + microwave buildup.	56
Fig.33. XRD patterns of 20 wt.% Pt samples reduced in hydrazine under microwave during four different periods of times.	57
Fig.34. XRD patterns of 20 wt.% Pt samples reduced in hydrazine under microwave during four different periods of times; (a) before and (b) after carbonization at 800 °C.	58
Fig.35. The typical TEM images of the 20 wt.% Pt sample reduced under microwave in hydrazine for 3 min.	58
Fig.36. (a) XRD patterns of 20 wt.% Pt samples reduced in ethylene glycol under microwave during four different periods of times after carbonization at 800 °C and (b) XRD patterns of 20 wt.% Pt samples reduced in sodium borohydride under microwave during four different periods of times after carbonization at 800 °C.	59
Fig.37. SEM images of three 20 wt.% Pt samples reduced three different reducing agents under 3 min microwave irradiation in hydrazine.	60

Fig.38. SEM images of microwave-assisted reduced CNT-free nanofibers in 5 % Hydrazine hydrate solution for(a) 15s, (b) 30s, (c) 60s, (d) 120s and CNT-containing samples reduced for (e) 15s, (f) 30s, (g) 60s and (i) 120s. 63

Fig.39. TEM images of microwave-assisted reduced CNT-free samples for (a) 15s, (b) 30s, (c) 60s, (d) 120s and TEM images of CNT-containing samples reduced for (d) 15s, (e) 30s, (f) 60s and (d) 120s. 65

Fig.40. (a) HR-TEM image showing the alignment of the SWCNTs through CNF; (b) FFT pattern of SWCNTs; (c) HR-TEM image of Pt atoms in the FCC structure of a single crystal Pt and (d) FFT pattern of FCC structure of Pt. 66

Fig.41. XRD spectrums of nanofibers (a) without and (b) with CNT and (c) Raman spectrums comparing the graphitization in nanofibers with and without CNT carbonized at 800°C. 68

Fig.42. CV spectra of fibers: (a) without and (b) with CNT. 69

Fig.43. (a) TEM image of the crushed carbon nanofibers to be used in the fuel cell electrodes, (b) SEM image of the surface of fuel cell cathode catalyst layer and (c) SEM image from the intersection of the fuel cell cathode catalyst layer. 72

Fig.44. Single PEMFC a) performance b) power density output curves of the microwave treated samples at various irradiation times. 72

List of Tables

- Table 1.** Information about carbothermal treated electrospun P(AN-co-nVP)/ Pt-20 wt.% samples. 49
- Table 2.** A summary of the samples studied and the conditions used in this study. 50
- Table 3.** Information about microwave treated samples with and without CNTs. 70

List of Symbols and Abbreviations

AIBN	2,2'-azo-bis(isobutyronitrile)
AN	Acrylonitrile
CNF	Carbon nanofiber
CNT	Carbon nanotube
DMF	Dimethylformamide
FT-IR	Fourier Transform Infrared
PAN	Polyacrylonitrile
n-VP	n- Vinyl pyrrolidinone
PVP	Poly(vinyl pyrrolidinone)
SCE	Standard Calomel Electrode
SEM	Scanning Electron Microscope
TGA	Thermogravimetric Analysis
TEM	Tunneling Electron Microscope

1. Introduction

Introduction

Platinum (Pt) with an exclusive catalytic activity for oxidation and reduction reactions has been intensively investigated in various applications including fuel cells [1]–[3]. Since the specific surface area of Pt has a key role in its performance, several studies have been conducted to decrease the size of Pt particles [4]. Nevertheless, obtaining a proper control on the catalyst particle size and distribution has always been one of the major issues for scientific community [5]. Most of the conventional methods for production of carbon-supported Pt materials, such as wet impregnation and chemical reduction techniques, do not usually offer a precise control on the size and dispersion of the particles as well as a strong bonding between particles and carbon support [4]. To address these drawbacks, several alternative methods such as sonochemical [6], [7] and microemulsion [8] techniques, which are capable of producing more uniform catalyst particles, have been developed. Although these techniques decrease the probability of agglomeration of produced particles, the need for achieving a reasonably isolated Pt clusters with a strong attachment to the carbon support remains unsatisfied. Free nanoparticles are always prone to reaggregate and lose their desired performances. Thus, an effective production method is required to both synthesize finer Pt nanoparticles and establish a strong interaction between the nanoparticles and the carbon support. It is found that, the most practical way is to employ polymer-based fabrication of catalytic nanocomposites to control the particle size [9]–[11]. So far, various types of polymers have been utilized to develop specific regular structures of polymer-metal particle nanocomposites [12], [13]. The polymeric framework either sterically stabilizes the metallic catalyst particles or electrostatically binds to the metal ions by forming ligands [11], [14]. Among several types of stabilizing polymers, polyethylene oxide (PEO) [9], [10] and polyvinyl pyrrolidone (PVP) [11]–[13], [15]–[17] have been the most frequently utilized ones. It is reported that PVP and metal cations form complexes through donation of lone pair electrons from carbonyl oxygen and nitrogen to metal cations [11]. Generally, the process of stabilizing metallic particles is reported to be carried out through two main procedures, entitled as “ex-situ” and “in-situ” [18]–[21]. In the case of the ex-situ method, synthesized metallic nanoparticles are dispersed within a polymeric solution right after production [22], [23]. The particles with a thin overlaying polymeric layer are then precipitated in a non-solvent. This method is more widely employed in

various applications, compared to its in-situ counterpart. Almost any type of metallic nanoparticles can be protected using various kinds of polymers since there is no need for chemical coordination and compatibility between particle precursor and the polymer [22], [23]. Although fine and uniformly distributed catalyst nanoparticles are produced through ex-situ process, the particles are prone to aggregate upon several uses or heat treatments [24], [25]. To avoid this problem, the in-situ method could be employed to achieve more control on the size and distribution of the nanoparticles [26]–[28]. In this approach, the nanoparticle synthesis and stabilization with a polymeric material are conducted simultaneously. Metal precursors create a chemical coordination with a functional polymer; therefore, they can uniformly distribute throughout the polymer and remain inside this polymer matrix (no precipitations). Upon application of a reduction procedure, the metallic clusters are locally produced while they are trapped within a polymeric skeleton. Therefore, their shape, size and distribution are significantly dependent on the composition and architecture of the carrying polymer. Copolymerization enables distribution of a specific polar monomer throughout another supporting polymeric matrix. In this case, the polar monomers can locally coordinate with the metal precursors and evenly distribute them within the supporting polymeric matrix. This phenomenon is known as “micellization”, which gives rise to a precise and effective isolation and dispersion of the catalysts [29]. During subsequent reduction, a noble metal supported polymeric structure could be achieved, with a narrow particle size distribution. By adjusting the input molar ratio of the monomers, the final architecture of the copolymer could be tuned (block, random and etc.) [30]. Therefore, the catalyst particles produced via in-situ method using an appropriate copolymer helps to make the particles considerably stable against aggregation. Consequently, the size and distribution of the particles could be accurately controlled in the atomic level by tuning of the structure of hosting copolymer. For fuel cell applications, it is necessary to have catalyst particles supported by a high surface area carbon material, such as carbon nanofibers (CNF) and carbon nanotubes (CNT). Therefore, polyacrylonitrile (PAN) was chosen in this study due to its high carbon yield and well electrospinnability and the vinylpyrrolidone (VP) units were randomly incorporated into this polymer to coordinate with metal precursors and disperse them throughout the AN matrix [31], [32]. The VP as a “bifunctional” monomer can coordinate with both organic and inorganic substances.

The vinyl ends can polymerize with AN units and on the other hand, O and N, existing in its 5-membered lactam end, electrostatically interact the metal cations [33].

Electrospinning is a versatile technique that can meet the primary needs of in-situ synthesis method in terms of producing applicable nanofiber. Electrospinning develops continuous long polymeric fibers through an electrically charged jet of polymer solution. As a result, a porous film, consisted of an interwoven web of continuous nanofibers, is achieved [34]. Since electrospinning is a quite fast and simple process to produce nanostructures, production of electrode materials with lower Pt loading for fuel cells can be achieved economically in industrial scale [35], [36]. It is stated that substituting conventional carbon particles with one-dimensional carbon nanomaterials (CNTs or CNFs) leads to a long-haul electron transfer in the electrodes; therefore, the catalyst utilization increases [37]. So far, numerous investigations have been devoted to the decoration of noble catalyst particles over CNTs or other carbonaceous materials; however, there are a limited number of documents allocated to the decoration of CNFs [38]. Amongst those few studies, there are only a few reports on the use of in-situ method [39]–[42]. In most of the in-situ based studies, scientists have only used a single polymer (PAN) structure rather than a copolymer to stabilize the catalyst particles. However, an even particle size distribution was not achieved using the PAN homopolymer [43], [44]. This signifies the significant role of the polar units within the copolymers for localizing the catalyst atoms. In a study by Demir et al. [5], using the in-situ technique, the PdCl₂ was distributed within the electrospun poly(acrylonitrile-*co*-acrylic acid) copolymer and reduced by hydrazine hydrate solution. It was found that, the size of Pt nanoparticles could be tuned using different amounts of acrylic acid functional groups and PdCl₂ in the primary solution. In another work, the effect of the molecular architecture of the copolymer on the size and distribution of the Au particles was investigated [45]. It was observed that, using diblock template of a poly(styrene-*b*-2-vinylpyridine) copolymer, an ordered array of Au nanoparticles of 6 nm in diameter and 30 nm apart from each other, could be achieved. Distribution of Pd nanoparticles throughout poly(styrene-*co*-acrylonitrile) copolymer was also studied and Pd nanoparticles in the particle range of 30-40nm were achieved [27]. Nevertheless, despite achieving a good control on distribution of the nanoparticles, the average particle size that could be obtained is not less than 3nm in all the reported studies. An efficient reducing protocol must be

developed to reduce the localized precursors in a shorter time not letting them to grow further. Therefore, the microwave-assisted techniques, which have always provided a rapid synthesis method in various areas, were utilized in this study.

1.1. Preventing nanoparticle agglomeration via polymer-assisted stabilization

Achieving a good control on the size and distribution of the synthesized nanoparticles, is one the most challenging topics due to their relatively high surface energy. In spite of various efforts to discover an effective method to take control over the size of synthesized nanoparticles, there is still a rising demand to develop precisely controllable techniques. One of the most effective strategies for overcoming sintering problem of the nanoparticles is the well-known polymer-assisted stabilization of the particles [44]. Applying a shell of polymer over the nanoparticles gives rise to the significantly decreased aggregation of nanoparticles, since a polymeric layer can satisfy the high surface energy of the particles. By simply tuning the molecular architecture of the polymers, especially through copolymerization or adjusting their molecular weight, it would be possible to control the size of the nanoparticles within the polymeric shell. Generally, there are two main strategies to control the size distribution of the nanoparticles by means of polymers. Firstly, the nanoparticles could be synthesized and then become dispersed within a polymeric solution and finally precipitating in a non-solvent solution (ex-situ method). Since, almost all types of nanoparticles could be stabilized by means of various polymers, the ex-situ technique is known as of the most continent method. For example, the Au covered with a polymer monolayer was reported. Spherical Au nanoparticles stabilized by grafted poly(N-isopropylacrylamide) (PNIPA) were synthesized via a controlled radical polymerization technique. The NIPA was started its polymerization from the surface of Au nanoparticles. The average diameter of the obtained Au nano-cores was about 3.2 nm [46].

In the second approach, the metal nanoparticle precursor can create a complex with the hosting polymer (copolymer) and subsequently be reduced by a desiring technique, while it is already entrapped within a polymeric matrix. This method that combines the nanoparticle synthesis and the nanoparticle coating into a single process is called “in-

situ” method. The in-situ methods have been getting a significant attention compared to the ex-situ technique, due to a better capability of controlling the size and distribution of the nanoparticles. In fact, the polymeric matrix acts both as a template for nanoparticle synthesis and stabilization. Once a copolymer is employed, the polar units in the copolymer establish a electrostatic binding with the surface of nanoparticle precursor and manage the desired distribution of the particles and on the other hand, the nonpolar polymeric units offer stabilization via steric bulk of their framework [9], [10] [11], [15]–[17]. For instance, polyvinylpyrrolidone (PVP) is one of the most well-known polymer that is frequently used to prevent particle aggregation, due to its ability to bind with metallic ions [13]. It was observed that the Pt nanoparticles produced with the aid of PVP have been considerably smaller than that of particles synthesized without PVP. Furthermore, it is reported that the catalysts particles produced this way demonstrate greater active surface area.

In the in-situ method, copolymers are utilized to control the arrangement of metallic catalysts on nanometer scale [47]. The specific architecture of copolymers can help the formation of an ordered arrangement for the nanoparticles as well as stabilization [48]. For instance, block copolymers, that are consisted of distinct blocks that bind to the nanoparticle surface or nanoparticle precursors and the other blocks that just manage the solubility and steric stabilization, have been recently reported [49]. This type of precise control over the growth of nanoparticles is called “nanoreactor” approach in which the polar block (unit) can localize the precursors to phase-segregated nanoscale regions (Fig. 1). In fact, the morphology and size of the provided nanoparticles could be adjusted through tuning of the size and shape of the “nanoreactors” via regulation of the composition and size of the utilized polymers [50].

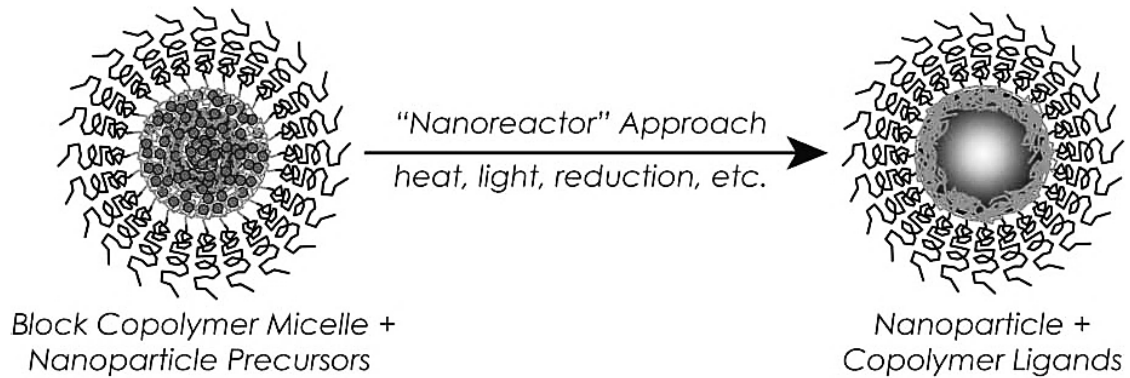


Fig.1. Schematic image of a block copolymer, which is used to stabilize the nanoparticles [47].

Monodisperse CdS nanoparticles with a controlled sizes were stabilized using a double-hydrophilic block copolymer of poly(ethylene glycol) and poly(ethylene imine). It was observed that the CdS nanoparticles were spread out as distinct units and represented a high oxidation resistance due to the protecting polymer layer. The size of the particles was observed to be adjustable from 2 nm to 4 nm based on polymer concentration and solvent type [51].

Based on the application, the polymer-stabilized nanoparticles can be produced in a bulk film or fiber format. To produce polymer/metal composite fibers in a nano or micro scale, the electrospinning method could be employed. In this regard, Yang [52] et al. produced a PAN nanofiber containing Ag nanoparticles by electrospinning of Ag precursor containing PAN solution. It was reported that, just by changing the molar ratio of the AgNO_3/PAN , the size of the Ag nanoparticles could be tuned in the range of 3.5nm-10 nm [31]. The average diameter of the polyimide fibers including silver trifluoroacetate was also reported to be reduced regarding the metal concentration. Also, the number of Ag nanoparticles was increased by increasing the amount of Ag precursor [32]. During another investigation, the PVP was utilized to stabilize Ag nanoparticles through two different ways. Firstly, the Ag containing PVP polymer solution was directly electrospun. The DMF was used both as a solvent of PVP and a reducing agent for Ag^+ ions. In the second route, first the PVP-coated Ag nanoparticles were synthesized and then dispersed in poly(vinyl alcohol) (PVA) solution and finally electrospun (5 wt.% of the PVP

containing Ag nanoparticles). The electron microscopy images of the PVP nanofibers presented in Fig. 2. The Ag nanoparticles were all spherical and in the range of 3.4 nm.

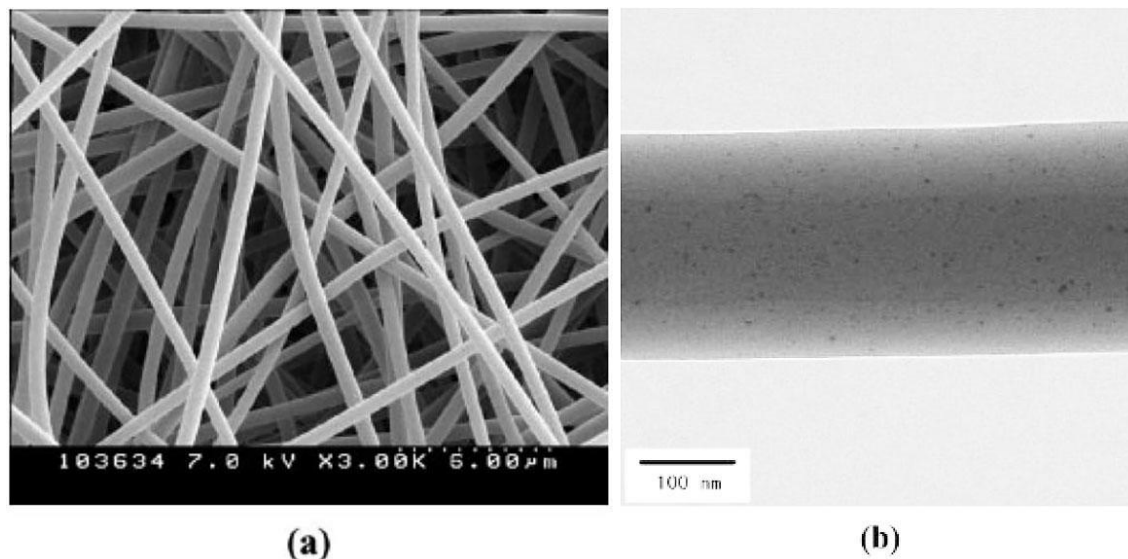


Fig.2. (a) SEM and (b) TEM images of the PVP nanofibers obtained from 47 wt.% PVP-0.5 wt.% AgNO₃ [53].

Fig. 3 also shows the electron microscopy images of the PVP nanofibers containing extremely higher amount of Ag precursor (15 wt.% of AgNO₃). It is observed that the average size of the nanofibers has reduced compared to the 0.5 wt.% Ag containing nanofibers, which was attributed to the increased charge density over the fibers during electrospinning [53]. The average Ag particle size was calculated to be 4.6 nm in these fibers, which suggested the ability of the PVP polymer to efficiently stabilize the Ag nanoparticles.

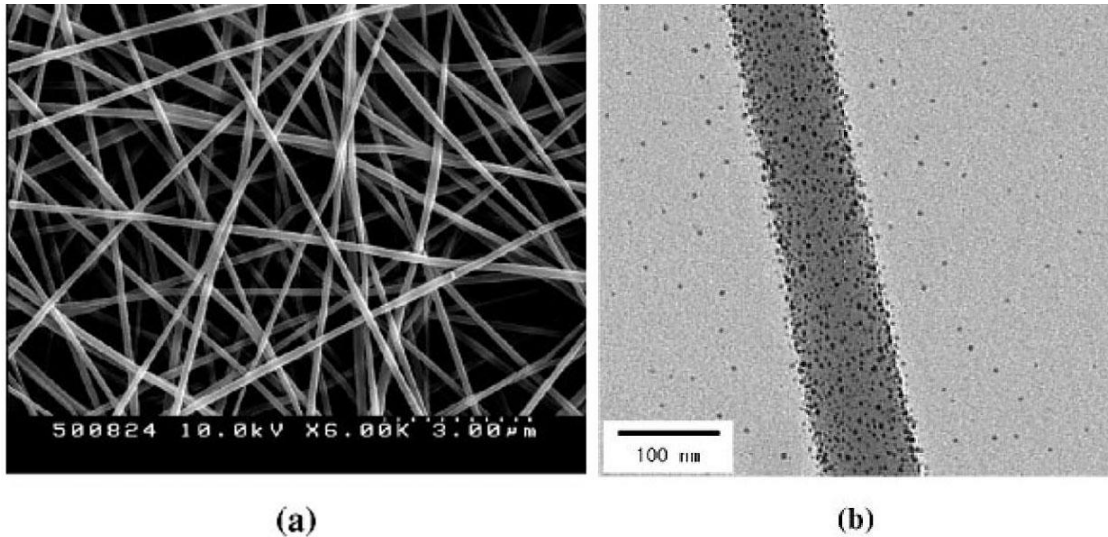


Fig.3. (a) SEM and (b) TEM images of the PVP nanofibers obtained from 47 wt.% PVP-15 wt.% AgNO₃ [53].

The PVA nanofibers including PVP-coated Ag nanoparticles could be observed in Fig. 4. In these fibers, the wt.% ratio of PVA/PVP-coated Ag is 95/5 and therefore, the overall amount of Ag is equivalent to 0.5 wt.%. It was observed that the Ag nanoparticles were uniformly scattered throughout the PVA nanofibers possessing a diameter of around 6 nm, slightly larger than that of the 47 wt.% PVP-15 wt.% AgNO₃ nanofibers. This phenomenon advocates the fact that the Ag nanoparticles were well-stabilized by PVP during electrospinning process. Furthermore, the final PVA nanofibers retain good mechanical properties.

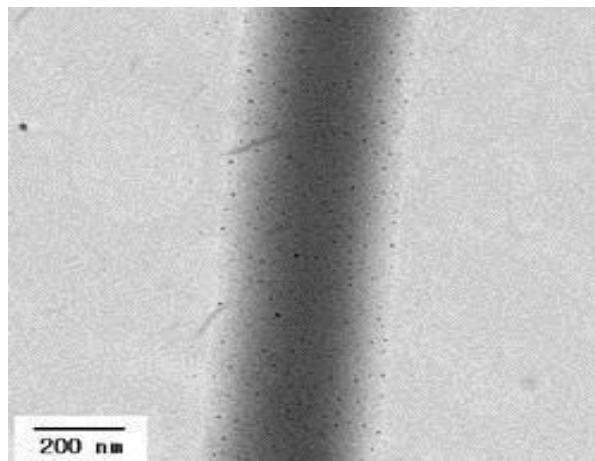


Fig.4. TEM images of the PVA nanofibers containing 5 wt.% of PVP-coated Ag nanoparticles with equivalent 0.5 wt.% of Ag within the nanofibers [53].

A single-step approach was devised to prepare Au nanoparticles (10 nm) out of $\text{HAuCl}_4 \cdot x\text{H}_2\text{O}$ through air-saturated aqueous solutions containing poly(ethylene oxide)-poly(propylene oxide)-poly(ethylene oxide) (PEO-PPO-PEO) block copolymer [54]. Overall molecular weight and relative block length of the block copolymer mainly controlled the formation of Au nanoparticles. Fig. 5 demonstrates the TEM image and the Au nanoparticle size distribution histogram. It is observed that the rounded Au nanoparticles in the sizes less than 8.3 nm were achieved.

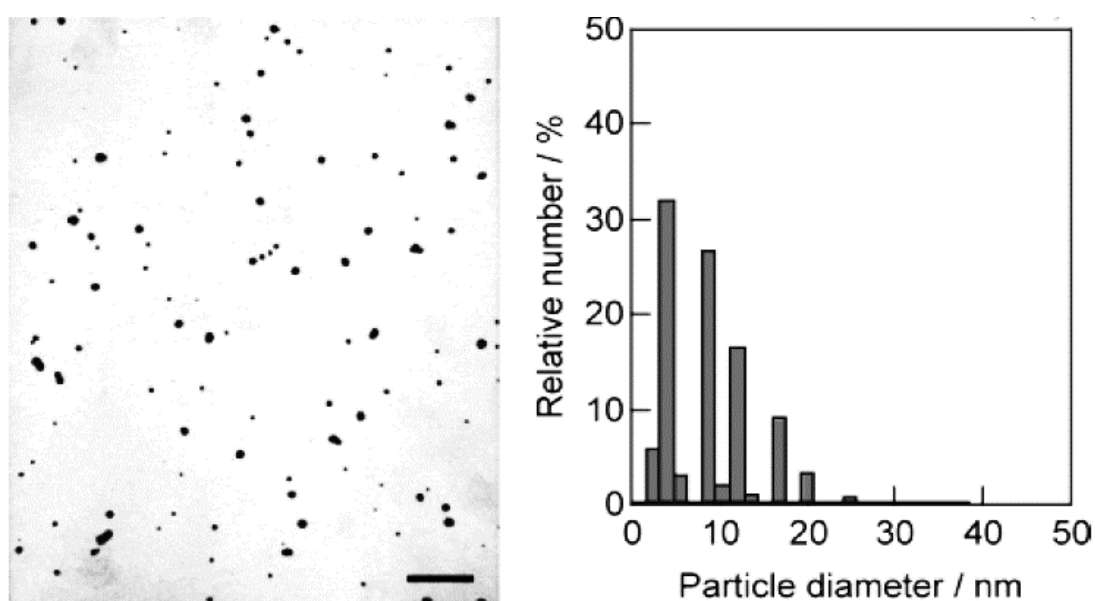


Fig.5. TEM image and size distributions histogram of Au-(PEO-PPO-PEO), (scale bar=100nm) [54].

Monodispersed Au nanoparticles (15-30nm) were produced using poly(mercaptopmethylstyrene-co-N-vinyl-2-pyrrolidone) (MMS-NVP) [55]. Production of Au nanoparticles was also compared with samples prepared using PVP and PAN polymers (Fig. 6).

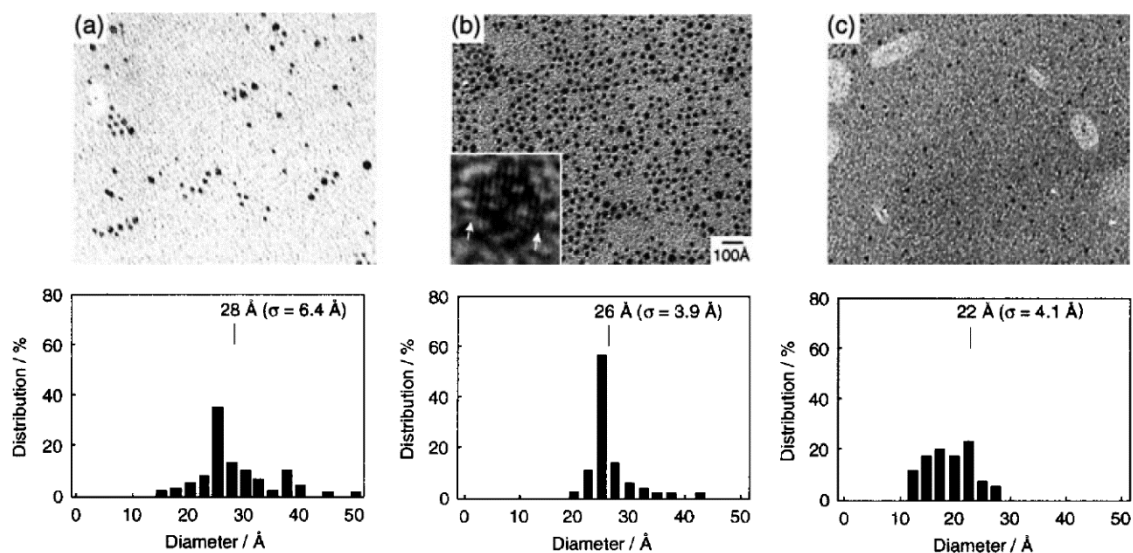


Fig.6. TEM images and size distributions of Au nanoparticles prepared through KBH_4 reduction in the presence of: a) PVP, b) PAN, and c) MMS-NVP. (Polymer/Au = 20:1 mol/mol, KBH_4/Au = 10:1 mol/mol, DMF/water = 9:1 v/v) [55].

The Au precursor was HAuCl_4 . It was found that finer Au nanoparticles could be obtained by accelerating the reduction rate of $[\text{AuCl}_4]^+$ ions by a polymer, such as PVP, to absorb these ions. Additionally, the Au nanoparticles with the size of around 20 nm were synthesized using KBH_4 reducing agent.

In addition to Au nanoparticles, due to the high importance of Pd and Pt nanoparticles in various applications such as fuel cells, these particles also were produced through stabilization by appropriate polymers or copolymers. For instance, poly(styrene-co-acrylonitrile) copolymer was employed to produce electrospun fibers containing Pd nanoparticles [27]. It was observed that the nanofibers with a diameter of 200 nm and the Pd nanoparticles of 30-40 nm were achieved. In a similar study, carbon nanofibers containing Pd nanoparticles were produced through electrospinning of polymeric solution/ PdCl_2 and the following thermal treatment in argon [110]. During an air-stabilization step at 300 °C, the Pd cations entrapped inside the electrospun PAN nanofibers were transformed to PdO nanoparticles smaller 10 nm. In another work, the production of Pd containing PAN nanofibers was also reported. The heat-treated PAN nanofibers at 500°C demonstrated a mean particle size of 40 nm [103]. In a study by Zhang et al. [111] Pd-Co containing PAN-based nanofibers were synthesized through

reduction by sodium borohydride and thermal treatments. It was observed that, by thermal treatment at higher temperatures, the final particle sizes were increased. The 8.9 nm nanoparticles in size, synthesized at 300°C, agglomerated to 13.8 nm at 700°C. Through another analogous study, carbon nanofibers supporting Pd nanoparticles by means of carbonization of electrospun PAN nanofibers embedding Pd(Ac)₂ precursor was synthesized [56]. Heat treatments demonstrated the reduction of Pd (carbothermal reduction) and aggregation into tiny particles within the nanofibers. The average size of nanoparticles was around 5nm. By heat treatment at 600°C, the size of Pd nanoparticles was increased to 15 nm. Through treatment at the 800°C, the Pd particle sizes were 30 nm and aggregated over the fiber surfaces. Upon heating till 1100°C, particles continued sintering on the fiber surfaces up to 50-350 nm.

To study the stabilizing effect of copolymers on nanoparticles, the Pd nanoparticles were synthesized via electrospinning of a copolymer of AN and acrylic acid (AA) containing PdCl₂ and subsequently reduced in hydrazine [5]. It was observed that, two or four crystallites were adhered together and formed agglomerate. The spherical Pd nanoparticles were distributed homogeneously on the electrospun nanofibers. It was reported that the Pd particle size is mostly depended on the amount of AA functional groups within the copolymer and also amount of PdCl₂. Larger Pd nanoparticles were produced by increasing the number of AA units and also PdCl₂ concentration in the copolymer. Fig. 7 shows the electron micrographs of fiber mats with Pd nanoparticles in bright contrast. Four samples were electrospun from solutions of equal polymer concentration including two different constituents. Solutions A, B, and D contain the same copolymer (5.4% AA), but PdCl₂ concentrations were different. Solutions B and C have equal amounts of PdCl₂; but they include polymers with different AA contents. It appears that Pd particle size depends on the amount of comonomer AA and PdCl₂ concentration in the initial solution.

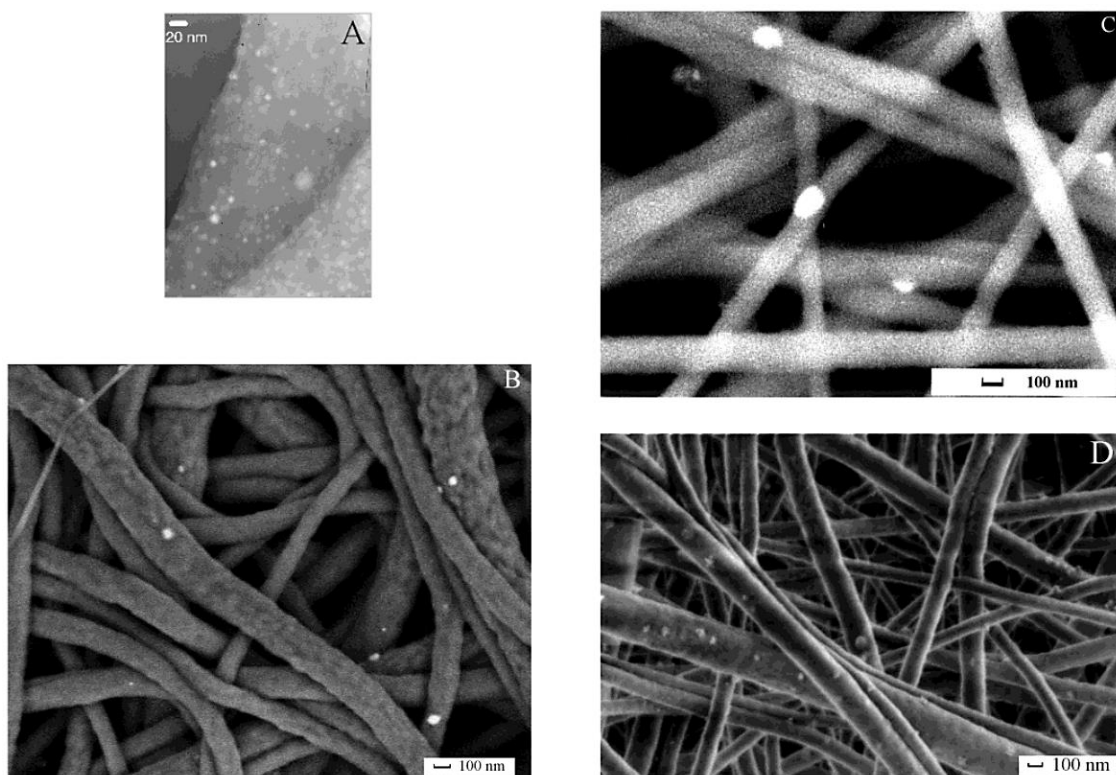


Fig.7. SEM images of the PAN-AA-Pt nanofibers: (a) sample A, (b) sample B, (c) sample C, and (d) sample D [5].

1.2. Electrospinning of polymeric solutions

Electrospinning as a versatile method to produce highly scalable nanoscale fibers has recently received a significant attention [34]. Taylor [57] as one of the pioneers in this field investigated the morphology of the polymer drip coming out of the needle tip. He found that it has a conical morphology and a jet could be instigated from its vertex. Therefore, since then, the cone drop at the tip of electrospinning needle was called as “Taylor Cone”. For spinning a material, it needs to be a “viscoelastic” material, so that become pulled into a long single strand. The basic aspects of an electrospinning system are demonstrated in fig. 8. Normally, in any typical electrospinning set-up there is one electrode which is attached into the polymeric solution container and the opposite electrode is connected to a grounded collector. Once, an extremely high voltage is applied, the charge repulsion at the surface of the liquid jet leads to a pressure against the surface tension of the fluid itself. By overcoming the created tension to the natural surface

tension of the fluid, its tip deforms to a Taylor cone. As, the intensity of the field on the Taylor tip exceeds a critical value, a jet of fluid will erupt, right at the apex of the Taylor cone and proceed to the gathering plate. The solvent evaporation during electrospinning of fibers leads to the formation of non-woven fiber mat.

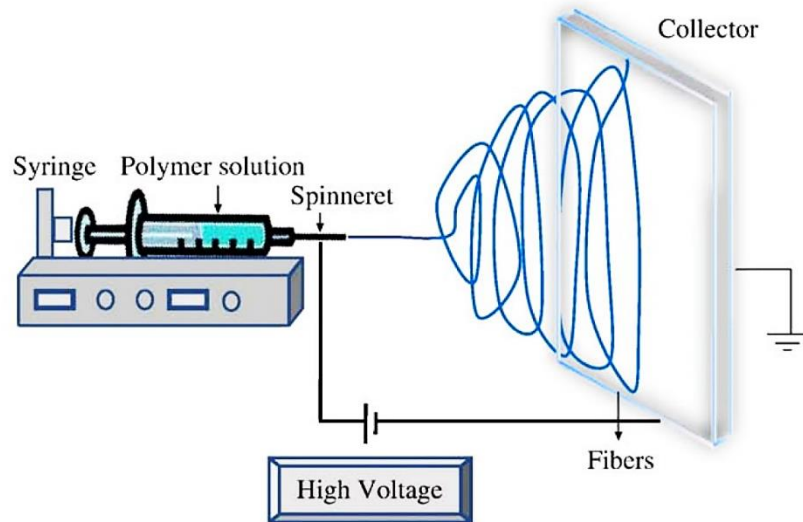


Fig.8. Schematic illustration of electrospinning system [60].

Properties of the polymeric solution play a substantial role in determining of the final fiber morphology. The surface tension of the fluid affects the probability of bead formation during electrospinning. The viscosity of the solution and its electric properties will also influence the elongation of the jet, directly dictating the diameter of the electrospun nanofibers. In fact, when the viscosity is low, the polymer chain entanglement is lower and the polymer jet breaks down into small droplets and causes beads formation. As the viscosity of the fluid increases, a gradual alternation in the form of the beads from round to spindle-like and then formation of a smooth fiber could be achieved [58]. It was reported that, the viscosity of the fluid has an important effect on the fiber diameter size and there is a power law relationship between solution concentration and its size [59].

Voltage provides the required energy to overcome to the surface tension of the fluid and draw it towards the collector in the electrospinning system may be compared to the impact that gravity has on a waterfall. The higher the implemented voltage, the greater the columbic repulsive force could be present in the polymer jet resulting in extra

stretching and enhance fiber formation [61]. It was observed that, there is an inverse relation between implemented voltage and fiber diameter [62]. The gap between the needle tip and the collector affects the fiber deposition time, the evaporation rate, and the whipping of the jet, which eventually affects the fiber properties. As the distance between the needle tip and fiber collector increases, the thickness of fibers decreases since the fibers are stretched throughout a long way. In some studies, it has been observed that, at extended distances, the diameter of the nanofibers usually increases because decreased electrostatic field strength results in reduced stretching in the electrospinning jet [63], [64]. However, as the distance increases too much, there is a possibility that the fibers cannot even reach the collector.

As another important controlling parameter, the flow rate of the polymeric fluid can affect jet velocity, material transfer rate and characteristics of resulting fibers. It was reported that, fiber diameter and the pore diameter increases with an increase in the polymer flow rate [65].

1.3. Proton exchange membrane fuel cell

Generally, the existing fuel cells could be categorized into five groups, called as solid oxide, phosphoric acid, alkaline, molten carbonate and proton exchange membrane fuel cell (PEMFC). Normally, most types of fuel cells convert H_2 and O_2 into electrical energy. Like other devices, various types of fuel cells have their specific pros and cons. It is possible to claim that, the PEMFCs are the known as the simplest type of the fuel cells, in terms of implementation. Therefore, the ease of usage of PEMFCs and also its availability in the market have attracted the most attention from the research and development community. As one the outstanding characteristics of fuel cells, one can refer to their high energy-conversion efficiency (up to 60%) [66].

The fundamental features of a typical PEMFCs is illustrated in Fig. 9. Normally, a PEMFC has two catalyst layers in its anode and cathod electrodes which has a seperating proton exchange membrane in between. The proton exchange membrane is actually a polymeric material which can only transfer the protons and is insulating for the electrons. The electrode which takes the hydrogen fuel in is called the anode and the electrode connected to the oxygen gas is named as cathode. The main products of the fuel cell

reaction are electrical current and water, which should be gathered through two complicated backplates, which can also help to dissipate heat in the high-power cells. To obtain a high performance from the fuel cell, the backplates must be in a good contact with the catalyst layer. To meet this necessity, a carbon paper is placed between the catalyst layer and the backplate. This paper provides both electron conducting and gas/water transfer duties.

Generally, the PEMFC electrodes are based on carbon particles (e.g., Vulcan XC-72 carbon black), which are decorated with Pt particles. An excessive catalyst loading in these electrodes is generally required due to the fact that, all the loaded catalyst particles are not accessible. The cost of precious metallic catalysts has been a serious barrier against commercialization of PEMFCs [35], [67]. To address this issue, recently a significant number of investigations has been devoted to devising PEMFCs functioning with less than 0.05 mg.cm^{-2} catalyst loading, which still is not realized [68].

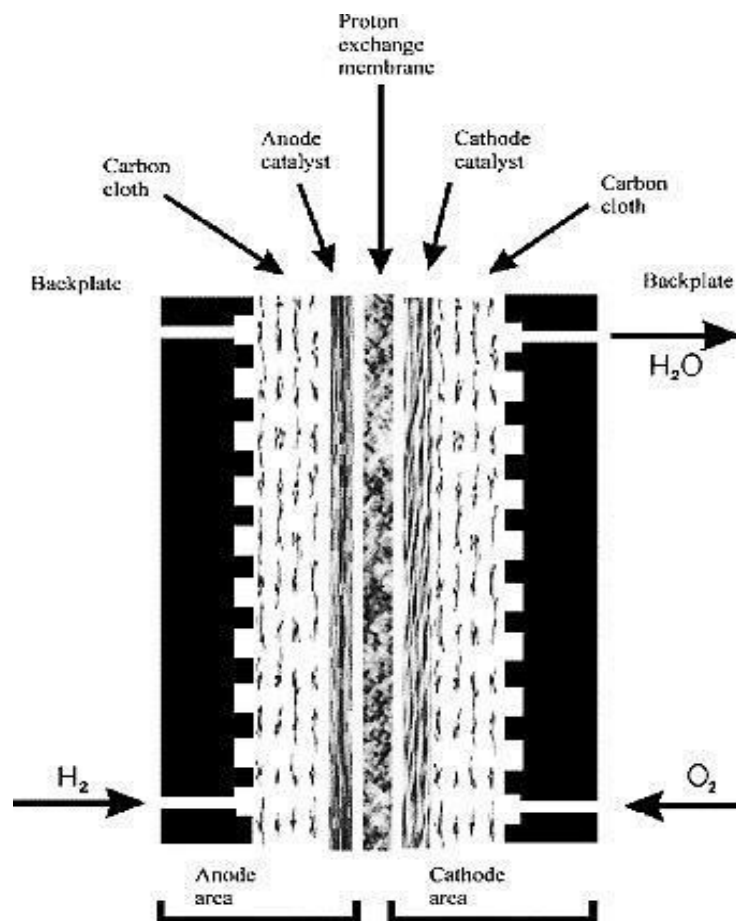


Fig.9. Schematic illustration of PEMFC components [66].

Numerous studies have revealed that, replacing the carbon particles with either one-dimensional (CNTs or CNFs) or two-dimensional (graphene) carbon structures, is likely to offer a powerful long-range electron delivery in electrodes and deduced catalyst loading [69]. Some research studies have reported deposition of noble metallic particles over CNTs for PEMFC applications [38].

However, just a limited number of studies are carried out on the application of CNFs in fuel cell electrodes. Because of the fascinating structural, thermal, electrical, mechanical properties and also ease of scalable production, CNFs could be potential future materials to be used in PEMFCs [70]. Stacked-cup carbon nanofiber (SC-CNF) supported Pt nanoparticles were produced by a modified ethylene glycol method, with a loading range of 5 to 30 wt.% (Fig.10) [71].

It was observed that, the average size of Pt nanoparticles increases as a function of Pt precursor amount and a minimum of 5 nm was obtained. A special self-developed filtration process was used for producing the Pt/SC-CNFs MEAs. It was found that the Pt/SC-CNFs MEAs with an optimized 50 wt.% Nafion content demonstrated a higher performance compared to the carbon black-based MEAs with an optimized 30 wt.% Nafion content. This performance was associated to the high aspect ratio of SC-CNFs, which can conveniently create continuous conducting networks within the Nafion matrix, compared to the carbon black particles. For the SC-CNFs/Pt nanofibers containing 5 wt.%, 10 wt.% and 20 wt.%, 2 nm-3 nm Pt particles were observed being evenly distributed over the SC-CNFs as shown in TEM images in Fig. 10. The Pt concentration was also observed to increase by increasing the Pt loading in the samples.

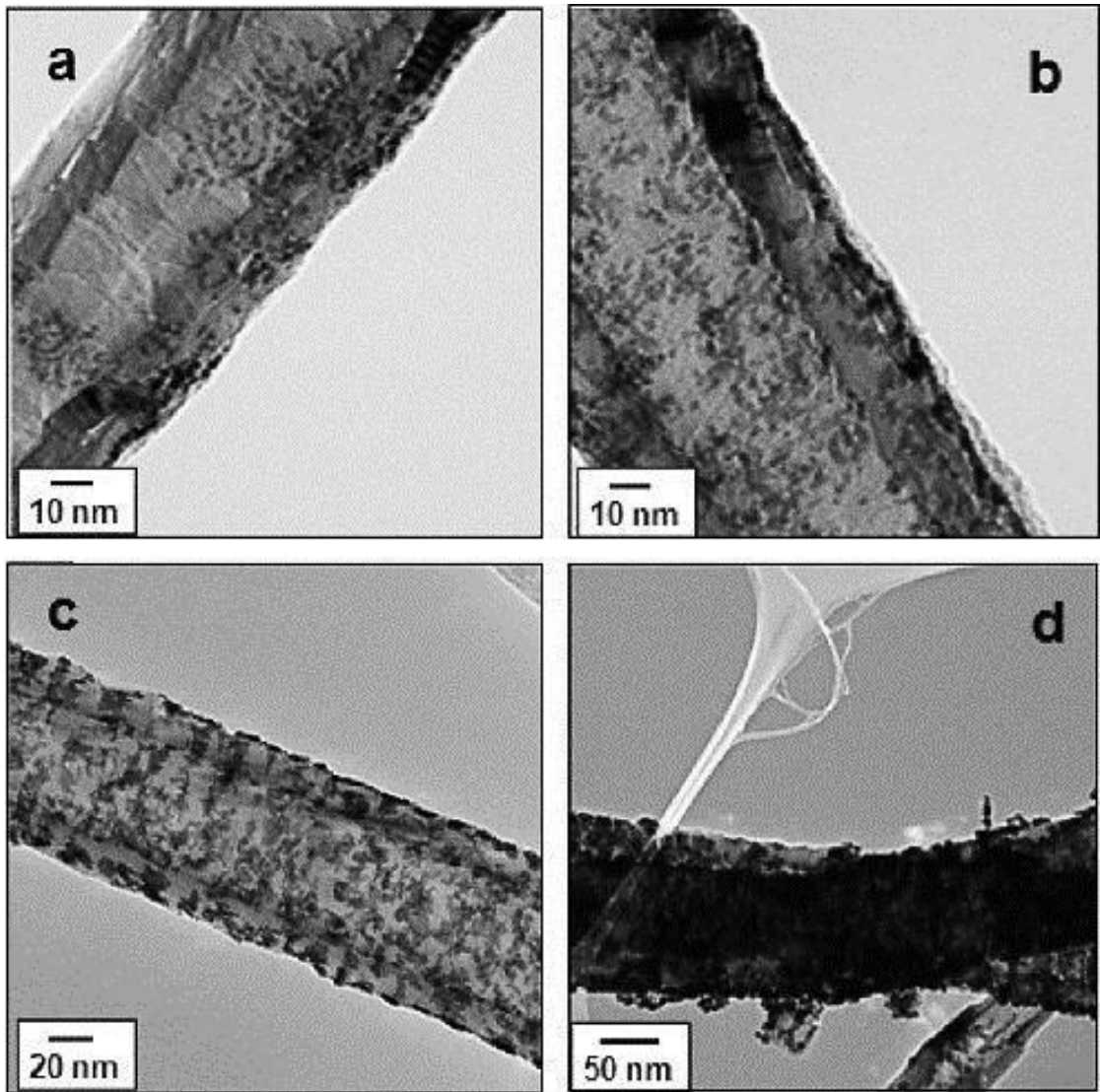


Fig.10. TEM images of the SC-CNFs/Pt containing: (a) 5 wt.%, (b) 10 wt.%, (c) 20 wt.% and (d) 30 wt.% of Pt [71].

The cross sectional SEM images from the SC-CNF/Pt cathode electrodes containing various portions of Pt loadings are demonstrated in Fig. 11. Regarding the SEM images, it was observed that the nanofibers have been randomly oriented in the catalyst layer, which is in contrast to a former work on Pt/MWNT cathodes with partially oriented MWNTs [72].

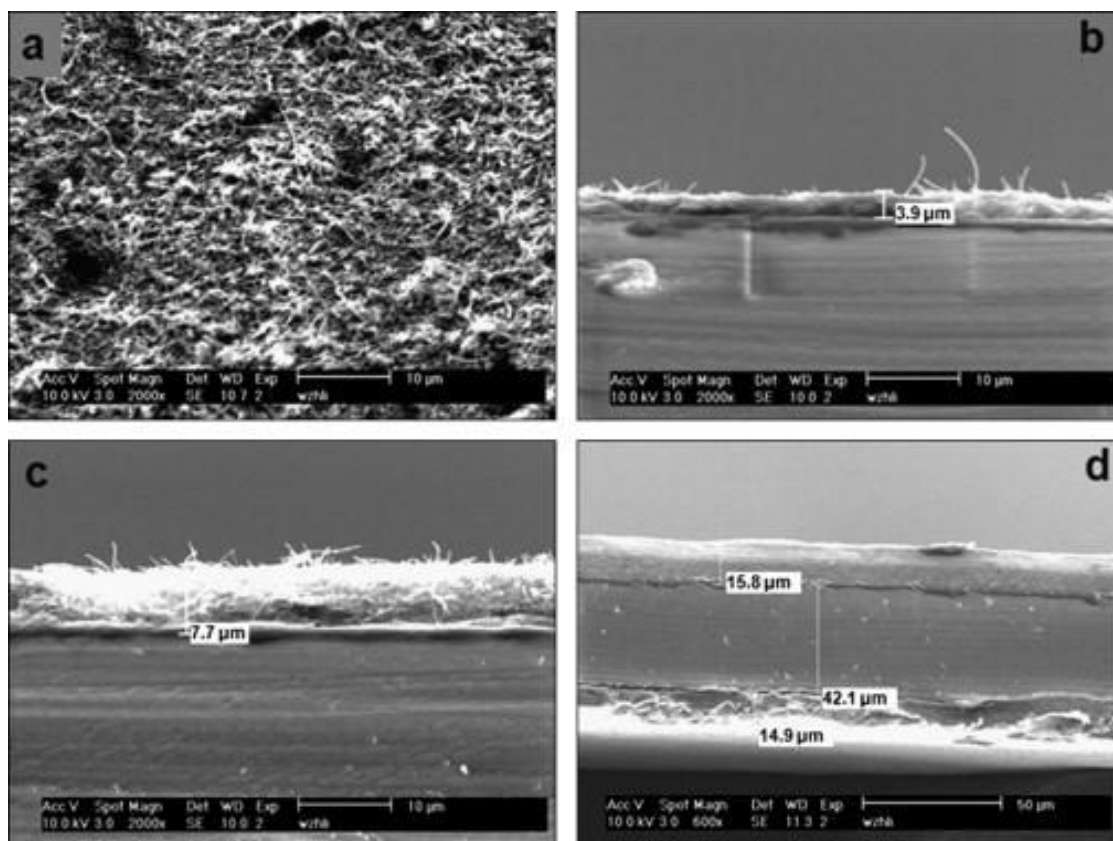


Fig.11. SEM micrographs of the (a) top surface of SC-CNF/Pt cathode, cross-section view of cathode layer with: (b) SC-CNFs/20 wt.%Pt (0.025 mg Pt/cm²), (c) SC-CNFs/5 wt.%Pt (0.025 mg Pt/cm²) and (d) SC-CNFs/20 wt.%Pt (0.2 mg Pt/cm²) [71].

The single cell performances of the 4.4 cm² Pt/SC-CNFs samples, with anode and cathode loadings of 0.2, 0.05 to 0.025 mg Pt/cm² and 0.2 to 0.1 mg Pt/cm², respectively, are demonstrated in Fig. 12.

It was reported that, by reducing the Pt loading in the anodes from 0.2 mg/cm² to 0.025 mg/cm² (maintaining the Pt loading on the cathodes identical for all samples, 0.2 mg/cm²), the performance of the fuel cell did not change considerably at low current region. Nevertheless, in the high current densities there was a relatively significant variation of 50 mV from the anode loaded with 0.05 mg Pt/cm² compared to the 0.2 mg Pt/cm² sample. Such a declined performance in fuel cell system could be attributed to the tubular architecture and also being highly packed. For another set of samples, consisted of anodes loaded by 0.05 mg Pt/cm² from 20 wt.% fibers a higher active region and also

improved mass transport due to the thinner catalyst layer, a considerable fuel cell performance was observed.

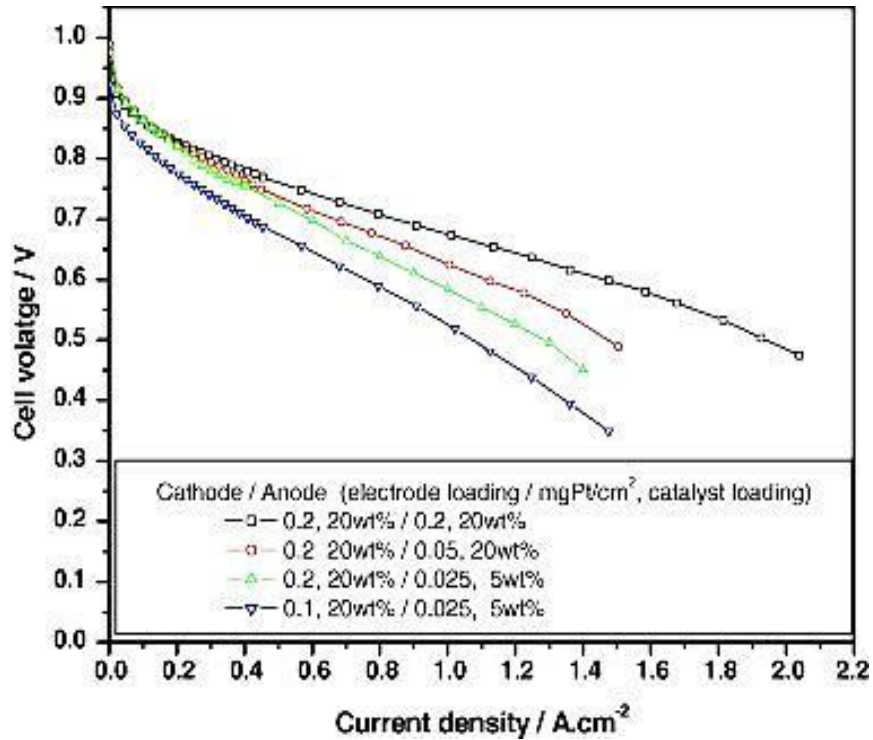


Fig.12. PEMFC polarization curves of MEAs with different anode and cathode Pt/SC-CNFs electrode loading and catalyst loading. Test conditions: cell: 70 °C, 100% relative humidity; anode/cathode: H₂/O₂, 200/200 mL/min, 35/35 psi [71].

Durability of the synthesized catalyst materials being used in long-term PEMFC applications is another considerable object that requires enough investigations. also, another issue that requires attention in PEMFC research [73]. Losing catalyst surface area because of carbon corrosion in supporting material is one of the essential degradation issues in PEMFCs. Pt loaded CNF and CNT (by polyol method) were used to prepare cathodes for the PEMFCs (Fig.13). The samples generally represented a high stability compared to the conventional carbon black.

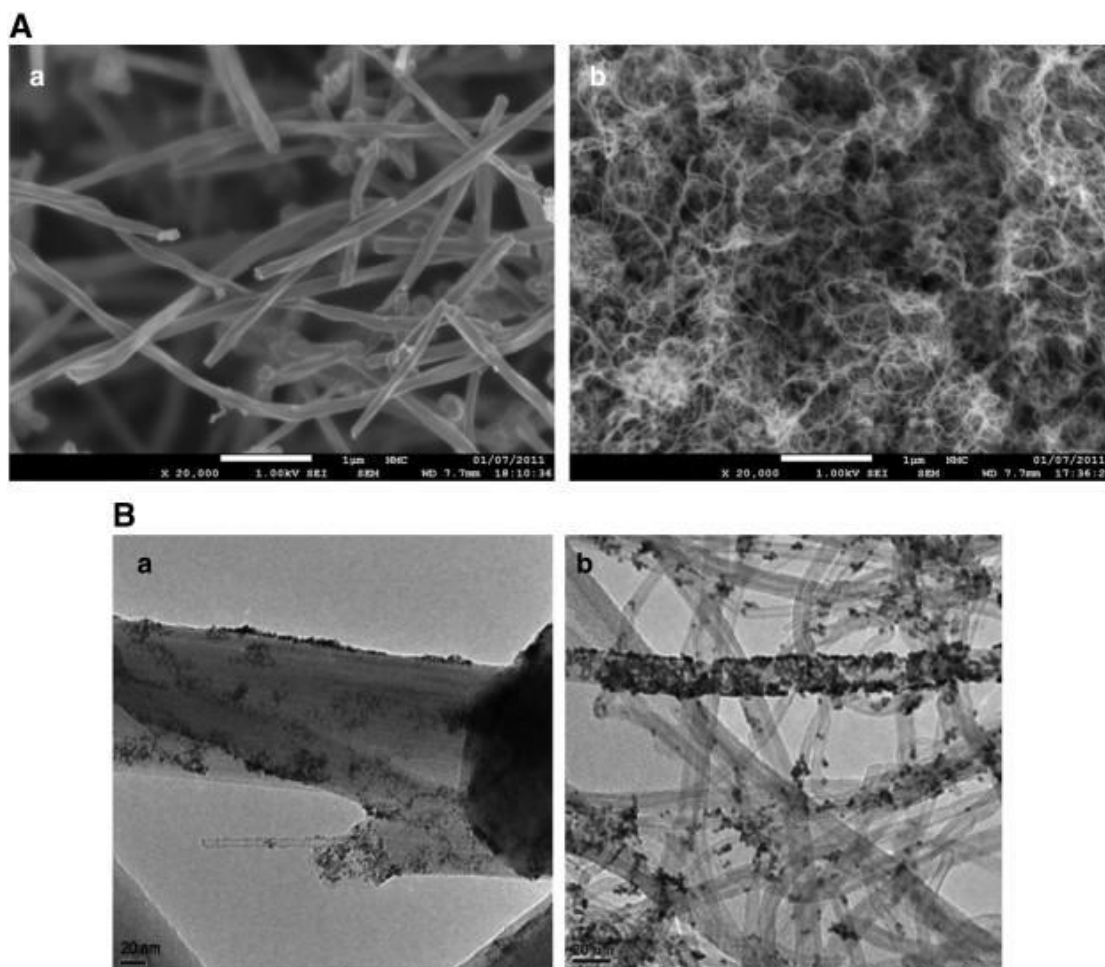


Fig.13. (A) SEM images of (a) CNF and (b) CNT. (B) TEM images of the Pt decorated (a) CNF and (b) CNT [73].

The single cell performance of the samples represented through polarization curves are shown in Figs. 14. It could be observed that, the CNT and CNF based electrodes exhibited a 20% and 42% boost in the max power density after cycling more than 5k (in CV test). However, considering an identical condition, the Vulcan-based cells have represented 20% decrease.

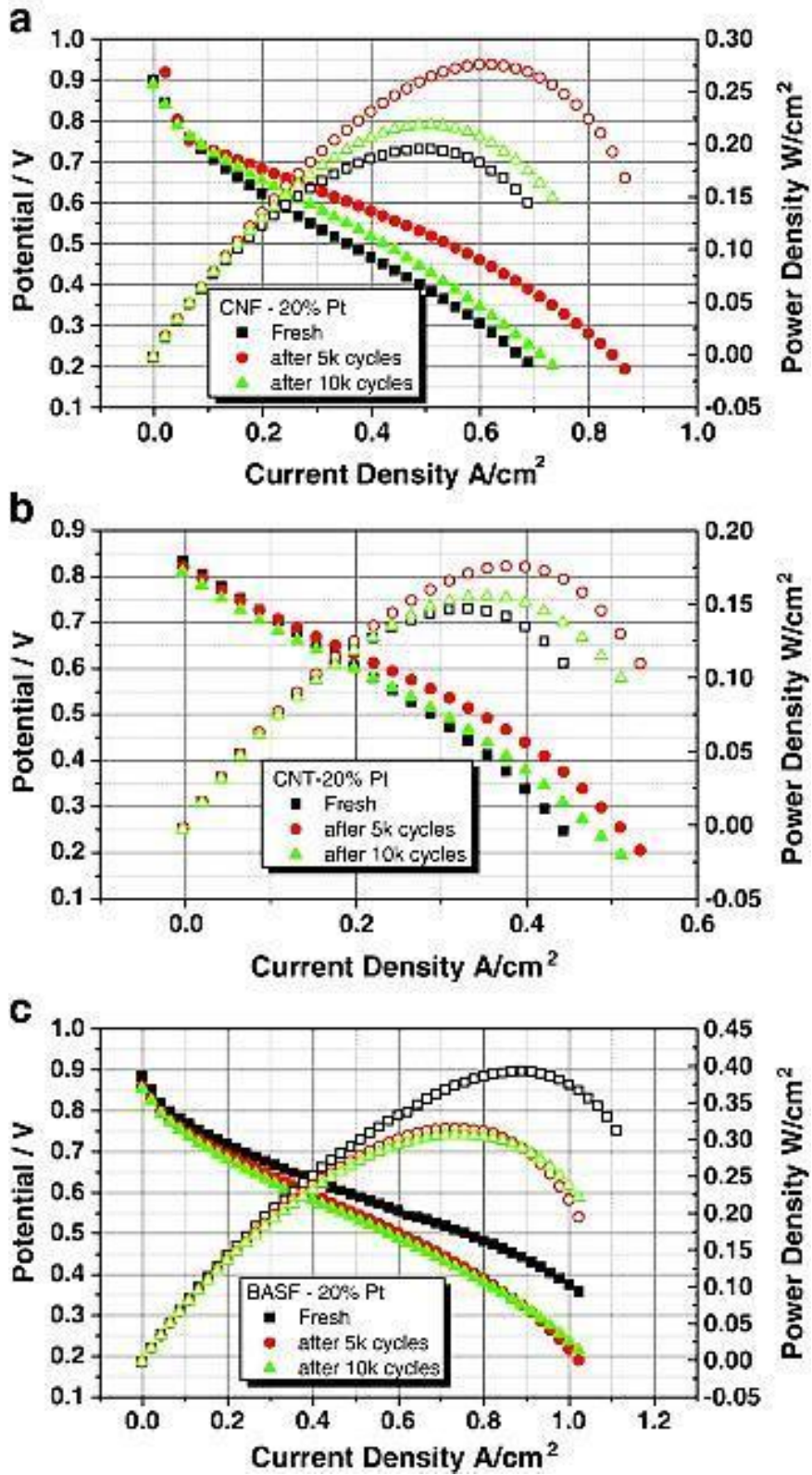


Fig.14. Fuel cell performances of catalyst materials before and after CV treatments, fuel cell test being performed at H₂ and air flow of 0.4 and 2 ml/s respectively, at 70 °C [73].

Due to the urgent necessity of replacing fossil fuels in the recent years, various alternative energy conversion systems have been developed. As mentioned, one of the most promising routes to produce green electrical energy is fuel cell technology. Among various types of fuel cells, the PEMFCs are most feasible version to be used in the cars and houses. Generally, the electrode materials of these fuel cells are made of a carbon support which contains Pt catalyst particles. Although, the PEMFCs are extremely user-friendly and efficient systems to produce energy, the production costs are too high so that it prevents the commercialization of these fuel cells. One important factor causing high production costs is associated with the carbon support itself and the other is related to the expensive catalyst materials such as Pt. In order to address these issues, in this study we tried to develop a simple method to produce highly scalable carbon support materials (carbon nanofibers) while controlling the size of Pt nanoparticles down to less than 1 nanometer to achieve higher performance with smaller amount of the catalyst. Therefore, we first stabilized the Pt precursors throughout the structure of a copolymer and then applied a microwave-assisted reduction protocol to reduce the Pt nanoparticles as they are trapped within the copolymer. Although some studies related with the polymer assisted nanoparticle synthesis have been recently carried out, an effective reducing protocol has not been utilized in any of them. Therefore, the particle sizes have not been precisely controlled and the achieved sizes were always bigger than 3 nm. Furthermore, there is a lack of comprehensive study on the electrochemical, catalytic and fuel cell performances of the carbon nanofiber based catalyst materials. Therefore, in this study the effort was focused to produce a cost-effective and high-performance material for fuel cell applications.

2. Materials and experimental

2.1. Materials

Acrylonitrile (AN, MW = 53.1 g mol⁻¹) and N-Vinylpyrrolidone (nVP, MW= 111.14 g mol⁻¹, Sigma-Aldrich) were purchased from Aldrich. Azobisisobutyronitrile (AIBN, Sigma-Aldrich) was used as initiator after being crystallized in acetone. Anhydrous N,N-dimethylformamide (DMF, Sigma-Aldrich) and deionized water were used as solvent for polymerization and solution preparation for electrospinning. Platinum (II) chloride (PtCl₂, MW = 265.99 g/mol, 99.9 % metal basis Alfa Aesar) was used as platinum precursor. Hydrazine hydrate solution (N₂H₄, MW = 32.05 g/mol⁻¹, Sigma-Aldrich), ethylene glycol (C₂H₆O₂, Sigma-Aldrich) and sodium borohydride (NaBH₄, Sigma-Aldrich) were utilized as reducing agents. Single walled carbon nanotubes (SWCNT, OCSIAL, Tuball, d = 1.6±0.4 nm, l >5 μm) were also used to reinforce the nanofibers. Nafion® solution (Sigma-Aldrich) was used in sample preparation for cyclic voltammetry tests.

2.2. Synthesis

2.2.1. Copolymer synthesis

The solution copolymerization of AN with nVP monomer was conducted in the DMF: deionized water (DIW) (1:1) at 60 °C for 5h. The amount of nVP was 2.5 mol% of total monomers (20 g AN and 1.02 gr nVP). The radical initiator AIBN (0.0634g) was added to the reaction with 0.1 mol% of the total monomers. The resulting product was precipitated in ethanol. The precipitated copolymer (Fig. 6II) was dried in a vacuum oven at 60°C until stationary weight.

2.2.2. Fiber preparation

The electrospinning solution was prepared by dissolving the 5 wt.% PtCl₂ and 20 wt.% PtCl₂ salt (with respect to the copolymer amount) in DMF along with 40 μL fuming HCl acid through stirring for 2h at 50 °C (Fig. 15II). A clear light orange solution was obtained by completely dissolving the salt in DMF and 7 wt.% p(AN-co-nVP) copolymer (with respect to the DMF amount) was added to the resulting solution. The solution was continuously stirred for further 2h at 50 °C to obtain a virtually clear light-yellow

solution. The change of the color of the solution from orange to the light yellow was assumed to be as a result of the complete electrostatic coordination of the platinum ions with the vinylpyrrolidone groups of the copolymer (Fig. 15IV). With the aim of investigating the effect of addition of carbon nanotubes, 1 wt.% SWCNT with respect to the copolymer was dispersed in DMF through sonication for 10h in a 40 kHz MRC DC150H sonicator. In parallel, the clear solution of copolymer and PtCl_2 solution was prepared as previously mentioned (Fig. 15V). Both CNT ink and polymer solution were mixed together and sonicated for extra 10 h to obtain a homogeneous suspension.

The electrospinning was carried out at room temperature by applying a high voltage of 15 kV between a stainless-steel syringe needle (0.5 mm inner diameter) and a grounded square collector (15 cm \times 15 cm) covered with aluminum foil (Fig. 15VI) situated 15 cm apart from the syringe tip. The syringe was pushed by an automatic pump at a flow rate was 0.5 ml/h. The electrospun fiber mats were dried in a vacuum oven at 60 °C for 12h to evaporate any residual DMF.

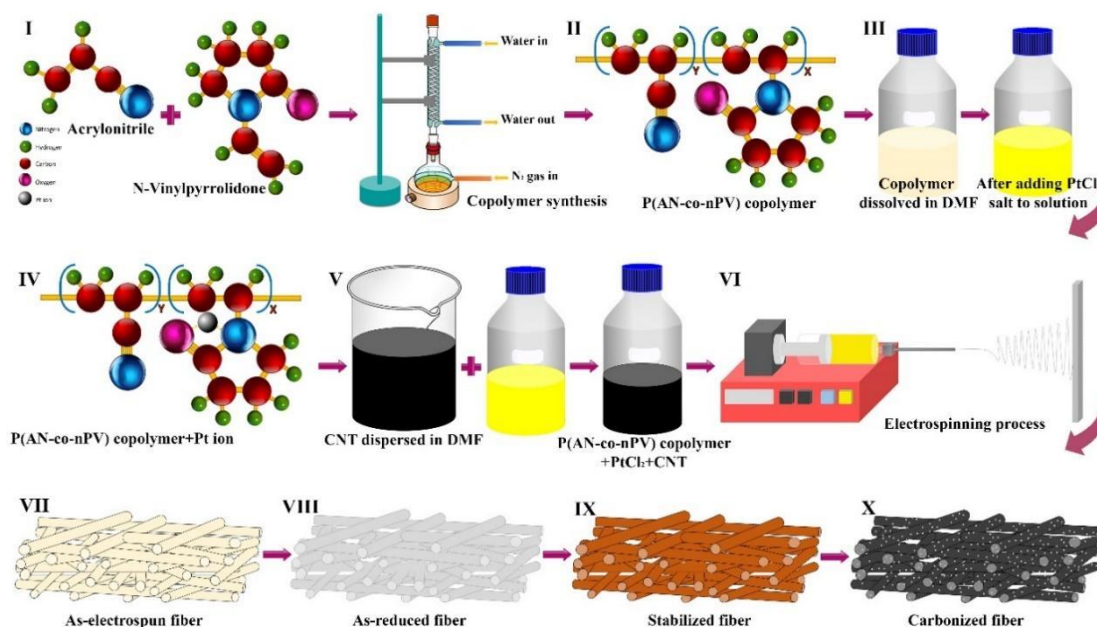


Fig.15. Schematic of CNF/Pt nanofiber synthesis.

Microwave assisted reduction within a 5 vol.% aqueous hydrazine solution and also ethylene glycol (100%) and sodium borohydride were carried out to reduce the PtCl_2 to Pt nanoparticles. The reduction of the samples was conducted in monowave 300 microwave reactor (Anton Paar GmbH). The microwave irradiation with a fixed power of 250 W along with in situ stirring (300 rpm) was exerted for 15s, 30s, 60s and 120s. For each microwave reduction period (15s, 30s, 60s and 120s) precise on/off intervals were defined for the microwave reactor so that the irradiation was stopped for 10s after every 5s of irradiation. The microwave-reduced samples were washed and vacuum filtered using DIW for several times until pH of the water was neutral. Some of the electrospun P(AN-co-nVP)/Pt-20 nanofibers were directly carbonized without any chemical reduction for comparison. PtCl_2 was carbothermally reduced to form nanoparticles.

The electrospun nanofiber mats were stabilized at 200°C with a rate of 5°C/min under air and carbonized at different temperature (600°C, 700°C, 800°C, 900°C and 1000°C) with a heating rate of 10°C/min under argon. The reduced samples went through the same heating procedure and carbonized at 800°C, which was the optimized temperature based on the previous experiments.

2.3. Characterizations

2.3.1. Polymer characterization

Fourier Transform Infrared (FTIR) spectra were recorded with Bruker Equinox 55 FTIR spectrometer with Attenuated Total Reflectance (ATR) attachment. ^1H Nuclear magnetic resonance (NMR) spectra were recorded in deuterated dimethylformamide (DMF-d_6) or dimethyl sulfoxide (DMSO-d_6) with Varian Inova 500 NMR spectrometer. Polymer molecular weights (MW) ($M_n = 122,500 \text{ g/mol}$, $M_w = 400,000 \text{ g/mol}$) were determined by size exclusion chromatography (SEC) using Viscotek TDAmx equipped with refractive index (RI), viscometer (VIS) and right-angle scattering/low angle scattering (RALS/LALS) detectors and three columns (Viscotek D5000, D3000 ve D1000).

2.3.2. *Fiber characterization*

¹³Carbon NMR solid-state spectrum (¹³C-SSNMR) was recorded with Varian Inova 500 NMR spectrometer. The graphitization degree of carbonized samples was investigated with Raman spectroscopy (Renishaw in Via Raman Spectrometer with visible excitation at 532).

The morphology of the fiber mats and the size and distribution of the Pt nanoparticles over the nanofibers were studied with Gemini 35 VP Field Emission Scanning Electron Microscope (SEM). Average fiber diameter was measured in all the samples by considering the size of at least 50 representative nanofibers. Transmission Electron Microscopy (TEM) analyses were conducted on JEOL JEM-2000FX TEM. The mean diameter size of the Pt particles was determined using Image J software based on averaging of more than 400 size measurements. The high resolution TEM microscopy (JEOL JEM-ARM200CFEG UHR TEM) was conducted to confirm the presence of graphitic structures in the nanofibers. The FFT patterns were also obtained using TEM characterizations in order to approve the crystallinity of the Pt particles. X-ray diffraction patterns (XRD) of the samples were studied using a Bruker AXS Advance D8 XRD instrument. Thermogravimetric analyses (TGA) were carried out using a Netzsch STA 449 C Jupiter simultaneous thermal analyzer with a sensitivity of 0.1°C. The electrical conductivity of the carbonized nanofibers was measured using a probe instrument. Surface area measurements were carried out based on N₂ gas absorption at 77 K using the Brunauer-Emmer-Teller (BET) model.

2.3.3. *Electrochemical Characterization*

The catalytic performance of the nanofiber-Pt composites was investigated with the cyclic voltammetry (CV) measurements with Gamry Reference 3000 Potentiostat/Galvanostat using a three-electrode cell system in which the catalyst ink was coated on top of a platinum (diameter of 3 mm, surface area 0.07065 cm²) electrode as the working electrode, Pt wire was used as counter electrode and Ag/AgCl as reference electrode. A catalyst ink of various types of nanofibers (4 mg/mL) in isopropyl alcohol (IPA) was prepared. The Nafion (20%) solution (0.5 micro liter Nafion/1mL IPA) was added to the materials and the slurry was sonicated for 15 min. 1 μL of the resulting

homogeneous ink applied onto the platinum working electrode was dried at room temperature for 20 min. Cyclic voltammograms were obtained with a potential scan range of -0.3V to 1.3 V at a scanning rate of 50 mV s⁻¹ in 30 min under N₂ gas purge. All the CV tests were carried out in a 0.1 M sulfuric acid solution and performing at least 20 stabilization cycles prior to the CV tests.

2.3.4. Fuel cell testing

In order to prepare an appropriate catalyst material to be used as a catalyst layer in PEMFC, the synthesized CNF/Pt was manually crushed using a mortar and pestle. These crushed shorter fibers were aimed to be used in the cathode side of a single PEMFC set-up. In the anode side, a standard electrode made up of commercial Vulcan (XC72) catalyst material was used. The as-crushed nanofibers were mixed with 30 ml mgPt⁻¹ Nafion ionomer solution (5wt.% Nafion in water) and 60 ml mgPt⁻¹ isopropyl alcohol (IPA) and sonicated for 15 min and consequently stirred for 45 min to achieve a homogenized slurry. Then the slurry was carefully bladed on a gas diffusion layer (GDL) of the size of 4*2.5 cm² and left to be dried in the ambient temperature. The cathodes were prepared for samples with and without CNT microwave treated for 15s, 30s and 60s. The overall Pt loading was maintained identical in all of the samples equal to 0.8 mg cm⁻². For preparing the standard anodes from the commercial Vulcan dispersion was electrospayed over the GDLs. To prepare the Vulcan ink, a mixture of PVDF-c-HFP, Nafion ionomer solution and Vulcan powder was homogenized and electrospayed. In the electrospaying ink, the solid/solvent ratio was maintained 15:85 (w:w) and the weight ratios of Vulcan: Nafion: PVDF-c-HFP were fixed at 65:23:12. The PVDF-c-HFP was first dissolved in DMF by stirring for 48 h and then Nafion solution and Vulcan were sonicated for 1 h. Subsequently, the PVDF-c-HFP/DMF solution and the Nafion/Vulcan dispersion were mixed together by stirring for another 48 h. The ink was filled within a syringe and electrospayed on carbon papers (GDL, AvCarb MGL190 with 190 μm thickness) at a flow rate of 0.1 mL min⁻¹ under an applied voltage of 15 kV by a Gamma High Voltage Power Supply (ES30P). Eventually, the electrodes were dried for 24 h at room temperature.

The membrane electrode assemblies (MEAs) were put together through the hot pressing of the cathode and anode electrodes having a pre-conditioned membrane (Nafion NR211) in between at 120 °C under 533.8 kPa for 5 min. The prepared MEAs were assembled to a single fuel cell test set-up working at the 70 °C under a 100 % relative humidity. The oxygen and hydrogen gases were delivered into the system with the stoichiometric ratios of 2 and 1.5, respectively. The fuel cell test was conducted via Scribner 850E fuel cell test system and testing cell through precisely machined tiny serpentine channels on the graphite flow fields. The fuel cell tests were conducted in a Scribner testing system at 70 °C with a 150 kPa back pressures. After achieving a steady state condition in the galvanostatic mode, the current/voltage results were recorded.

3. Results and discussion

In this study, with the aim of obtaining an optimal condition for the synthesis of the carbon nanofiber-supported Pt particles with a precise size control, various samples containing several portions of Pt were examined under numerous reducing conditions. Various process variables were optimized in the electrospinning technique. Different reducing conditions were also developed using different reducing agents under several immersion times or applying microwave irradiation and also carbothermal reduction. The necessary characterization techniques such as SEM, EDX, TEM, TGA, XRD and CV were employed to obtain the best performance among numerous samples. The cyclic voltammetry (CV) conditions were optimized and the Pt catalyst activity was observed and the electroactive surface area is calculated. As a result of these characterizations, it was observed that the samples obtained by microwave irradiation in hydrazine aqueous solution for several seconds contained homogeneously dispersed Pt nanoparticles of 0.8-4 nm in diameter. In the case of carbothermal reduction as the second selected method, the nanoparticles in the range of 1.7-8 nm in diameter were observed, but with a wider size distribution. It has been observed that as the temperature of the carbonization increased, the nanoparticle sizes grow and were directed to the CNF surface.

It could be claimed that, the Pt nanoclusters with a carbon nanofiber support, targeted at the less expensive and more efficient operation of high cost Pt catalyst for PEMFC electrodes have been produced in the planned frame of this project.

3.1. Polymer characteristics

The FTIR analysis was performed to characterize the formation of the P(AN-co-nVP) copolymer (Fig. 16a). In the FTIR spectrum of the AN, its characteristic peaks corresponding to the C=C (1630 cm^{-1}) and C \equiv N (2228.96 cm^{-1}) are recorded. In the case of the nVP monomer, the strong absorption band at 1671 cm^{-1} attributed to the C=O bond, the characteristic peak at 1628 cm^{-1} related to the double bond C=C stretching vibration, and a peak at 1424 cm^{-1} representing the characteristic absorption of methylene end were also observed. The FTIR spectrum of the P(AN-co-nVP) copolymer demonstrated the characteristic absorption vibrations coming from both AN and nVP. The carbon double-bond (C=C) was completely disappeared, indicating a complete copolymerization.

The effect of the addition of platinum salt into the copolymer was also studied using FTIR characteristic peak of the carbonyl (C=O) group of the P(AN-co-nVP) copolymer, coordinating with the platinum ions. Presence of an electrostatic interaction between polymer and a metal ion leads to the changes in the absorption frequency of the interacting groups [74]. As it is seen in the high-resolution carbonyl pick represented in Fig. 16b, the position of the C=O stretching was shifted from 1673 cm⁻¹ to 1659 cm⁻¹ after addition of PtCl₂ into the polymer.

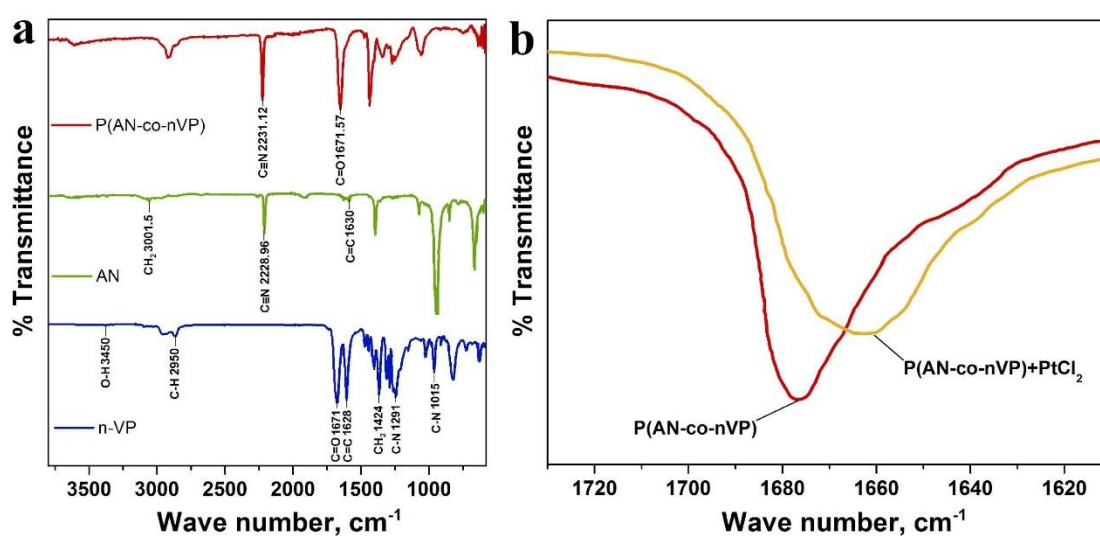


Fig.16. (a) FTIR spectra of AN, n-VP and P(AN-co-nVP) copolymer and (b) high resolution FTIR characteristic stretching of C=O in P(AN-co-nVP) and P(AN-co-nVP) + PtCl₂.

The molecular architecture of the copolymer was studied by ¹H-NMR spectroscopy (Fig. 17a). In the ¹H-NMR spectrum, the characteristic resonances located around $\delta = 4.3$ ppm (**D**) and at $\delta = 3.15$ ppm (**B**) were attributed to the methine protons within the N-vinylpyrrolidone and acrylonitrile repeating units, respectively [75]. These unique characteristic peaks were used to determine the molar ratio of the copolymer building blocks, which is nVP/AN = 2.8%. The other characteristic chemical shifts are methylene protons (-CH₂, **A** and **C**) of both AN and nVP groups and methylene protons (-CH₂, **E**, **F** and **G**) of the pyrrolidone ring as marked on the ¹H-NMR spectrum (Fig. 17a).

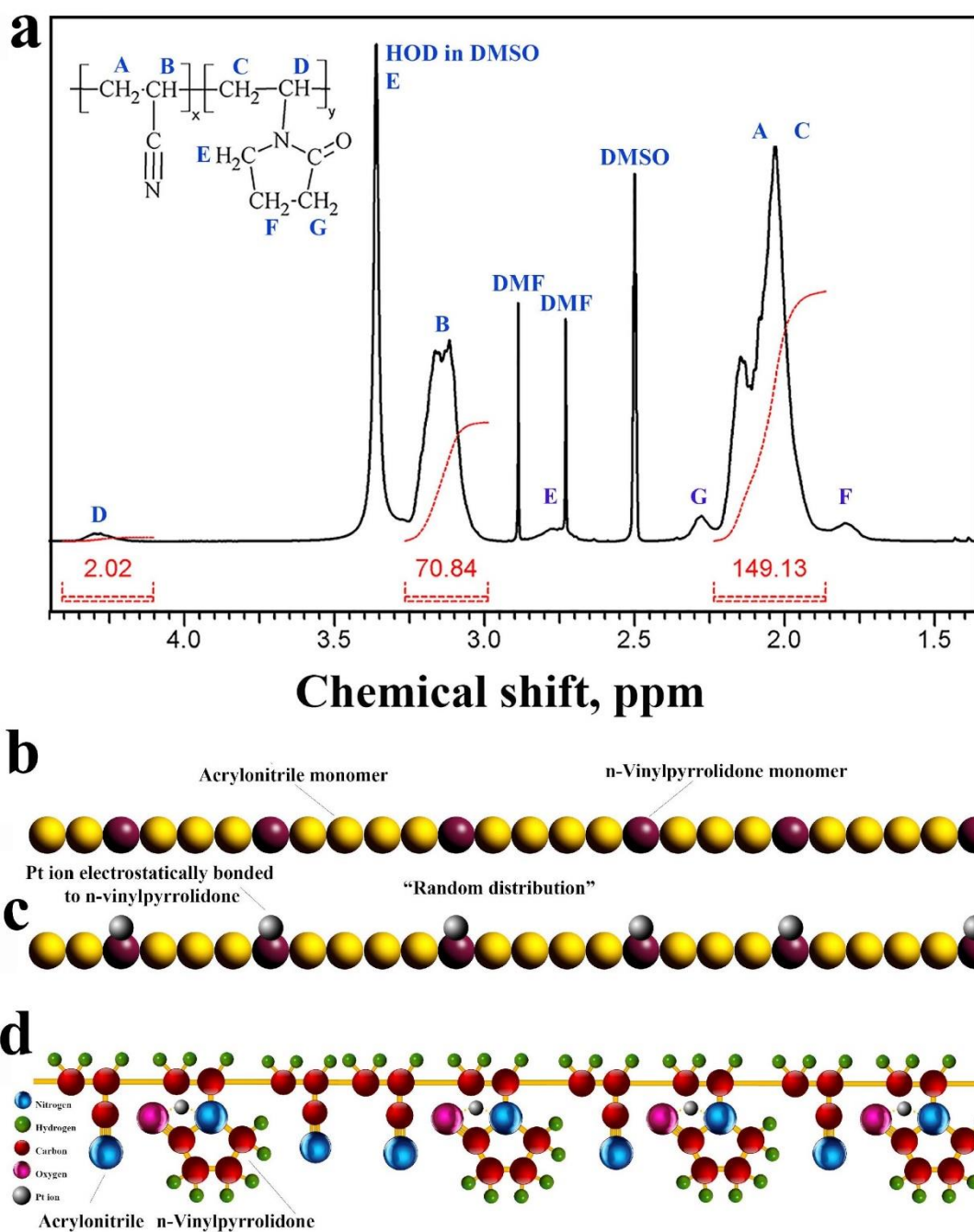


Fig.17. (a) ^1H NMR spectra of P(AN-co-nVP) as-synthesized copolymer, (b-d) schematic image showing the random copolymer and electrostatic interaction of Pt cations with polar groups of nVP.

The reactivity ratios are used for the estimation of the monomer distribution in the structure of the copolymers [76]. The reactivity ratios of AN and nVP units, calculated

based on the monomer feed ratios and output molar ratios of the monomers within the copolymer (interpreted from the ^1H NMR results), are $r_1 = 0.41$ and $r_2 = 2.36$, respectively. These reactivity ratios indicated the formation of a random copolymer (Fig. 17b). The effective random distribution of the nVP units within the structure of the copolymer was expected to lead to the even distribution of the platinum ions. Through such an effective localization mechanism, the growth and agglomeration of nanoparticles during reduction and carbonization stages can be avoided [5].

3.2. Electrospinning parameters

3.2.1. Electrospinning of nanofibers without carbon nanotube

With the aim of achieving a proper condition for the electrospinning of the nanofibers, different controlling parameters were manipulated and optimized according to the intended conditions. The concentration of the polymer solution, the metal salt/polymer weight ratio, the solution flow rate, the applied voltage difference, and the distance between the collector plate and the needle tip are some of the factors that affect the nanofiber morphology and nanoparticle distribution. The effect of solution flow rate was examined for different polymer solutions and the best electrospinnability condition was identified and utilized in the following experiments. The effect of applied voltage difference on the thickness and morphology of the fibers prepared with P(AN-co-nVP) copolymer and 5% PtCl_2 during electrospinning were investigated. Samples were prepared by increasing the applied voltage from 8 kV to 20 kV and the resulting fibers showed small differences as examined by SEM (Fig. 18). The diameter of the nanofibers changed around 350-400 nm. As the different voltage values applied did not appear to have a significant effect on the nanofiber size and morphology, the most stable voltage values observed during electrospinning process (12 kV) was chosen to be used in the rest of the experiments.

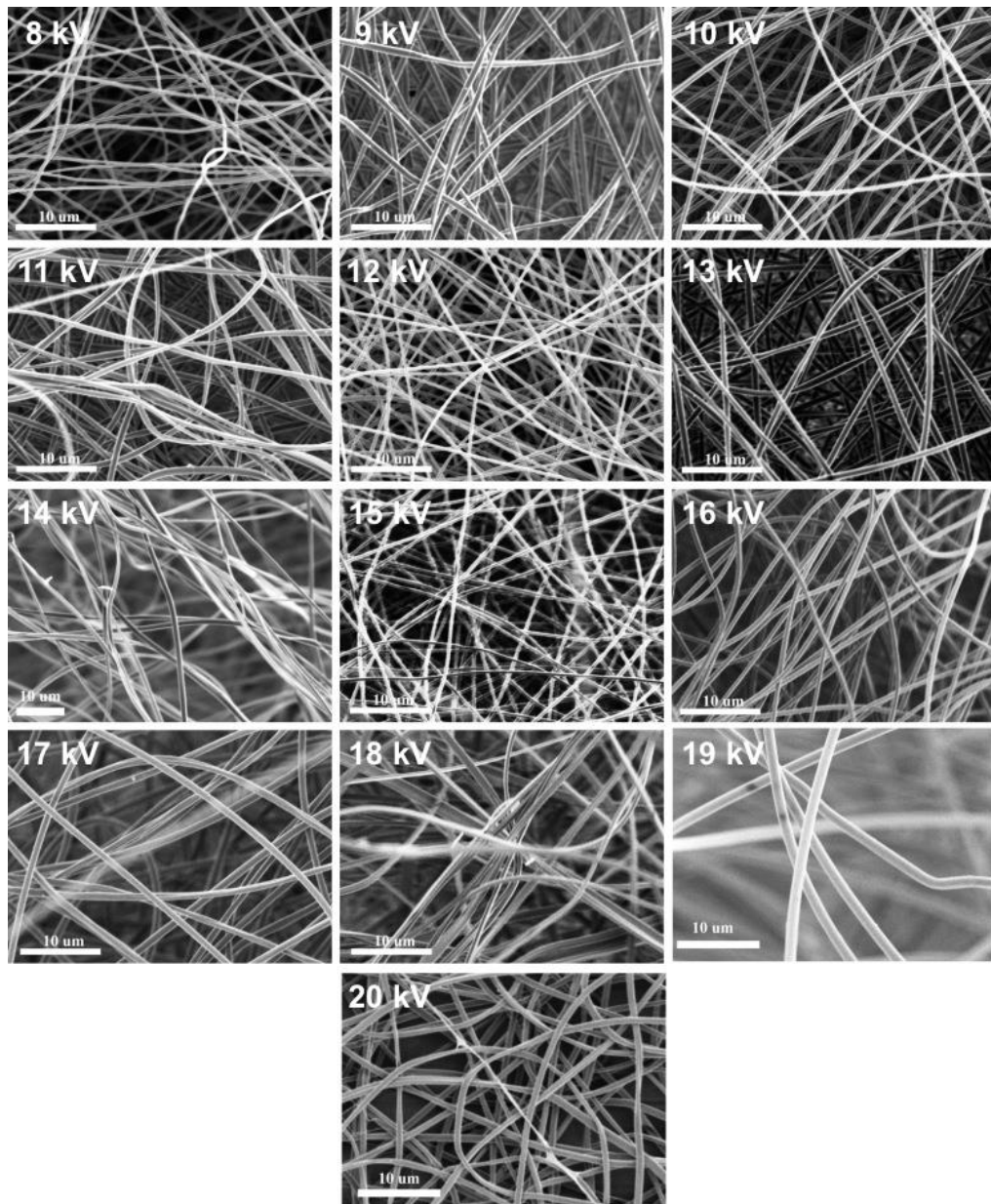


Fig.18. SEM images of the electrospun nanofibers of P(AN-co-nVP)/5wt.% PtCl₂ at different voltage applications.

3.2.2. Electrospinning of nanofiber/carbon nanotube hybrid structures

The P(AN-co-nVP)/5 wt.% PtCl₂ solution with 0.75 wt.% CNT with respect to the amount of polymer was also studied in terms of electrospinnability by changing process controlling parameters, similar to the CNT-free fibers described in previous section. After deciding about the viscosity of the electrospinning solution, the collector distance

and rate of electrospinning, the effect of applied potential difference on the thickness and morphology of the fibers was studied.

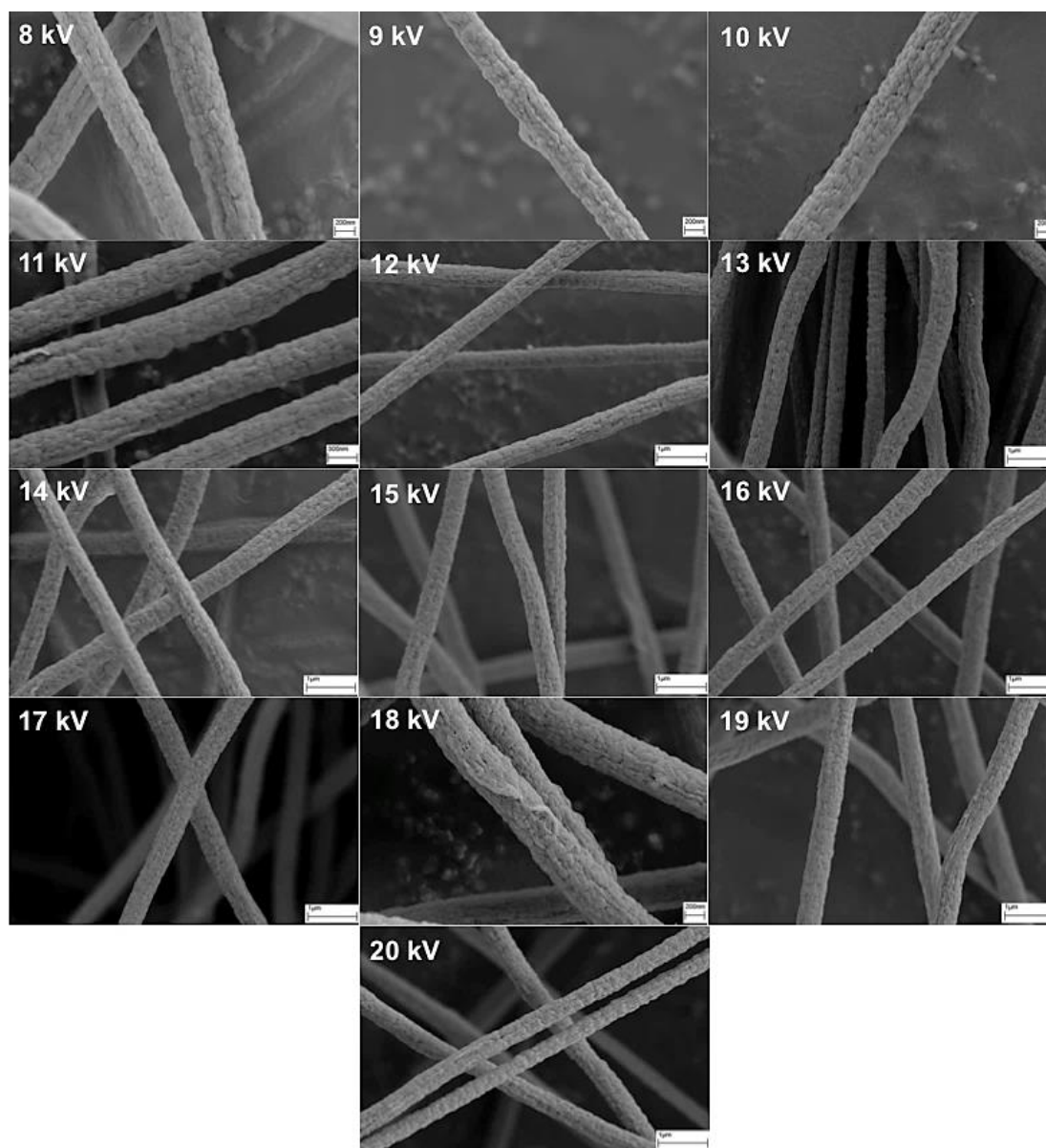


Fig.19. SEM images of the electrospun fibers of P(AN-co-VPYR)/CNT-0.75% / PtCl₂-5% with different voltage applications.

The applied voltage varied between 8 kV to 20 kV and the samples were observed using SEM (Fig. 19). Small differences were detected in the samples although no significant difference was observed. When these nanofibers were examined by TEM, the

agglomerated CNTs were observed in some regions (Fig. 20). The surface roughness observed in the SEM images (Fig. 19) was attributed to these small CNT aggregates in near-surface regions to give a rough surface to the nanofibers.

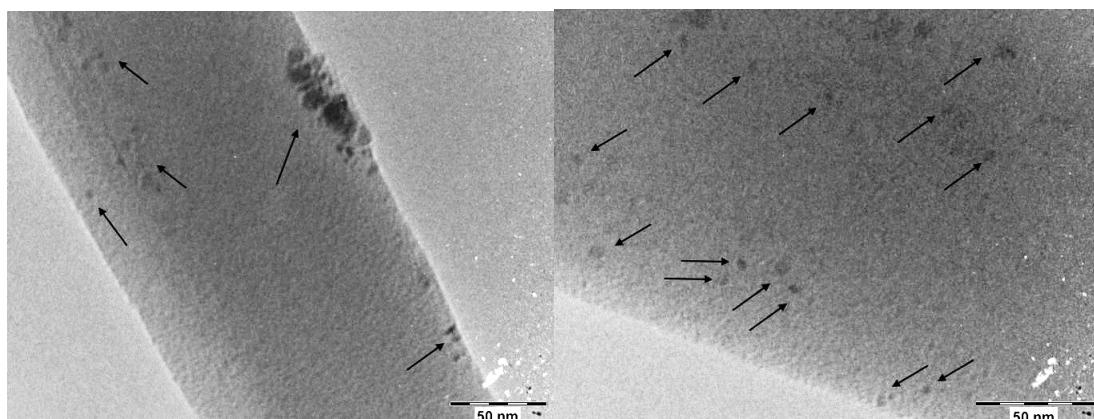


Fig.20. TEM images of P(AN-co-nVP)- 5 wt.% PtCl₂- 0.75 wt.% CNT.

3.3. Development of carbon nanofiber-supported Pt through carbothermal reduction

First, the electrospun nanofibers containing Pt precursor were heat treated up to 1000 °C without any chemical reduction of the salt. While polymeric nanofibers were carbonizing, PtCl₂ were carbothermally reduced to Pt nanoparticles. Effect of carbonization temperature on both fiber quality and particle size and distribution was investigated.

The effect of various carbonization temperatures on the structure of the nanofibers was investigated using ¹³C-SSNMR (Fig. 21a) spectroscopy. It was observed that the sp³ hybridized carbons (26.94 ppm) of polymeric nanofibers was gradually converted to the sp² hybridized carbon atoms (91-160 ppm) by increasing the carbonization temperature as seen in the ¹³C-SSNMR spectra of the nanofibers carbonized at 600°C, 800°C and 1000°C. At 600 °C, two adjacent peaks associated to the sp² hybridized carbon atoms of -C=C- (127 ppm) and pyrrole rings (150 ppm) produced from cyclization of cyano groups (-C≡N) of acrylonitrile could be observed. However, upon increasing the

carbonization temperature up to 1000 °C, the sp² hybridized carbon (–C=C–) structures characterized by the peak at 124 ppm become dominated, showing full cyclization.

Raman spectroscopy was also employed to qualitatively inspect the degree of graphitization in the carbonized samples at different temperatures (Fig. 21b). CNFs show two specific Raman bands, namely, G band and D band at 1580 cm⁻¹ and 1350 cm⁻¹ corresponding to the graphitic structure and disordered carbons, respectively [77]. It was observed that the intensity ratio of D-band over the G-band (I_D/I_G) decreased as the carbonization temperature increased from 600 °C to 1000 °C, signifying the transformation of disordered carbon into graphitic carbon. The I_D/I_G ratios for all carbothermal-reduced samples are provided in Table 1. It is observed that a significant enhancement in the extent of the graphitization takes place by increasing the carbonization temperature from 600 °C to 800 °C; however, the enhancement rate was lower at temperatures higher than 900 °C.

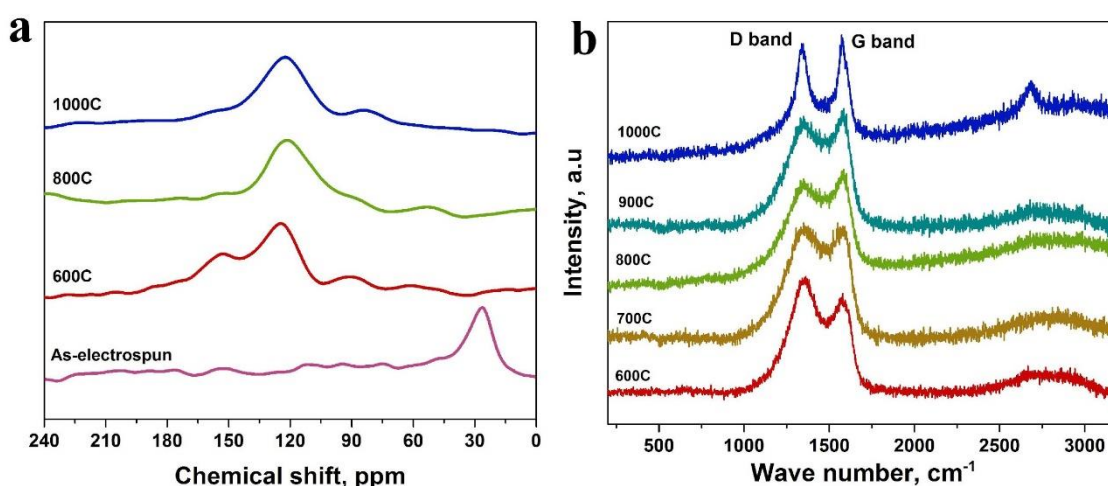


Fig.21. (a) ¹³C-SSNMR spectr of electrospun fibers before and after carbonization at 600 °C, 800 °C and 1000 °C and (b) Raman spectra of carbonized samples at different temperatures.

It is well-established that the electrical conductivity of the carbonaceous support of catalyst particles can extensively affect the catalytic performance of catalyst layer in fuel cell applications [3]. To study the effect of graphitization degree on the electrical

conductivity of nanofibers, the four-probe measurement was performed as summarized in Table 1. All carbon nanofibers demonstrated a relatively high conductivity comparable with the carbon fibers studied in similar studies [78].

It was observed that, by increasing of the carbonization temperature, the electrical conductivities are also increasing, which is in parallel with the graphitization degree of corresponding carbon fibers. During carbonization from 600 °C to 1000 °C, the graphite layers within the nanofibers grow steadily and the electrical conductivity significantly increases from 0.024 S cm⁻¹ to 1.39 S cm⁻¹, respectively. This observation could be associated with the increased number of the graphite domains and also decreased spacing between the graphene layers and also increased graphitized domain in carbon fibers, which facilitates the resonance vibration effect of the π bond and mobility of the π electrons and improves conductivity [79].

The size and distribution of the Pt particles in the carbon nanofibers, play an important role in their catalytic performance. As it was mentioned in the experimental section, in the carbothermal treated nanofibers, the PtCl₂ platinum precursor salt was thermally reduced during carbonization stage and no reducing agent was utilized beforehand. Since the Pt nanoparticles in carbothermal reduced nanofibers were not stabilized using reducing agent within the framework of the polymer and were simultaneously nucleated and grown during high-temperature carbonization procedures, relatively large Pt particles were expected. Nevertheless, the SEM images of the carbothermal treated samples (Fig.22) showed that relatively uniform distribution of fine particles was obtained, especially at low temperatures. This phenomenon indicated that the effective presence of the vinylpyrrolidone functional units in the copolymer has led to the confinement and immobilization of the platinum ions (Fig. 16b). Thus, the well separated and distributed individual Pt particles were formed in isolation with low degree of agglomeration. Nevertheless, upon increasing the carbonization temperature, the nucleated Pt clusters were potentially capable to move and coalesce in order to reduce their surface energy due to the increased thermodynamic propulsion enough for particle movements as seen in Fig. 22. On the other hand, carbonization at relatively high temperature is of a vital significance to enhance the graphitization and electrical conductivity of the carbon nanofibers. Therefore, finding a reasonable balance between

Pt particle size and graphitization degree in the polymer based carbon supported Pt materials is of crucial significance. As seen in the SEM micrographs of the various carbothermally reduced samples (Fig. 22), the size of the Pt particles increases and more particles appear on the surface of the nanofibers as the carbonization temperature increases. The Pt particles are not frequently observed on the surface of the fibers carbonized at 600 °C (Fig. 22b). The Pt nanoparticles are very small and relatively far from each other, indicating the fact that cluster agglomeration has not been dominated at this temperature and the inner Pt clusters has not effectively moved towards the surface of the fibers during carbonization. However, at higher carbonization temperatures from 800 °C to 1000 °C (Fig. 22c- 22f), the Pt particle size and population on the surface of nanofibers gradually increases and reaches to the significantly large agglomerates at 1000 °C.

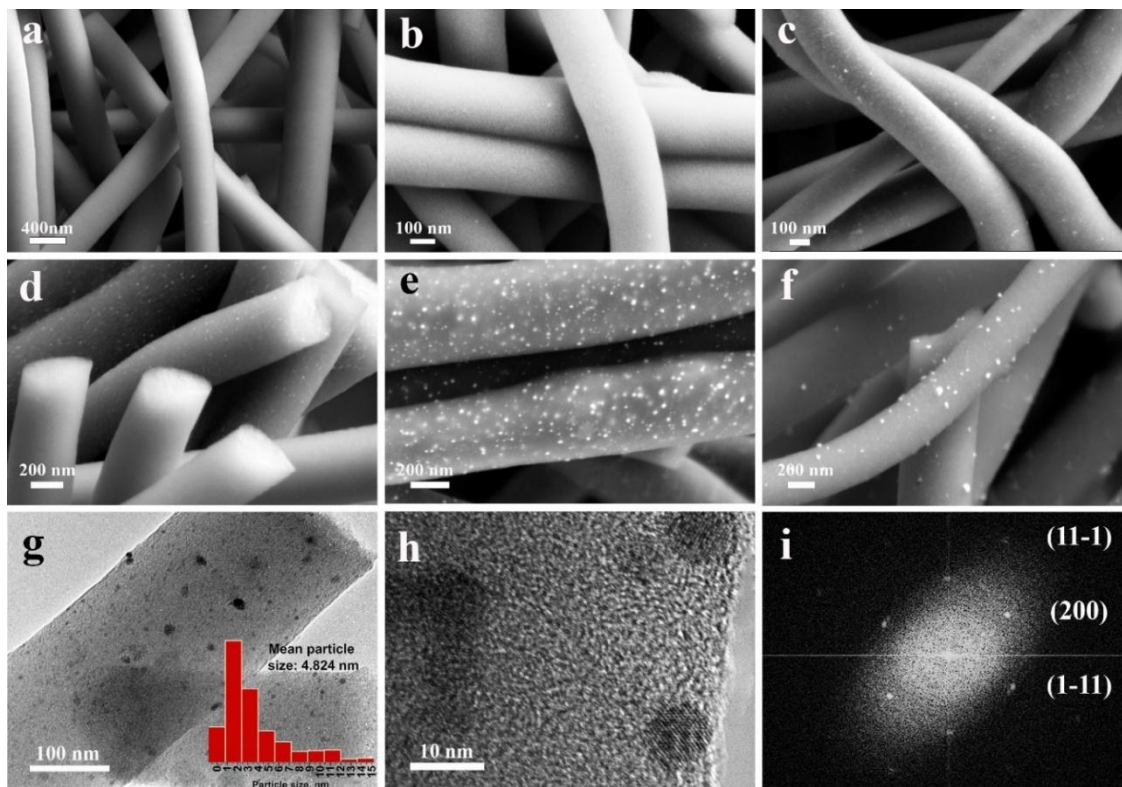


Fig.22. SEM images of as-electrospun (a) and carbothermally reduced nanofibers at different temperatures; (b) 600 °C, (c) 700 °C, (d) 800 °C, (e) 900 °C and (f) 1000 °C. TEM (g) and HR-TEM (h) images of carbonized samples at 800 °C; (i) FFT pattern of the particles in (h).

Unlike the samples carbonized in the range of 600 °C to 800 °C, which show very uniform particle size, the 900 °C and 1000 °C-carbonized samples demonstrated a bimodal particle size distribution. In other words, it was observed that increasing the carbonization temperature more than 800 °C resulted in agglomeration of the smaller particles and forming larger ones, which are energetically favorable at high temperatures. The Pt particle size distributions were obtained in all samples and mean particle sizes are collected in Table 1. Fig. 22g shows a representative TEM image of a carbothermally treated sample at 800 °C.

The inset histogram in the TEM image (Fig. 22g) confirms a wide particle size distribution in carbothermal treated samples. The crystalline structure of the Pt particles was also characterized using high resolution TEM analysis. Fig. 22h exhibits a typical atomic resolution TEM micrograph of the well-defined crystalline Pt particles in 800 °C carbothermal treated sample. The fast Fourier transform (FFT) pattern obtained from Pt particles in the same sample (Fig. 22i) confirms the face center cubic (FCC) crystalline structure of the Pt particles.

During the carbonization, difference between free energies of cluster surfaces stimulates their growth. In other word, under elevated temperatures, Pt particles tend to sinter through Ostwald ripening processes [80], in which the smaller particles are prone to dissolve and join larger particles to grow up and decrease the specific surface area. From the thermodynamic point of view, the driving force for sintering process is associated with the tendency to reduce the interfacial energy in the system, nevertheless, the conditions such as vacancy concentration gradient and stress gradients control the kinetics of sintering and growth [81]. For the sintering mechanism of Pt particles, two main mechanisms could be considered based on the “Pt atomic migration” and “Pt cluster migration” [82], [83]. A schematic image, demonstrating these two mechanisms, has been provided in Fig. 14. In the “Pt atomic migration” mode (Fig. 23a), the Pt atoms dissociate from the Pt clusters and move through the fibers via porosities or surface of the fibers and stop upon collision to other particles. For the reason that, larger particles are always stable (the Pt-Pt bonding energies are stronger than the Pt-CNF interaction), atomic migration usually takes place from smaller cluster towards larger particles and therefore leads to the diminishing of the smaller particles and further growth of larger

ones [84]. In the case of cluster migration (Fig. 23b), sintering is assumed to happen through movement of the small clusters through the fibers and specially across the surface and incorporating with the clusters on the way [84]. By increasing of the carbonization temperature, the kinetics of sintering processes accelerate and leads to the formation of the larger Pt particles in the nanofibers, especially over the surfaces (Fig. 23). Based on the activation energy required to move the single atoms and the bulk of a cluster, it can be inferred that the “Pt atomic migration” is mostly dominated in lower applied temperatures and “Pt crystallite migration” at elevated temperatures. The effect of the carbonization temperature on the average Pt size distribution was demonstrated in Table 1. By increasing the temperature from 700 °C to 1000 °C, around an order of magnitude greater Pt particles were generated. However, formation of smaller Pt nanoparticles (Fig. 23) in the nanofibers carbonized at lower temperatures (600 °C and 700 °C) denotes the fact that the applied activation energy for growth by temperature is not enough to induce the Pt clusters or atoms to move. This needs that, the Pt clusters must be effectively localized and their surface energies have been stabilized within the structure of the fibers. This phenomenon could be addressed through interpretation of ¹³C-NMR spectrums of 600 °C and 1000 °C carbonized samples (Fig. 21a). It is stated that; noble metal atoms can form stable π -complexes with -C=C- bonds of organic compounds and the stability of the complexes can enhance in the case of presence of an electronegative component in the vicinity of the -C=C- bond (like N in the pyrrole rings).

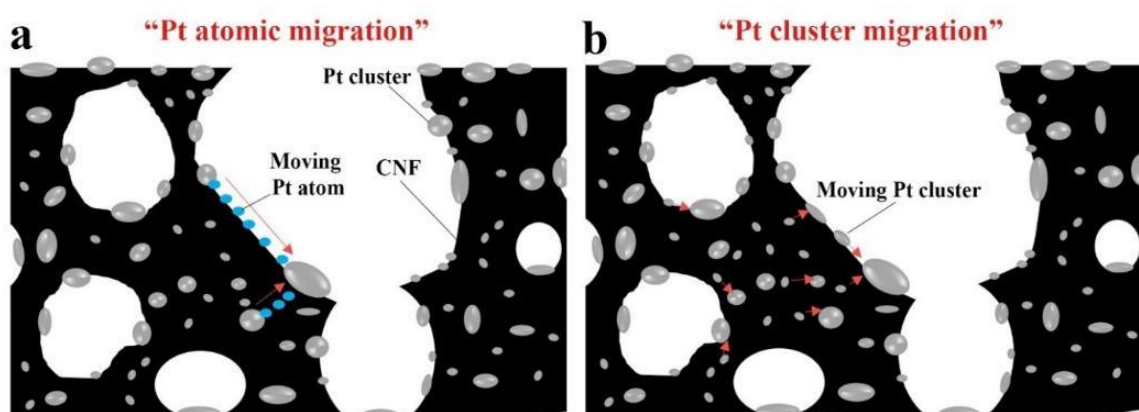


Fig.23. Schematic images showing the sintering mechanism of Pt in nanofibers.

This π -complex is explained to form between an occupied 4d orbital of the metal atom and an unoccupied molecular π^* -orbital of -C=C- fragment [85]. It means that, although the Pt atoms can establish π -complexes with both graphitic structure and pyrrole rings, there is a stronger interaction with the latter. Therefore, the presence of smaller Pt particles in samples carbonized at lower temperatures can be justified by considering the effective role of the pyrrole rings in formation of favorable interactions with Pt atoms and insufficient driving force (temperature) to overcome it. However, by increasing carbonization temperature, most of the polymeric chains and pyrrole rings are reradiated and lead to the weakening of chemical interactions of Pt atoms and fibers. Since the surface energies of the Pt clusters are less stabilized, the particles compensate this issue by sintering together. Nevertheless, compared to the other conventional techniques [86], [87], the particle size control obtained by in-situ method is quite smaller. In fact, the porosities throughout the fibers act as potential wells for the Pt atoms so that obstruct the movement of the particles [88]. At higher applied temperatures, the role of mechanical trapping and role of the micro-pores becomes more highlighted, due to the activation of metal flow throughout the fibers.

The XRD measurement was carried out to investigate the formation of crystalline Pt particles in the carbothermal treated samples (Fig. 24). The relative diffraction peaks at 40.0° , 45.9° , 67.5° and 81.7° corresponding to the (111), (200), (220), and (311), respectively, confirmed the crystalline structure of the Pt nanoparticles [36], [89]. It was observed in the XRD patterns that, by increasing the carbonization temperature, the Pt (111) peak in the samples becomes stronger, which might be associated with the larger Pt clusters incorporation in these materials. In the case of 600°C -carbonized samples, no diffraction peak is observed, showing that Pt particles are too small to be detected.

In addition, a broad peak in the XRD patterns which appears around $2\theta=26.5^\circ$ (Bragg reflection of graphitic structure in carbon (002)) signifies the formation of graphite structure in carbon nanofibers [90]. The intensity of this peak also increases as the carbonization temperature increases.

The average stacking height of the graphite planes (L_c) can be calculated based on Scherrer's formula [90] using this graphite peak in XRD spectra. It was observed that,

by increasing the carbonization temperature, the stacking height of the graphite planes within the carbon nanofibers was increased (Table 1).

The mean spacing between the graphite layers, which is called d_{002} , was also determined based on the characteristic graphite peak in the XRD patterns, showing a decrease with the increasing temperature [91] (Table 1). The $L_c \sim 53\%$ increases and d_{002} declines $\sim 4\%$ by increasing the carbonization temperature from 600°C to 800°C , denoting a high degree of graphitization at this temperature. The rate of graphitization was also improved by carbonizing at 900°C and 1000°C , however the values were comparable with 800°C sample.

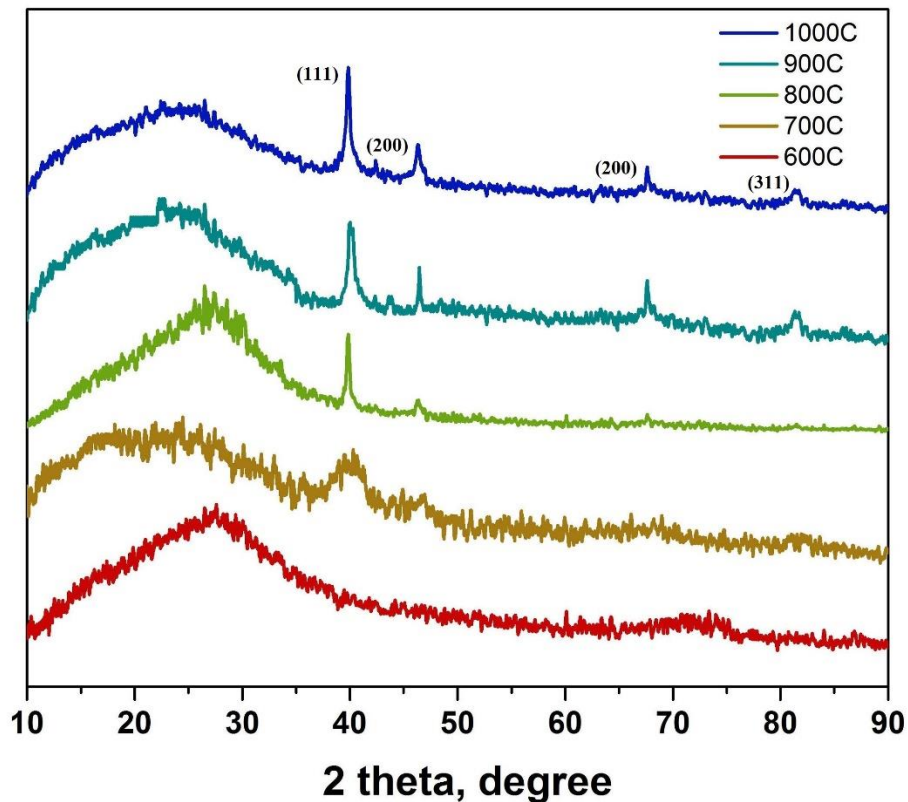


Fig.24. XRD spectrums of carbothermal reduced samples at various temperatures.

Thermogravimetric analysis (TGA) was conducted in order to determine the Pt loading within the nanofibers after carbonization, as summarized in Table 1. The Pt amount was obtained to be around 20-21 wt.% in almost all the samples.

Cyclic voltammetry (CV) was employed to explore the electrochemically active surface area (ECSA) of catalyst Pt on carbon nanofiber support. The ECSA values indicate the number of available active sites for charge transfer and also the access of a conductive path to transfer the electrons to and from the electrode surface in the catalyst material [92]. A high ECSA is favorable for fuel cell catalyst with high electrocatalytic activity [36]. The cyclic voltammograms demonstrating the characteristic peaks for oxidation and reduction of Pt are represented in Figs. 25. It is observed that the shapes of all cyclic voltammograms corresponding to different samples were identical and similar to the polycrystalline platinum behavior reported in the literature [93], [94].

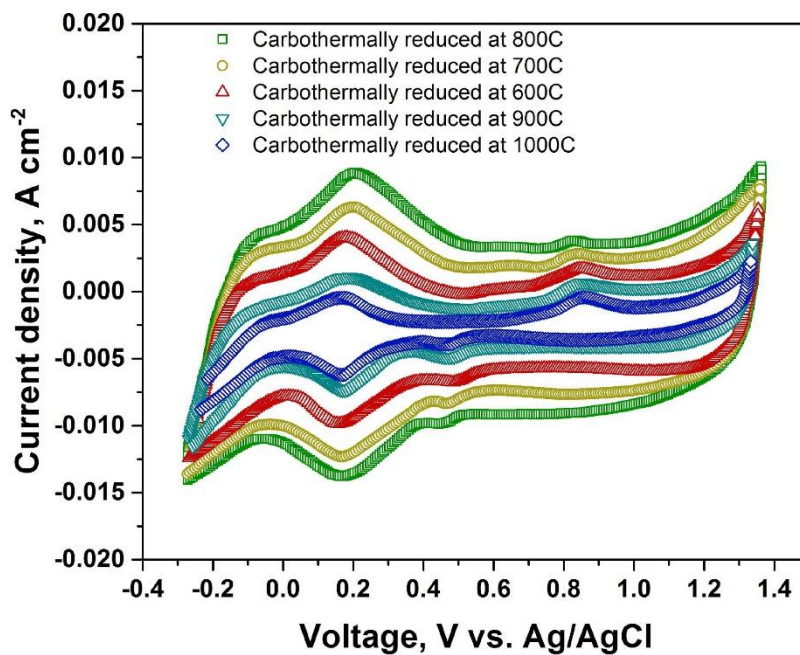


Fig.25. CV spectra of carbothermal reduced samples at various temperatures.

A hydrogen oxidation peak could be observed at -0.2V, which is attributed to the weak bond of hydrogen in (111) Pt crystal direction [36]. In the CV diagrams, following the anodic branch, the first peak at -0.2V (SCE) corresponds to the hydrogen adsorption. By

increasing the applied potential, Pt oxidation occurs. The oxide formation can proceed through two steps, which are evolved as two distinct peaks on CV curves. The first peak appeared around 0.2 V SCE, corresponds to the reaction of Pt with water molecules which gives rise to the platinum hydroxide (PtOH) formation. The second small bump (about 0.8 V SCE) could be associated to the Pt oxidation through conversion of PtOH to PtO. After reaching the maximum voltage of 1.4 V SCE, the direction of applied potential was reversed. Through cathodic branch of the CV diagrams, the oxide reduction occurred around 0.45 V SCE. At this region, the PtO was reduced into Pt, through reverse recursion. The Pt reduction procedure was accomplished through water formation. At the end, the cathodic hydrogen desorption occurred at the same potential of hydrogen adsorption around -0.2 V SCE.

Qualitatively, the voltammogram showed the catalytic activity, because the hydrogen adsorption-desorption peaks were clearly seen in the voltammogram at the potentials between -0.2 - 0.05 V (SCE). For quantitative measurements, the charge under the hydrogen adsorption peak is utilized to calculate the electrochemically active surface area [95]. The integrated area under the curves of hydrogen adsorption/desorption peaks after deducting the charge from the double layer area in the cyclic voltammogram depicts the total charge regarding to H⁺ adsorption/desorption (Q_H), and can be used to determine ECSA [77].

ECSA is calculated using the following equation, where Q_H is average total charge regarding to H⁺ adsorption/desorption. The theoretical charge of 210 μCcm⁻² is calculated by assuming one hydrogen is adsorbed for each Pt atom [96].

$$ECSA [cm^2 g_{Pt}^{-1}] = \frac{Q_H [\mu C cm^{-2}]}{210 [\mu C cm^{-2}] \times Pt_{loading} [g_{Pt} cm^{-2}]} \quad (4)$$

Using equation 4, the ECSA of all carbothermal reduced samples were calculated and summarized in Table 1. The highest electroactivity value of 53.06 m² g⁻¹ was obtained for the sample carbonized at 800 °C. The samples carbonized at temperatures lower than 800 °C, represented lower catalytic activity. The samples carbonized at higher temperatures also demonstrated a relatively lower electrocatalytic performance

compared to that of 800 °C carbonized one. The reason for the lower activity of the low temperature carbothermal treated samples could be associated to the lower degree of the graphitization and electrical conductivity of these samples, which restricted the efficient catalytic behavior. Although it was observed that the graphitization has been improved with the high carbonization temperatures, the Pt particles have been significantly coarsened. It is well established that, as the Pt particle size increases, the fraction of Pt atoms on the particle surface decreases, which means that the number of available sites for surface reactions decreases and leads to the lower reaction rate and catalytic activity [36]. The electroactive surface area of the commercial Pt catalyst (4 nm Pt particles and 20 wt.% Pt), as a reference material, is reported to be around 70 m² g⁻¹ [97], [98]. By comparing the ECSA values of all carbothermally reduced samples to that of commercial catalyst material, it was observed that, the range of the ECSA values of the carbothermal reduced samples are slightly lower than the commercial material with the same amount of Pt loading. The lower performance of the carbothermal treated samples is probably originated from the fact that, most of the Pt incorporated to CNFs is embedded inside the fibers. Although the CNFs have a porous structure, it is difficult for electrolyte solution (in CV test) to reach Pt particles through nano-sized pores compared to the Pt particles located directly on the surface of the carbon support as in the commercial materials. On the other hand, the mean particle size of the 800 °C carbonized sample, as the sample representing the best catalytic performance, is ~ 4.824 nm which is greater than that of commercial XC-72R (with 20 wt.% Pt), which is around 3.5- 4 nm [97].

Although Pt precursor is evenly dispersed within the polymer matrix by the aid of pyrrolidone groups, a long-term heat treatment at high temperatures, during which the Pt ions simultaneously nucleate and grow, results in the formation of big Pt particles. Upon this carbothermal reduction, the metallic particles lose their electrostatic interaction with functional nVP units; so, they migrate and combine to decrease their surface area. Therefore, a higher rate of Pt coarsening in carbothermal treated samples accounts for the formation of a bimodal particles size distribution consisted of large agglomerates and smaller particles as it was observed in TEM image in Fig. 22g. To address this issue, the Pt precursors can be reduced prior to carbonization to be appropriately stabilized within the polymeric matrix. It was assumed that, the reduced metallic Pt particles reach to a reasonable cluster size upon rapid reduction; therefore, they cannot have as much

mobility as the Pt nuclease. In this case, it is expected that the size of the stabilized Pt particles cannot change noticeably during the subsequent carbonization and lead to a uniform Pt distribution.

Table 1. Information about carbothermal treated electrospun P(AN-co-nVP)/ Pt-20 wt.% samples.

Carbonization Temperature (°C)	L_c (nm)	d_{002} (nm)	Pt mean particle size-electron microscopy (nm)	Pt wt.% -TGA	Electroactive Surface Area (ECSA, m ² /g)	I_D/I_G
600	0.58	3.4	2.8	20	31.4	3.5
700	0.64	3.4	3.7	21	37.3	2.6
800	0.89	3.3	4.8	20	43.1	0.4
900	0.97	3.2	9.3	20	28.1	0.3
1000	1.14	3.1	11.3	21	23.2	0.2

3.4. Development of Pt containing nanofibers through chemical reduction

Several samples containing different amounts of the PtCl₂ were prepared under different reducing conditions and characterized. The samples have been categorized regarding their Pt contents consisted of samples with 5 and 20 wt.% Pt. Table 2 summarizes the various conditions utilized to treat each groups of the samples. In the following sections, a brief explanation will be provided on the corresponding results achieved from each type of the samples.

After analyzing different conditions, the best procedure for production of the fibers was utilized for synthesizing CNT-containing nanofibers to improve the catalytic performance of the materials.

Table 2. A summary of the samples studied and the conditions used in this study.

Amount of Pt	Condition	Reducing Agent	Immersion Time in (RA) (h/min)	Microwave reduction
5 wt.% Pt	Effect of immersion time and reducing agent	Hydrazine	24	0
			42	0
			116	0
			132	0
	Effect of microwave time and reducing agent	Hydrazine	0	3 min
			0	
			0	
			0	
20 wt.% Pt	Effect of microwave time and different reducing agents	Ethylene glycol	0	3 min
			0	3 min
			0	3 min
			0	3 min
		Sodium borohydride	0	3 min
			0	3 min
			0	3 min
			0	3 min
		Hydrazine	0	3 min and 15-30-60-120s
			0	3 min and 15-30-60-120s
			0	3 min and 15-30-60-120s
			0	3 min and 15-30-60-120s

3.4.1. Nanofibers containing 5 wt.% Pt

3.4.1.1. Effect of the reducing agent and the reduction time

Electrospun nanofibers-PtCl₂ mats were subjected to different chemical reducing conditions and the obtained samples were visually examined by SEM and elemental analysis was performed by EDX spectroscopy. The nanocomposite mats containing PtCl₂ were incubated in 5 vol.% and 10 vol.% hydrazine solutions prepared with pure water for different times, and the effect of concentration of reducing solution and the duration of the reduction was investigated. Reduction times are indicated in the headings of SEM and EDX images showing the result of the relevant analysis. Fig. 26 shows the SEM

image and EDX analysis of 5 wt.% PtCl₂-containing electrospun nanofibers. X-ray diffraction peaks of Pt and Cl elements can be observed in the EDX spectrum. After the chemical reduction, the quantities of these peaks of Pt and Cl elements were compared and the amounts of reduction were investigated.

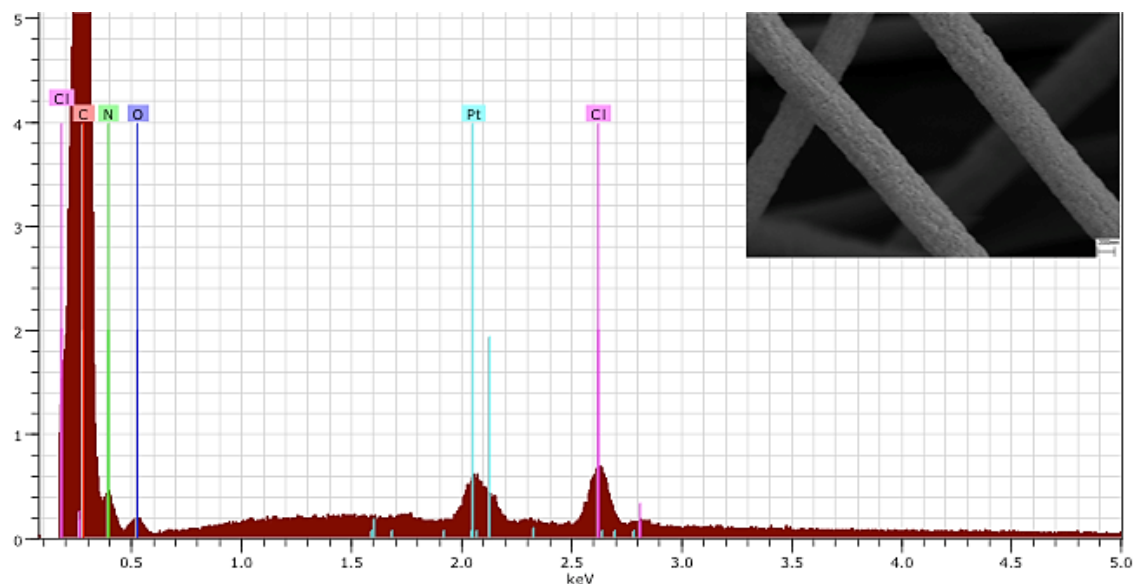


Fig.26. SEM image and EDX spectrum of as-electrospun nanofibers of P(AN-co-nVP)/5wt% PtCl₂.

The electrospun polymer nanofibers-PtCl₂ samples were suspended in a 5% aqueous hydrazine solution for 1 hour and 24 h and the resulting materials were analyzed by SEM and EDX. In the SEM images of Fig.27, the Pt nanoparticles are not visible, but the Cl/Pt ratio decreases in the EDX analysis as compared to the unreduced one (Fig.26). When the 1 hour and 24 h reduction times were compared, the Cl/Pt ratio decreased with time. When the SEM images were examined, it was observed that the reducing solution caused some degradation on the fiber surfaces, and these degradations was found to be more intense in the samples waiting in solution for 24 hours.

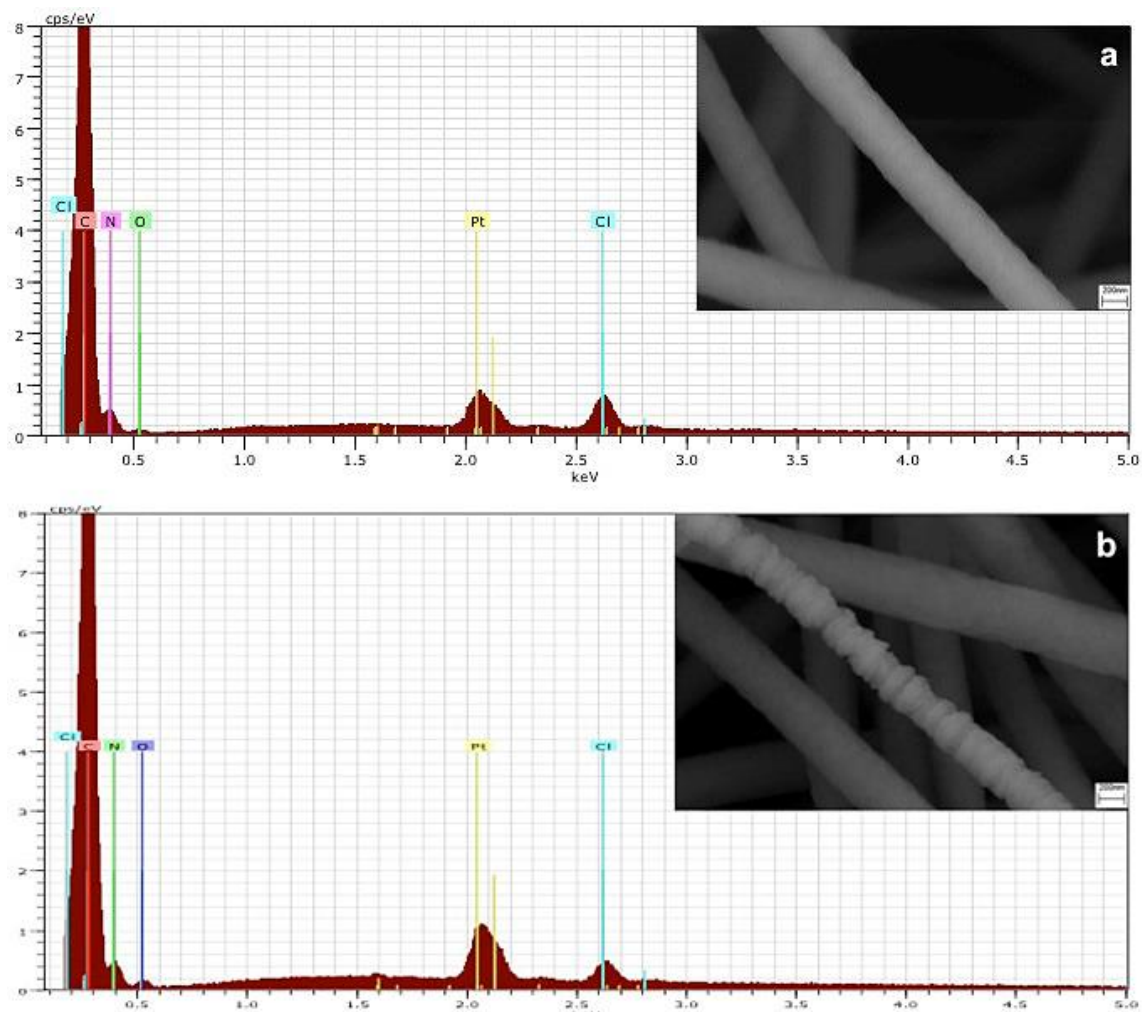


Fig.27. SEM images and EDX spectra of P(AN-co-nVP)/5 wt.% PtCl₂ nanofibers immersed in 5 vol.% hydrazine solutions for (a) 1 hour, (b) 24 hours.

After the reduction with 5% hydrazine aqueous solution was observed to be incomplete, the concentration of the reducing agent was increased to 10 vol.% hydrazine and reduction was performed for 1 h, 8 h and 24 h. When the Cl / Pt ratios were compared, the amount of Cl decreased with increasing the reduction period. After the 24 h reduction reaction, the Cl presence is still observed, but the amount appears to be very small (Fig. 28).

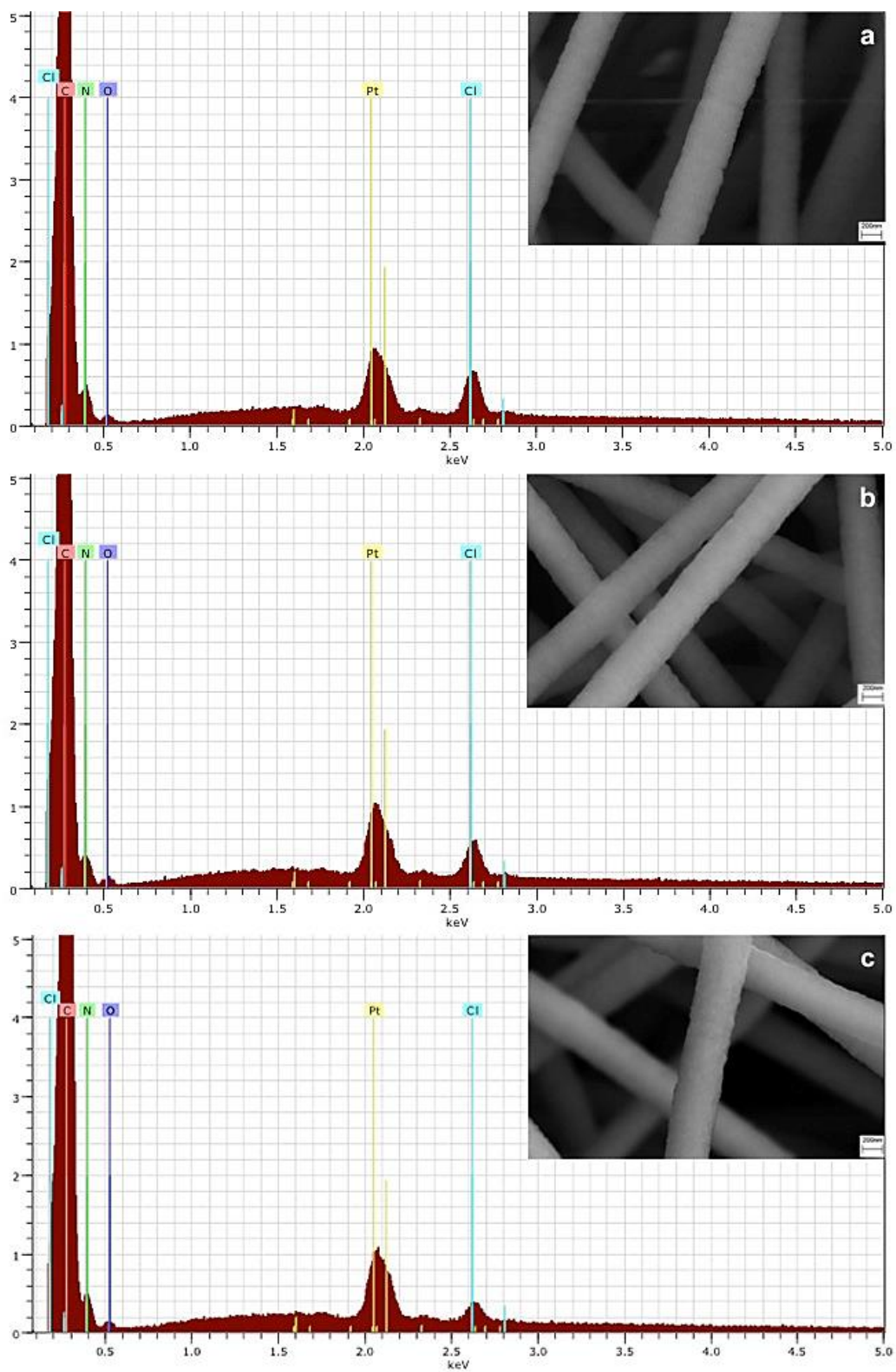


Fig.28. SEM images and EDX spectra of P(AN-co-nVP)/5 wt.% PtCl₂ nanofibers reduced in 10% hydrazine solution, (a) 1 hour, (b) 8 hours and (c) 24 hours.

Some of the samples were stored in the reducing solution for up to 116 h after it was found that the amount of reduced Pt increased with the reduction time but the process was not completed even after 116 h. The small amount of Cl observed in the EDX spectrum (Fig. 29) showed that the reduction period of up to 5 days was not sufficient and other methods were investigated to reduce this Pt salt.

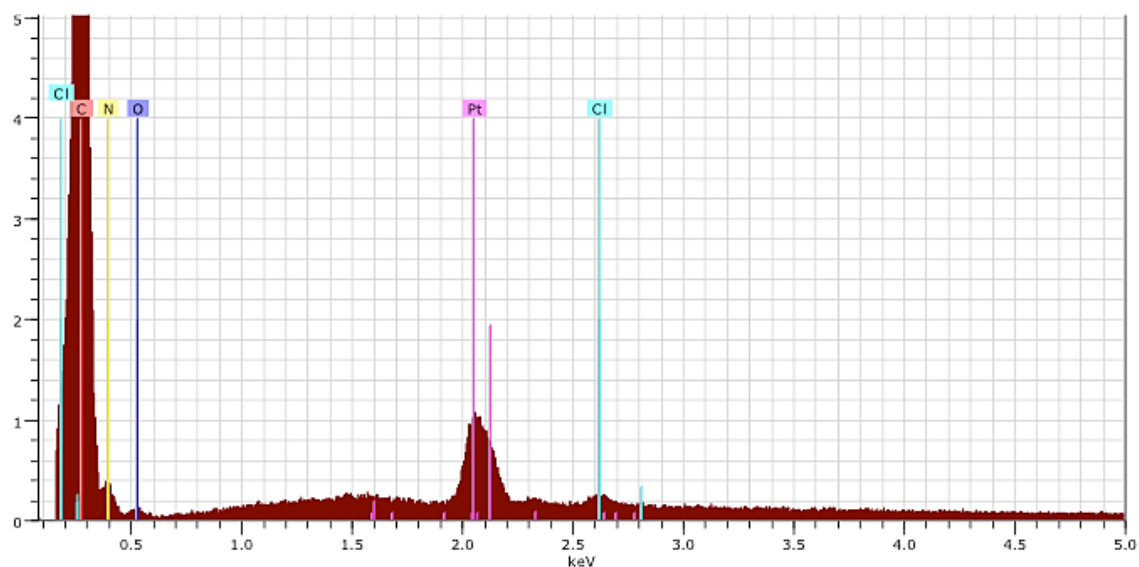


Fig.29. EDX spectrum of P(AN-co-nVP)/5 wt.% PtCl₂ sample reduced in 10% hydrazine solution, 116 hours.

Fig. 30 also shows the SEM images of the carbonized samples containing 5 wt.% Pt which are reduced at different time periods. According to the SEM images, no clear sign of Pt particles is represented on the carbon fibers while deformation of some fibers was clearly observed.

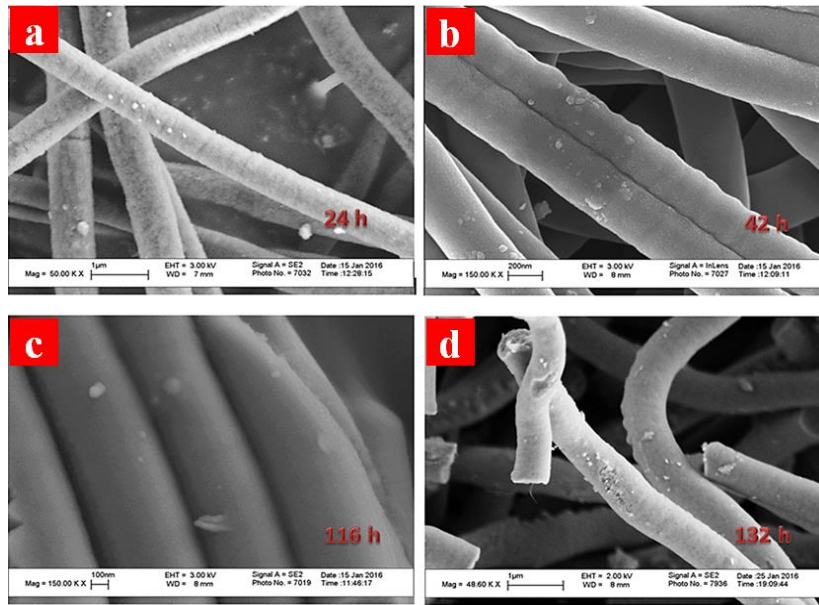


Fig.30. SEM images of the carbonized samples at 800 °C containing 5 wt.% Pt reduced in 5 wt.% hydrazine hydrate solution for different periods of times.

Fig. 31 represents the XRD patterns of the carbonized samples reduced in different times. There was no sign of Pt peak in the patterns even at a very long duration of time, e.g. 132 h, immersion at room temperature. Therefore, the microwave treatment was decided to be carried out on samples at different times and within different reducing agents.

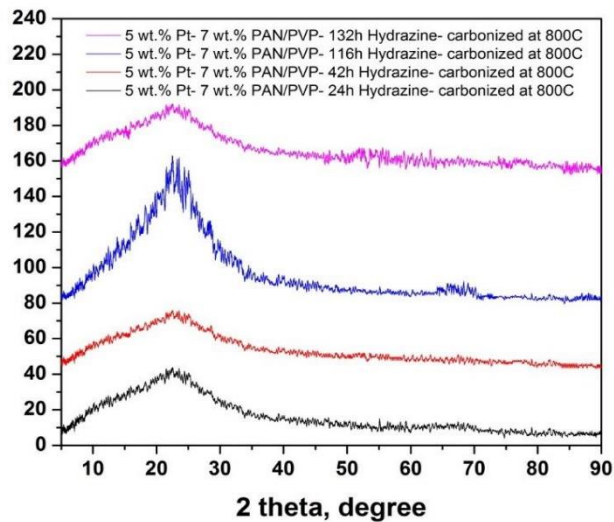


Fig.31. XRD patterns of the carbonized samples at 800 °C containing 5 wt.% Pt reduced in 5 wt.% hydrazine hydrate solution for different periods of times.

3.4.1.2. Effect of microwave

Given the obtained data from different immersion times, the microwave treatment of samples within different time periods was applied to the fibers in order to have a good control on the Pt particle size and distribution and also to benefit the effect high temperature to reduce the PtCl_2 salt. Therefore, several microwave irradiation times on fiber samples within hydrazine reducing agent was taken into account. In the literature, it has been shown that similar platinum precursors such as PtCl_4 and H_2PtCl_6 are reduced by microwave irradiation [99].

Some of the samples that were left in the 10% hydrazine solution for 46 hours were compared to the microwave treated sample. As can be seen in Fig. 32, all of the PtCl_2 salts were reduced to Pt in the sample subjected to microwave treatment after standing 46 h in a hydrazine solution. The microwave irradiation was applied 6 times with a total of 60 seconds periods provided that it was 10 seconds - open, 40 seconds - closed in a 1 KW domestic microwave oven.

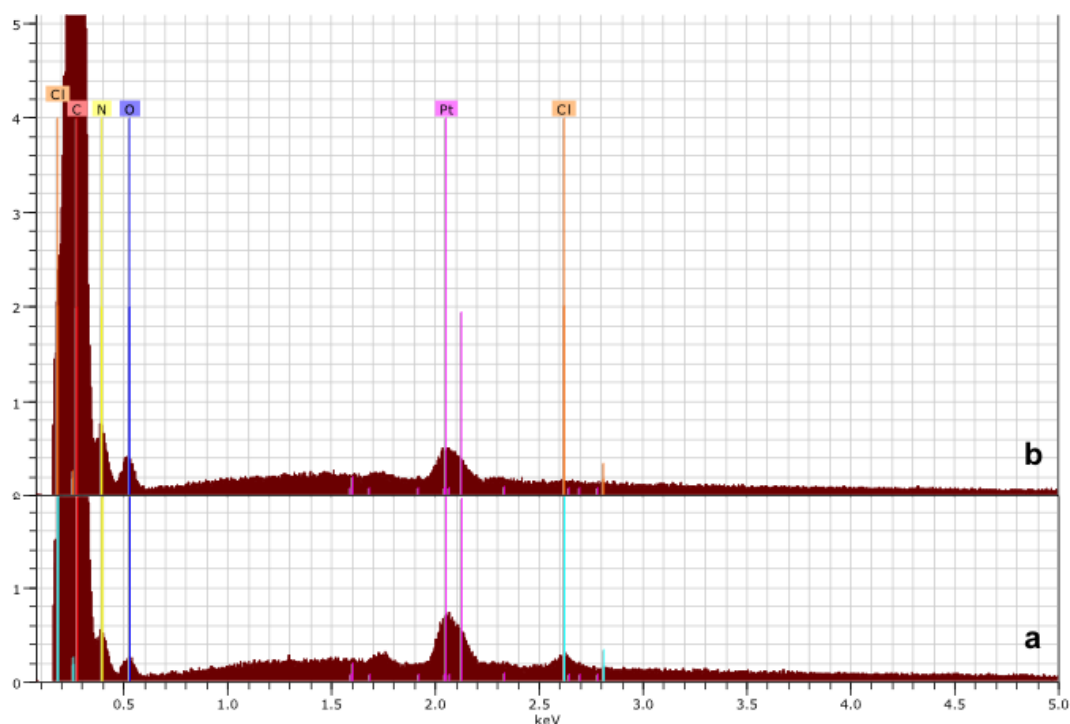


Fig.32. P(AN-co-nVP)/5 wt.% PtCl_2 reduced in 10% hydrazine solution, EDX spectrum, 46 hours (a) chemical reduction only, (b) chemical reduction + microwave buildup.

3.4.2. Samples with 20 wt.% Pt

3.4.2.1. Effect of microwave time and reducing agent

3.4.2.1.1. Hydrazine, Ethylene glycol and Sodium borohydride

To study the effect of hydrazine reduction for Pt nanoparticles in the fibers containing higher amounts of Pt precursor, the 20 wt.% Pt containing samples were utilized. The XRD patterns of the 20 wt.% Pt samples were obtained before carbonization to study the effect of reduction process on the samples. Fig. 33 demonstrates the XRD results of 20 wt.% Pt samples after reduction step and before carbonization of the fibers.

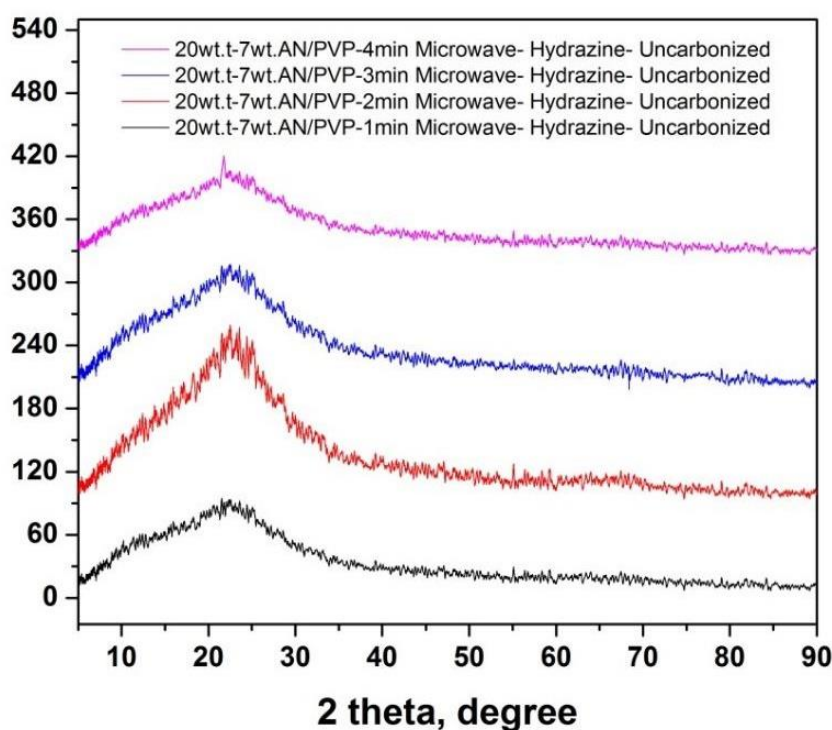


Fig.33. XRD patterns of 20 wt.% Pt samples reduced in hydrazine under microwave during four different periods of times.

Fig.34 demonstrates the XRD patterns of the 20 wt.% Pt samples reduced in hydrazine solution after carbonization. It is observed that, the characteristic peaks associated with the crystalline Pt particles are obvious in the XRD patterns.

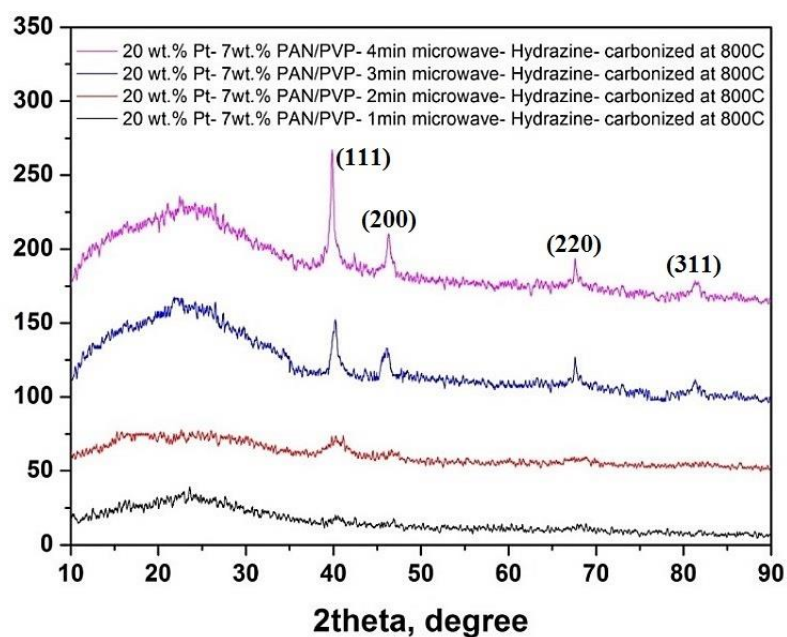


Fig.34. XRD patterns of 20 wt.% Pt samples reduced in hydrazine under microwave during four different periods of times; (a) before and (b) after carbonization at 800 °C.

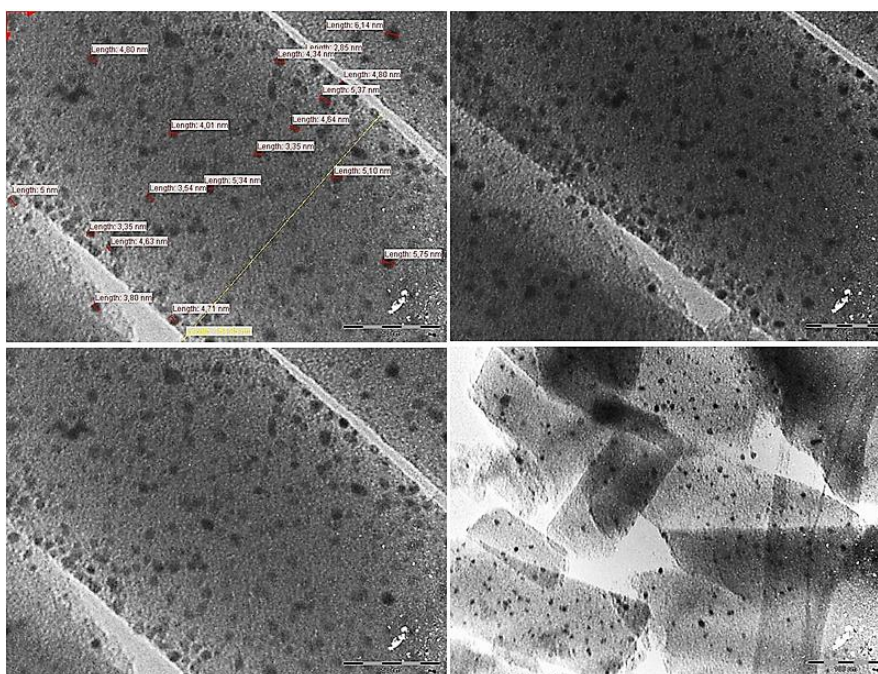


Fig.35. The typical TEM images of the 20 wt.% Pt sample reduced under microwave in hydrazine for 3 min.

The typical TEM images of the 20 wt.% Pt sample reduced under microwave in hydrazine for 3 min are also represented in Fig. 35. It could be observed that the Pt particles with an average size of 3 nm have been evenly distributed all over the nanofibers and also a relatively decent size distribution is achieved. This observation designated the fact that, using a microwave-assisted reduction in presence of the hydrazine hydrate solution on 20 wt.% Pt precursor containing nanofibers successfully enabled us to take a good control over the size distribution of the Pt nanoparticles.

Two other reducing agents, namely ethylene glycol (EG) and sodium borohydride (NaBH_4) were also utilized with the aim of studying the effect of microwave reduction using other reducing agents on the quality and the size of the Pt nanoparticles produced in the nanofibers. Both of these reducing agents have some advantages such a good microwave absorbance capacity and being more environmental friendly and cost-effective compared to the hydrazine solution. Fig.36 represents the XRD patterns of the 20 wt.% Pt samples microwave-reduced for 3 min in EG and NaBH_4 solutions, respectively, after carbonization at 800 °C. The characteristic Pt peaks could be observed using both reducing agents.

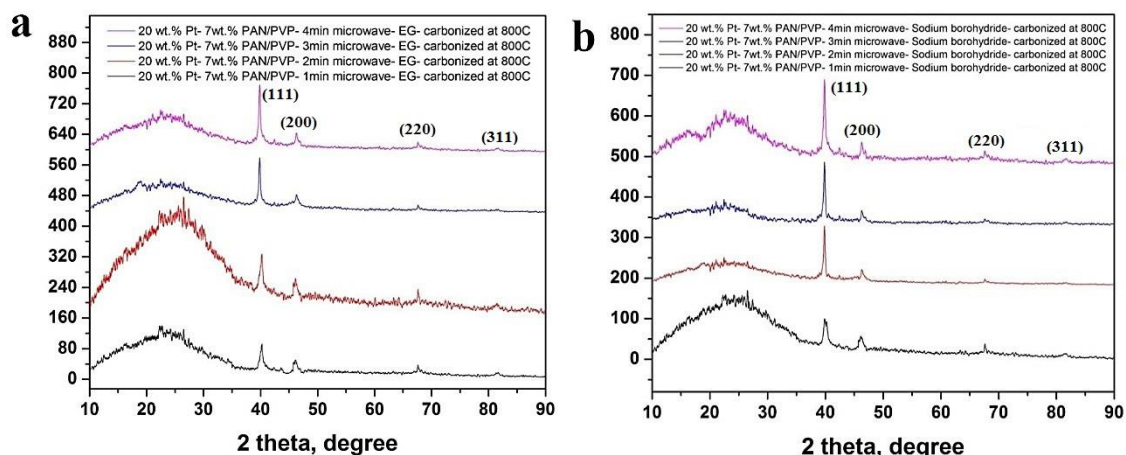


Fig.36. (a) XRD patterns of 20 wt.% Pt samples reduced in ethylene glycol under microwave during four different periods of times after carbonization at 800 °C and (b) XRD patterns of 20 wt.% Pt samples reduced in sodium borohydride under microwave during four different periods of times after carbonization at 800 °C.

The typical SEM images of three 20 wt.% Pt samples reduced three different reducing agents under 3 min microwave irradiation are represented in Fig. 37. It is observed that sodium borohydride leads to the formation of big Pt particles with a large range of size distribution (Fig.37a) while the ethylene glycol has created damages on the surface of fibers and has created extremely large Pt particles (Fig.37b). On the other hand, fine Pt nanoparticles randomly distributed throughout the fibers were observed when hydrazine is used as a reducing agent (Fig.37c and Fig.37d), which enables a better control over the size distribution of the Pt nanoparticles.

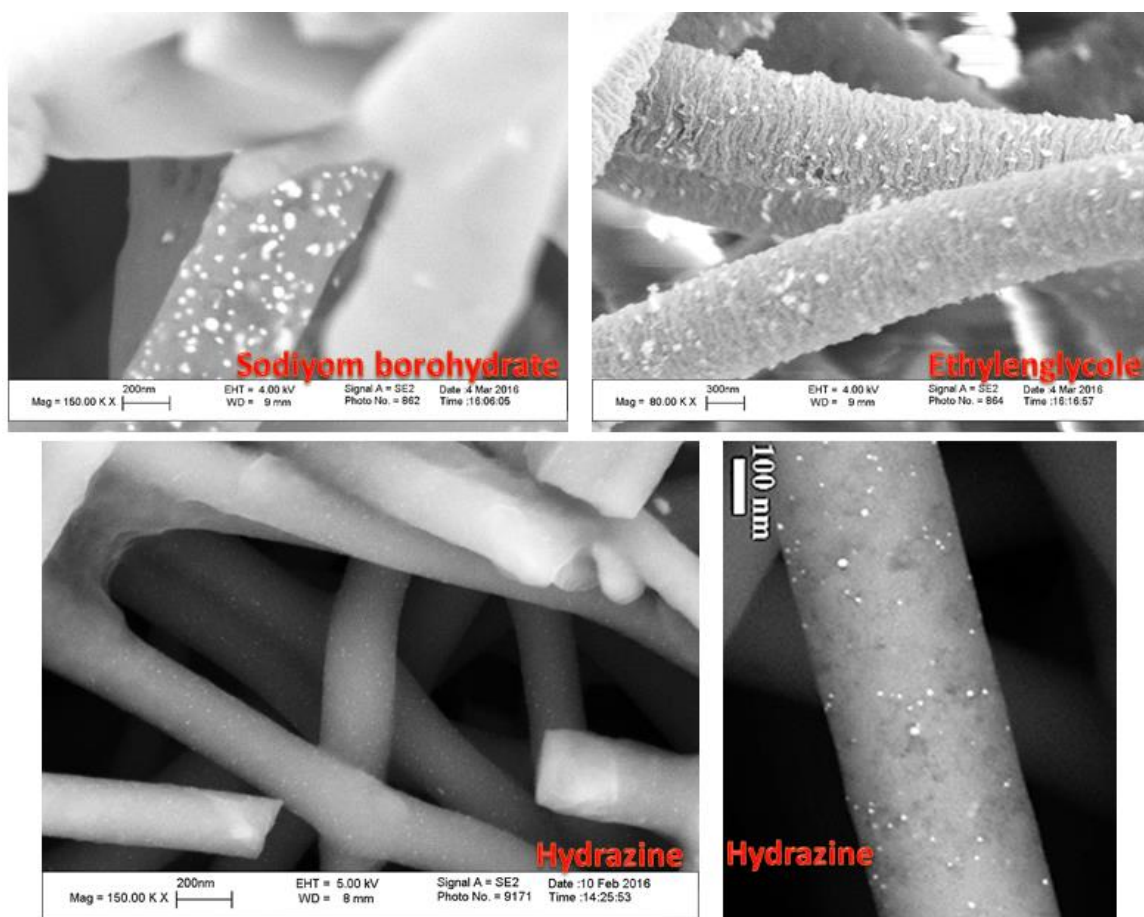


Fig.37. SEM images of three 20 wt.% Pt samples reduced three different reducing agents under 3 min microwave irradiation in hydrazine.

Comparing the results obtained from 5 wt.% Pt and 20 wt.% Pt containing samples, it was observed that using 5 wt.% Pt in carbon nanofibers cannot lead to the formation of an enough Pt nanoparticles throughout the fibers and specially on their surface. Furthermore, the amount of Pt used to synthesize most of the commercial PEMFC electrodes is reported to be around 20 wt.% Pt. Therefore, to include an enough amount of Pt in the fibers and also be comparable with the existing commercial electrodes, the 20 wt.% Pt containing nanofibers were chosen to perform further analysis. Also, based on SEM analysis on different samples reduced by various agents, it was observed that the hydrazine hydride solution provides the most consorable Pt size tuning once the samples were treated with microwave. However, using ethylene glycol and sodium borohydride, the damaged fiber surfaces along with bigger particles were obtained. Therefore, the hydrazine hydride solution was preferred as the best reducing agent to apply to the rest of the samples.

3.5. Microwave assisted reduced Pt in 20 wt.% Pt containing samples

A rapid microwave (MW)-assisted reduction in a 5 wt.% hydrazine hydrate aqueous solution was employed to achieve uniformly dispersed Pt nanoparticles in the range of a few nanometers in diameter. Microwave benefits the specific properties of compounds to transform electromagnetic energy into the heat energy. This is achieved through dielectric losses in materials and the magnitude of energy conversion depends on the dielectric properties of the molecules [100]. Both units of acrylonitrile and vinylpyrrolidone units in the copolymer are moderately polar and therefore microwave absorber materials [101]. Therefore, the microwave absorption in the presence of a reducing agent can take part throughout the nanofibers. Due to the intensive oscillations and collision of polar molecules under the influence of electromagnetic microwave irradiation, the produced heating energy results in the significantly accelerated Pt nucleation [102]. Another interesting feature of microwave treatment is associated with its rapid volumetric performance, which heats the bulk of the material simultaneously, resulting in the homogeneous Pt reduction [100]. By applying microwave irradiation to the polymeric fibers, the Pt^{2+} is rapidly reduced into the Pt^0 and becomes stabilized within the polymeric fibers. In addition to the microwave absorption of the polymeric fibers, the

polarization of the water molecules existing in the reducing solution also contributes to the overall heating up in the reducing medium.

As mentioned in the experimental section, the SWCNTs were also added to the nanofibers to study their effect on the catalytic performance of the samples. Due to their high conductivity, the SWCNTs can increase the number of dipole moments and polarizability in the nanofiber composites [101]. The microwave absorption of SWCNTs emanates from polarization, Ohmic losses and multiple scattering due to the large specific surface area [103]. The high aspect ratio of the SWCNTs is also an important factor that improves the absorptivity of the CNT/polymer composites [103]. The SWCNT structure can absorb the microwave irradiation through the interaction between microwave and π conjugated electrons and transform it to the Joule heat and cause to the rapid increase of the local temperature [104]. Therefore, during reduction of CNT-containing fibers, more thermal energy is expected to accelerate the reduction process and increases the number of Pt nucleation sites in the fibers. The reduction of the Pt^{2+} nanoparticles in presence of hydrazine hydrate is given in following equation [5]:



The SEM images of the microwave treated CNT-free and CNT-containing samples after carbonization are demonstrated in Fig. 38. The surface morphology and appearance of the nanofibers with and without CNTs are similar. Since no significant CNT extrusion or bumps on the surface of the CNT-containing fibers were observed, it could be speculated that most of the CNTs were embedded within the nanofibers. The CNTs as one-dimensional nanomaterials with nanoscale width and micron-sized length are quite long to be simply aligned through axial direction of nanofibers. Nevertheless, the electrospinning method as a promising technique can address this issue [105]. Higher solution conductivity exerts greater electric current on the flowing jet during electrospinning and induces large charge accumulation, which leads to a strong electrostatic repulsion throughout the jet. This strong repulsive force can simply overcome the surface tension and let the jet to elongate further which results in the reduction of fiber diameter [106]. Small signs of CNT orientation within the fibers could be observed in the broken parts in SEM micrographs (Fig. 38g and 38h). Comparing the SEM micrographs of both types of the microwave-assisted reduced samples (with and

without CNT) showed that the size distribution of the Pt particles, specially treated at shorter irradiation times, have been significantly improved. This could be associated with the effective influence of stabilization of the metallized Pt particles through microwave reduction prior to the carbonization. In both types of the nanofibers, upon increasing the microwave irradiation time, the Pt particles have increased in size due to the time-dependent nature of coarsening process. Furthermore, it was also observed that the size of the Pt particles in the CNT-containing nanofibers have been decreased compared to the CNT-free ones. Formation of relatively finer particles in the CNT-containing samples was attributed to the presence of CNTs as a good microwave absorber, which has accelerated the nucleation and instantaneous stabilization of the Pt particles. It seems that, addition of the CNTs into the nanofibers has led to the predomination of the rapid nucleation of new Pt clusters rather than growth. By increasing of the microwave treatment time, the size of Pt particles tends to increase due to the increased diffusion and growth opportunity at longer durations (120s). In both types of samples, a bimodal particle size distribution was observed, consisted of larger and fine particles. However, the average particle size was relatively smaller in the case of CNT-containing fibers. An interesting phenomenon about 120s microwave reduced CNT-containing samples was concentration of the Pt particles around CNTs (Fig. 38i).

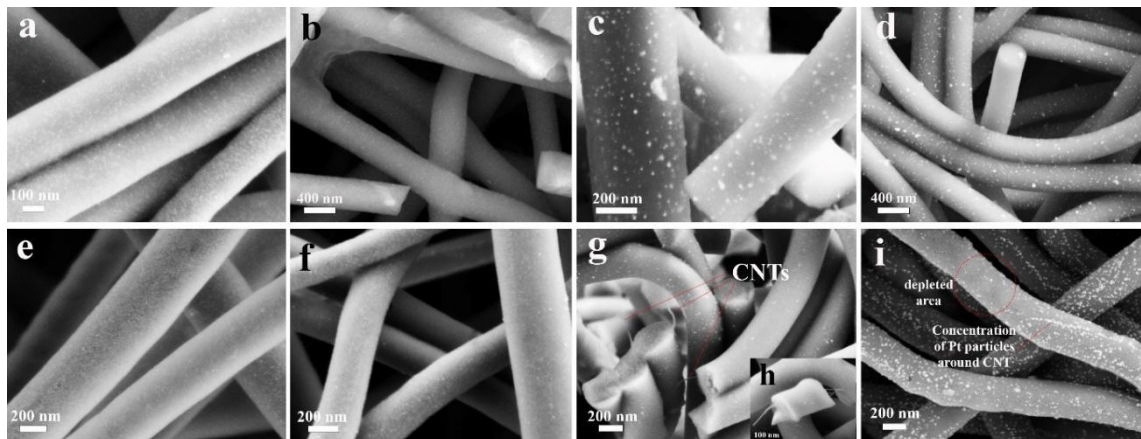


Fig.38. SEM images of microwave-assisted reduced CNT-free nanofibers in 5 % Hydrazine hydrate solution for(a) 15s, (b) 30s, (c) 60s, (d) 120s and CNT-containing samples reduced for (e) 15s, (f) 30s, (g) 60s and (i) 120s.

It was also observed that, upon attraction of Pt particles towards CNTs, the surrounding area of the CNTs becomes depleted from particles. This behavior could be associated to the high microwave absorptivity of the CNTs and also enough time for the Pt clusters to migrate and agglomerate around CNTs.

Pt particle size distribution and orientation of the CNTs throughout the nanofibers were also characterized with the TEM analysis. The TEM images of microwave treated P(AN-co-nVP)/Pt-20 wt.% nanofibers along with corresponding particle size distribution histograms are illustrated in Fig. 39a-c. Significantly smaller Pt particles and uniform particle distribution are observed, especially in 15s (Fig. 39a) and 30s (Fig. 39b) microwave-reduced nanofibers, compared to the carbothermally-reduced samples treated with the same temperature (800 C). By increasing the microwave treatment time, the particles tend to aggregate and form a bimodal particle size distribution (Fig. 39c). The minimum average particle size of about 1.75 nm is obtained in 15 s microwave irradiated CNT-free sample, which is calculated using image processing of TEM micrographs. The 30s treated sample also represented a similar narrow particle size distribution as 15s treated sample and average particle size of around 2.85 nm.

The CNT-containing samples exhibited an improved dispersion of Pt particles and smaller mean particle size compared to the corresponding CNT-free samples (Fig. 39d-39f). For instance, the 15s treated CNT-containing sample represented a mean particle size of about 0.862 nm which is equivalent to approximately 50% size declining with respect to its CNT-free counterpart (1.751 nm), due to the effective influence of the CNTs. By increasing of the microwave irradiation time, the Pt average particle size also increased in the CNT-containing samples (Table 2), however it has a lower coarsening rate.

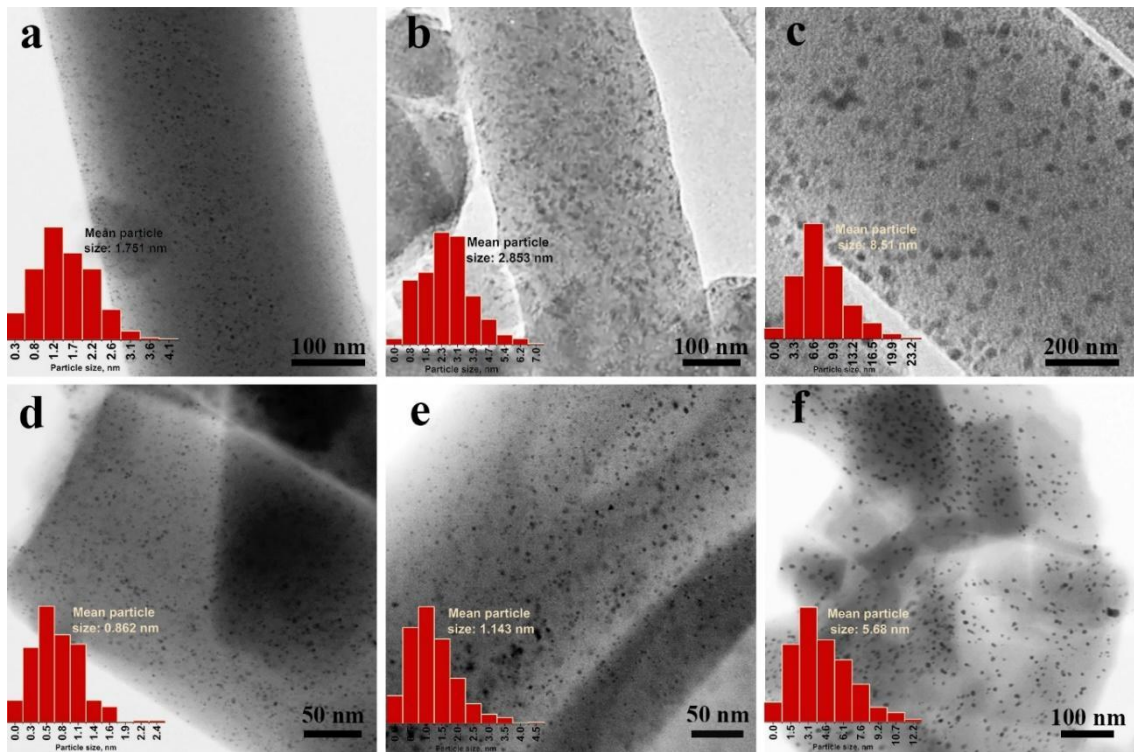


Fig.39. TEM images of microwave-assisted reduced CNT-free samples for (a) 15s, (b) 30s, (c) 60s, (d) 120s and TEM images of CNT-containing samples reduced for (d) 15s, (e) 30s, (f) 60s and (d) 120s.

Distribution of the CNTs was also observed in a typical CNT-containing sample (30s) using high resolution TEM (Fig. 40a). Although both CNFs and SWCNTs are consisted of the same carbon material, they can be observed as aligned tubes along the CNFs in the HRTEM image (Fig. 40a) due to their more ordered graphitic structure compared to the CNFs. The FFT pattern corresponding to the CNTs represented as inset image in Fig. 46b, approves the regularly aligned structure of the CNTs within the CNFs. The atomic layers of a Pt cluster are demonstrated in HRTEM image in Fig. 40c. The FFT pattern obtained from this particle (Fig. 40d) reveals a perfect FCC crystalline structure of the Pt particles.

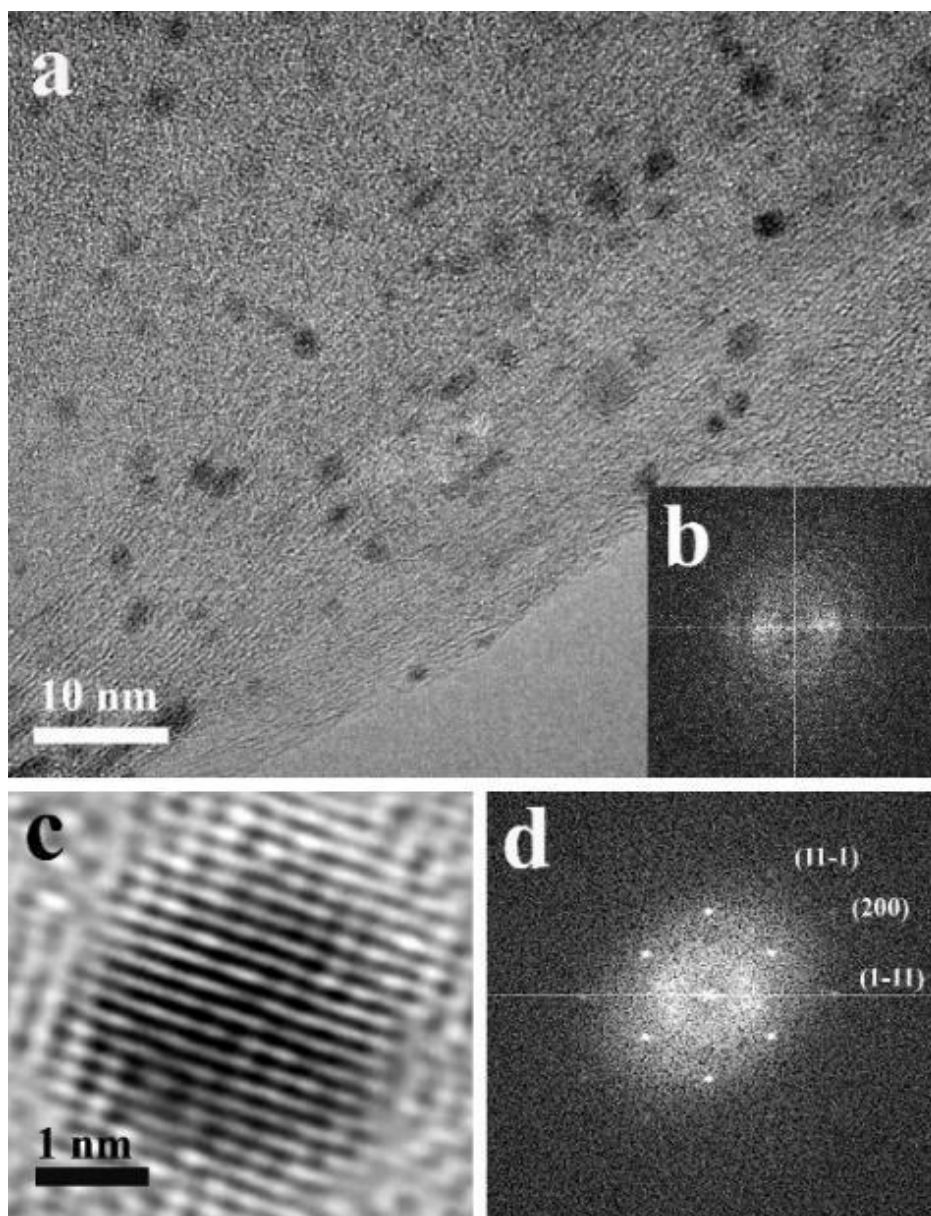


Fig.40. (a) HR-TEM image showing the alignment of the SWCNTs through CNF; (b) FFT pattern of SWCNTs; (c) HR-TEM image of Pt atoms in the FCC structure of a single crystal Pt and (d) FFT pattern of FCC structure of Pt.

In order to assess the crystal structure of Pt particles in all microwave treated samples, the XRD analysis was carried out (Fig. 41a and 41b). Four characteristic peaks at 46.6° , 54.7° , 80.6° and 98.7° were detected, associated to the (111), (200), (220) and (311) reflection planes of FCC platinum, respectively. [107]. In the XRD spectra of CNT-containing samples, represented in Fig. 41b, the XRD pattern of the pristine CNT is also included, in which the representative diffraction peaks at 30.0° and 50.4° could be

associated to the (002) and (004) planes of the hexagonal graphite structure [107]. The XRD results of the CNT-containing samples revealed that, they have also inherited the characteristic peaks of CNT. The small particle size effect is obvious about samples treated for lower times [108]. In other words, in the samples containing particles being in the range of 0.5- 2 nm, which do not have a regular bulk band structure, the binding energy shifts towards higher values and leads to the broadening of their Pt peaks [95].

However, by increasing the microwave reduction time, in both types of the samples, the sharper peaks were appeared. Using the XRD spectrums, the L_c and d_{200} were also calculated for the CNT-containing fibers, which were about 0.94 nm and 3.22nm, respectively. It revealed that, the presence of the CNTs can noticeably increase the size of the crystalline domains in the P(AN-co-nVP) derived nanofibers.

It has been frequently stated in the literature that, the incorporated CNTs in the structure of the CNFs, can play a templating rule for the formation of graphite layers within CNFs and thus, contribute to a higher degree of graphitization [109]. To survey this phenomenon in the CNT-containing samples, the Raman analysis was conducted and the result was compared with a CNT-free sample (Fig. 41c). Both samples represented the strong Raman peaks, attributed to the G and D bands (Fig. 41c). The ratio of I_D/I_G in the CNT-containing sample was calculated as 0.36, which as compared to its CNT-free counterpart (carbothermally-reduced at 800 °C, 0.44), the graphitization has been improved by ~ 18 %.

The four-probe technique was utilized to study the effect of enhanced graphitization on the electrical conductivity of the CNT-containing samples compared to the CNT-free counterparts, the electrical conductivity of the CNT-containing samples (0.95 S cm^{-1}) was meaningfully improved with respect to the CNT-free fibers (0.78 S cm^{-1}). In fact, the presence of a high concentration of significantly conductive CNTs and increased graphitization in the CNT-containing nanofibers could be referred as the main reason for the enhanced electrical conductivity. The enhanced graphitization in these structures is reported to be as a result of templating effect of the CNTs that instigate the nucleation and growth of graphene stacks within the nanofibers [110]. Furthermore, due to the alignment of the CNTs through the axis of nanofiber an additional enhancement in the electrical conductivity could be achieved [110].

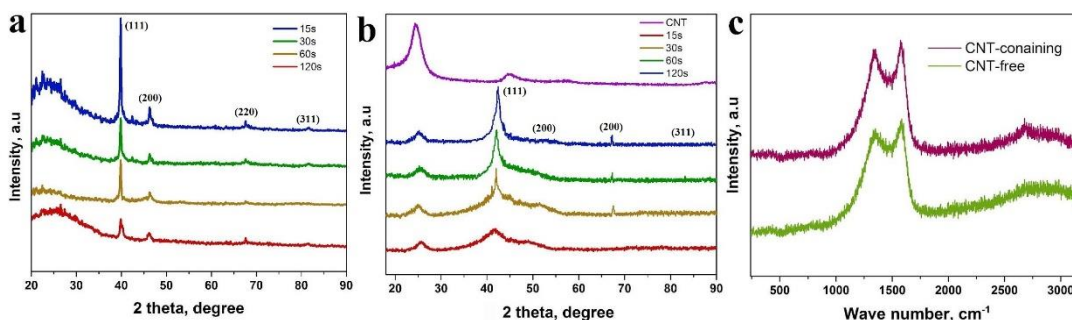


Fig.41. XRD spectrums of nanofibers (a) without and (b) with CNT and (c) Raman spectrums comparing the graphitization in nanofibers with and without CNT carbonized at 800°C.

The surface area analysis using BET test was also conducted on microwave treated samples with and without CNT, to investigate the probable impact of the CNTs on the porosity of the nanofibers. The results signified a noticeable enhancement in the surface area of the CNT-containing nanofibers ($385 \text{ m}^2 \text{ g}^{-1}$) compared to their CNT-free counterparts ($336 \text{ m}^2 \text{ g}^{-1}$).

The TGA characterization was performed on all nanofibers (with and without CNT) under oxygen atmosphere to determine the Pt contents and tabulated in Table 3.

The CV analysis was carried out to calculate the electrocatalytic activities of two groups of samples, The CV voltammograms representing the characteristic peaks for Pt oxidation and reduction in CNT-free and CNT-containing samples are demonstrated in Fig. 42a and 42b, respectively. In all CV voltammograms, a hydrogen oxidation peak at around -0.2V for hydrogen adsorption and two representative peaks for oxide formation reaction at 0.5 V SCE and 0.8 V SCE in the anodic branch; and the oxide reduction peak at 0.45 V SCE and a hydrogen desorption at around -0.2 V SCE were observed through cathodic branch of the CV diagrams. Similar to the carbothermal reduced nanofibers, the appearance of the CV spectra was identical to the polycrystalline platinum [13].

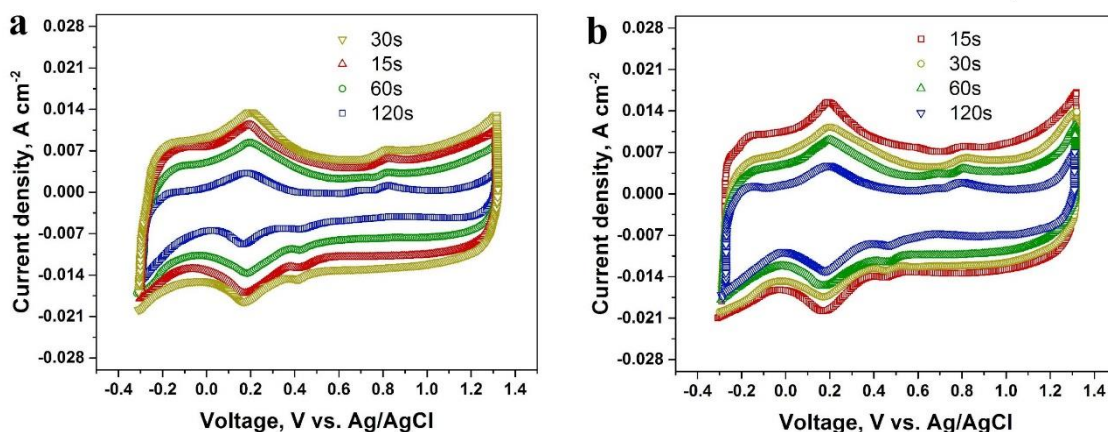


Fig.42. CV spectra of fibers: (a) without and (b) with CNT.

The ECSA of the samples was determined by the means of equation (4), through integrating the area under the hydrogen adsorption peaks on CV curves (table 3). The ECSA values obtained for CNT-free samples showed that, the 15 s and 30 s reduced samples have a relatively close value, however, the 30s treated sample demonstrated a slightly higher catalytic activity, despite the fact that the 15s sample possesses smaller average particle size (1.751 nm). Such a peculiar observation might be associated with the lower portion of Pt cluster near the surface of the nanofibers, accessible for the electrolyte. Regarding the ECSA results, the electrocatalytic performance is reduced with an increase in the mean Pt particle size. Comparing the ECSA results obtained from the microwave-assisted reduced (30s irradiated) with that of the carbothermal treatment (800°C), it was found that the nanofibers reduced before carbonization represented about an order of magnitude improved catalytic response compared to the carbothermal reduced samples.

The CV voltammograms of CNT-containing samples (Fig. 42b) demonstrated a more rectangular shape compared to the CNT-free ones. (42a). This feature could be attributed to the higher double layer capacitance of CNT-containing samples, because of a higher porosity of CNFs and the electrochemically inert nature of the CNTs [111]. Increasing of the effective surface area between catalyst layer and electrolyte leads to the increased amount of charge carriers attracted to the interface and therefore enhanced capacity [112]. The hydrogen adsorption peak at -0.2 V and Pt oxide formation reaction at 0.5 V SCE and 0.8 V SCE in the anodic branch; and the oxide reduction peak at 0.45 V SCE

and a hydrogen desorption at around -0.2 V SCE were evolved in the cathodic branch of all CV diagrams (Fig. 42b). The calculated values of the ECSA for all samples, using equation (4), were listed in Table 3. All CNT-containing nanofibers demonstrate an improved catalytic performance compared to their CNT-free counterparts.

Table 3. Information about microwave treated samples with and without CNTs.

Sample type	condition	Pt mean particle size-electron microscopy (nm)	Pt wt.% -TGA	Electroactive Surface Area (ECSA, m²g⁻¹)
CNT-free	Mic- treated- 15s	1.7	21	65.3
	Mic- treated- 30s	2.8	20	68.4
	Mic- treated- 60s	8.5	21	31.8
	Mic- treated- 120s	10.9	21	23.2
CNT-Containing	Mic- treated- 15s	0.8	20	82.5
	Mic- treated- 30s	1.1	21	73.8
	Mic- treated- 60s	5.7	20	45.7
	Mic- treated- 120s	7.6	20	34.4

Despite CNT-free samples, with a best catalytic performance achieved for 30s microwave irradiated sample (ECSA=68.44 m²g⁻¹), the CNT-containing fibers represented the highest activity for 15s of microwave reduction (ECSA=82.55 m²g⁻¹). This alteration could be ascribed to the significant number of Pt clusters over the surface of this sample (Fig. 39), which has been already described. Additionally, a higher surface area, due to the presence of CNTs in this group of samples could be considered as another factor contributing to a higher activity. The higher electrical conductivity in CNT-containing samples could also be effective in the enhancement of the electrochemical catalytic performance of the 15s-treated sample (and also other samples). It is observed that, by increasing the microwave irradiation time, especially after 60 s, the catalytic

activity of the nanofibers steps down. The significance of incorporation of the CNTs into the carbon nanofibers, besides enhancement of the catalytic performance, is explained to be their effectiveness in increasing the redox cycling capability. This is achieved through deducing the stress applied on the fibers by electrolyte movements during cycling [113]. Furthermore, the reinforcing effect of CNTs allows to construct a more strong and durable catalyst layer for different applications like fuel cell, which will be reported in the future work.

3.6. Fuel cell testing

In order to prepare PEMFC electrodes, completely processed carbon nanofibers were manually crushed by a mortar and pestle. The as-crushed fibers are represented in the TEM image in Fig.43a. The morphology of the crushed nanofibers in the MEA, binded with the Nafion solution is also illustrated in Fig.43b. To observe the exact thickness of the catalyst layer over the carbon paper in the MEAs, the same amount of catalyst layer (which is applied over carbon paper) was coated on an aluminum foil to observe the cross-section of the catalyst layer (Fig.43c). According to the cross-sectional image of the catalyst layer, it was observed that the thickness of catalyst layer was about 30-50 μm . It could be observed in the SEM images that there is a relatively balanced compactness and porosity in the catalyst layers and carbon nanofibers have been well distributed and created a good contact between each other.

Fig. 44 demonstrates polarization curves of the microwave reduced samples (with and without CNT) after PEMFC measurement at 70°C. The cell performances of the MEAs showed that, all the samples represented slightly low performance. Because, in many of studies or in the commercial PEMFCs, the electrodes are prepared from carbon supports with Pt particles decorated over the surface. However, the Pt particles in our samples are distributed throughout the fibers (inside and outside) and thus, there are lower accessible active regions.

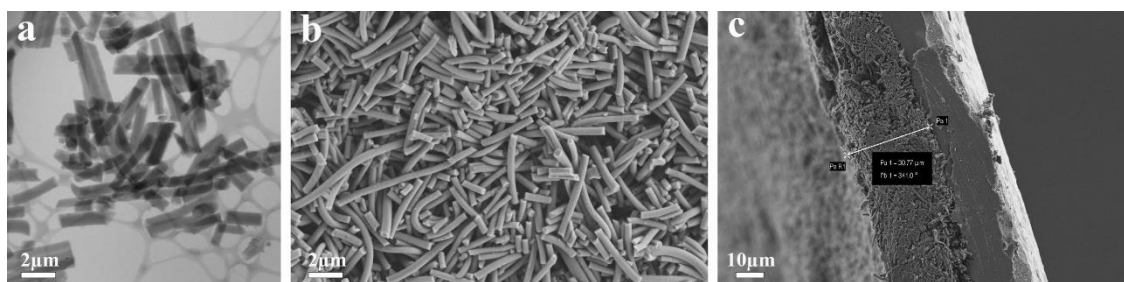


Fig.43. (a) TEM image of the crushed carbon nanofibers to be used in the fuel cell electrodes, (b) SEM image of the surface of fuel cell cathode catalyst layer and (c) SEM image from the intersection of the fuel cell cathode catalyst layer.

Also, it could be argued that, by some additional manipulations and optimizations the PEMFC performance of these samples could be improved. Comparing the CNT-containing and CNT-free samples, it could be observed that, the overall PEMFC performance of the CNT-containing samples are improved with respect to their CNT-free counterparts, both in lower and higher current density regions. This could be associated to higher charge conductivity and also smaller Pt nuclei over the CNT-containing samples.

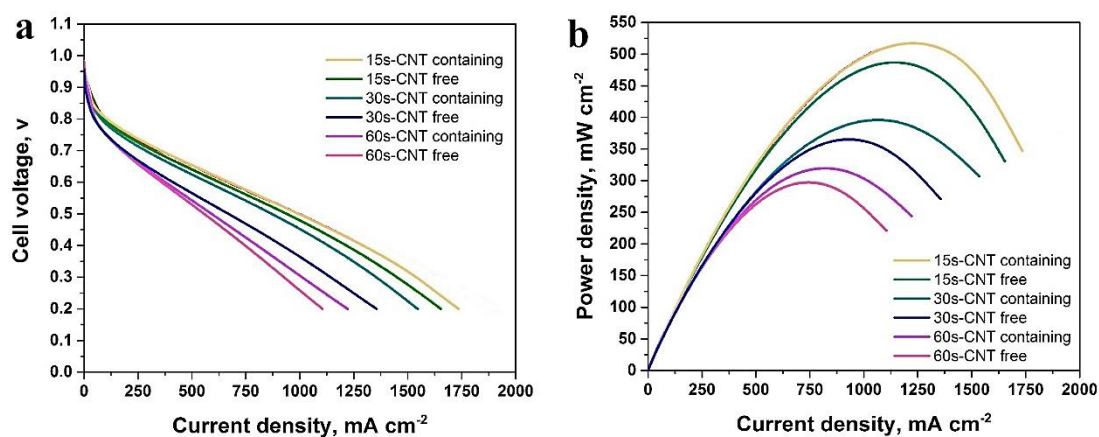


Fig.44. Single PEMFC a) performance b) power density output curves of the microwave treated samples at various irradiation times.

The highest PEMFC performance between microwave treated samples was achieved for 15s treated CNT-containing sample. It is observed that, the PEMFC results are in a good accordance with the CV catalytic performances of the samples (Table 3). Power density variations of the samples are also represented in Fig.44b. The maximum power density of 500 mWcm^{-2} was achieved for 15s microwave treated CNT-containing sample. It is clear from the power density curves that, by increasing the microwave irradiation time, the maximum power densities decrease.

4. Conclusions

An in-situ microwave-assisted synthesis method was reported for scalable production of CNF-supported Pt particles from a polymeric source with a precise particle size control. The CNF-supported Pt was synthesized through electrospinning of P(AN-*co*-nVP) copolymer solution in DMF containing 20 wt.% PtCl₂ as Pt source and subsequent microwave reduction in 5 vol.% hydrazine hydrate solution and carbonization at 800 °C. The copolymer structure was designed in way that it could template the dispersion of Pt precursors (chemically coordinated with polar groups of bifunctional monomers) in a random manner. Subsequently, a rapid microwave-assisted reduction procedure was implicated to locally reduce the Pt precursor, without permitting them to aggregate. The existence of the vinyl terminal groups polymerized with AN unit was verified from the FTIR and ¹H-NMR results. Furthermore, the ¹H-NMR results revealed a “random” distribution of nVP bifunctional groups within the PAN supporting polymer. The optimum carbonization condition for the nanofibers was achieved at 800 °C. Since the Pt nanoparticles were entrapped within a matrix, their surface energy was satisfied and therefore the sintering phenomena was considerably avoided, even during subsequent high-temperature carbonization procedure (at 800 °C). It was observed that a rapid microwave reduction is capable of generating a significantly uniform nucleation and distribution of Pt nanoparticles, throughout the nanofibers with average sizes even less than 1 nm. The minimum average particle size was obtained after 15s irradiation, which is 1.751 nm for CNT-free sample and 0.862 nm for CNT-containing ones with even narrow size distribution. The smaller particle size achieved in the case of CNT-containing CNFs, compared to their CNT-free counterparts, could be associated to the dominance of an effective Pt nucleation rather than growth, due to a higher microwave absorptivity in CNT-containing samples. In all samples, the mean Pt particle size was observed to increase as a function of microwave irradiation time. The catalytic activity of the samples measured by CV test demonstrated the best ECSA value for the 30s treated CNT-free sample despite the smaller Pt particle size in the 15s treated one. This observation was attributed to the lower accessibility of the Pt particles to the electrolyte solution. However, in the case of CNT-containing samples the highest ECSA value was observed for 15s microwave irradiated sample, which was assumed to be associated with the considerable number of Pt nucleated near the surface of this sample and also higher

porous nanofibers (due to the presence of CNTs) and a higher electrical conductivity. Moreover, the overall PEMFC performance of the CNT-containing samples is improved compared to their CNT-free counterparts, due to higher charge conductivity and also a high frequency of smaller Pt nuclei over the CNT-containing samples. The highest fuel cell performance and the maximum power density of 500 mWcm^{-2} was achieved for the 15s microwave treated CNT-containing sample.

5. References

- [1] Zhaolin Liu, Xing Yi Ling, and Xiaodi Su, and Jim Yang Lee, “Carbon-Supported Pt and PtRu Nanoparticles as Catalysts for a Direct Methanol Fuel Cell,” 2004.
- [2] J. M. Planeix *et al.*, “Application of Carbon Nanotubes as Supports in Heterogeneous Catalysis,” *J. Am. Chem. Soc.*, vol. 116, no. 17, pp. 7935–7936, Aug. 1994.
- [3] E. Antolini, “Carbon supports for low-temperature fuel cell catalysts,” *Appl. Catal. B Environ.*, vol. 88, no. 1, pp. 1–24, 2009.
- [4] T. S. Ahmadi, Z. L. Wang, T. C. Green, A. Henglein, and M. A. El-Sayed, “Shape-Controlled Synthesis of Colloidal Platinum Nanoparticles,” *Science (80)*, vol. 272, no. 5270, 1996.
- [5] Mustafa M. Demir *et al.*, “Palladium Nanoparticles by Electrospinning from Poly(acrylonitrile-co-acrylic acid)–PdCl₂ Solutions. Relations between Preparation Conditions, Particle Size, and Catalytic Activity,” 2004.
- [6] Kenji Okitsu, Akihiko Yue, and Shuji Tanabe, and H. Matsumoto, “Sonochemical Preparation and Catalytic Behavior of Highly Dispersed Palladium Nanoparticles on Alumina,” 2000.
- [7] Toshiyuki Fujimoto, Shin-ya Terauchi, Hiroyuki Umehara, and Isao Kojima, and W. Henderson, “Sonochemical Preparation of Single-Dispersion Metal Nanoparticles from Metal Salts,” 2001.
- [8] Z. Liu *et al.*, “Synthesis and characterization of PtRu/C catalysts from microemulsions and emulsions,” *J. Mater. Chem.*, vol. 12, no. 8, pp. 2453–2458, Jul. 2002.
- [9] Q. Z. and L. A. Archer*, “Poly(ethylene oxide)/Silica Nanocomposites: Structure and Rheology,” 2002.
- [10] G. Schmidt and M. M. Malwitz, “Properties of polymer–nanoparticle composites,” *Curr. Opin. Colloid Interface Sci.*, vol. 8, no. 1, pp. 103–108, Mar. 2003.

- [11] Y. L. and and M. A. El-Sayed, “The Effect of Stabilizers on the Catalytic Activity and Stability of Pd Colloidal Nanoparticles in the Suzuki Reactions in Aqueous Solution[†],” 2001.
- [12] T. Teranishi, R. Kurita, and M. Miyake, “Shape Control of Pt Nanoparticles,” *J. Inorg. Organomet. Polym.*, vol. 10, no. 3, pp. 145–156, 2000.
- [13] M. C. and and Y. Xing*, “Polymer-Mediated Synthesis of Highly Dispersed Pt Nanoparticles on Carbon Black,” 2005.
- [14] H. Wang, X. Qiao, J. Chen, X. Wang, and S. Ding, “Mechanisms of PVP in the preparation of silver nanoparticles,” *Mater. Chem. Phys.*, vol. 94, no. 2–3, pp. 449–453, Dec. 2005.
- [15] A. B. R. Mayer and J. E. Mark, “Transition metal nanoparticles protected by amphiphilic block copolymers as tailored catalyst systems,” *Colloid Polym. Sci.*, vol. 275, no. 4, pp. 333–340, Apr. 1997.
- [16] Yugang Sun, Brian Mayers, and Thurston Herricks, and Y. Xia, “Polyol Synthesis of Uniform Silver Nanowires: A Plausible Growth Mechanism and the Supporting Evidence,” 2003.
- [17] T. Teranishi, M. Hosoe, and T. Tanaka, and M. Miyake*, “Size Control of Monodispersed Pt Nanoparticles and Their 2D Organization by Electrophoretic Deposition,” 1999.
- [18] N. D. Luong, Y. Lee, and J.-D. Nam, “Highly-loaded silver nanoparticles in ultrafine cellulose acetate nanofibrillar aerogel,” *Eur. Polym. J.*, vol. 44, no. 10, pp. 3116–3121, Oct. 2008.
- [19] S. Sundarrajan and S. Ramakrishna, “Fabrication of nanocomposite membranes from nanofibers and nanoparticles for protection against chemical warfare stimulants,” *J. Mater. Sci.*, vol. 42, no. 20, pp. 8400–8407, Aug. 2007.
- [20] P. S. Roy, J. Bagchi, and S. K. Bhattacharya, “Size-controlled synthesis and characterization of polyvinyl alcohol coated palladium nanoparticles,” *Transit. Met. Chem.*, vol. 34, no. 4, pp. 447–453, May 2009.

- [21] Eric Formo, Eric Lee, and Dean Campbell, and Younan Xia, "Functionalization of Electrospun TiO₂ Nanofibers with Pt Nanoparticles and Nanowires for Catalytic Applications," 2008.
- [22] G.-Y. Oh, Y.-W. Ju, H.-R. Jung, and W.-J. Lee, "Preparation of the novel manganese-embedded PAN-based activated carbon nanofibers by electrospinning and their toluene adsorption," *J. Anal. Appl. Pyrolysis*, vol. 81, no. 2, pp. 211–217, 2008.
- [23] L. Ji and X. Zhang, "Manganese oxide nanoparticle-loaded porous carbon nanofibers as anode materials for high-performance lithium-ion batteries," *Electrochem. commun.*, vol. 11, no. 4, pp. 795–798, Apr. 2009.
- [24] H. Hou and D. H. Reneker, "Carbon Nanotubes on Carbon Nanofibers: A Novel Structure Based on Electrospun Polymer Nanofibers," *Adv. Mater.*, vol. 16, no. 1, pp. 69–73, Jan. 2004.
- [25] N. T. Xuyen, H. K. Jeong, G. Kim, K. P. So, K. H. An, and Y. H. Lee, "Hydrolysis-induced immobilization of Pt(acac)₂ on polyimide-based carbon nanofiber mat and formation of Pt nanoparticles," *J. Mater. Chem.*, vol. 19, no. 9, p. 1283, 2009.
- [26] L. Chen, S. Hong, X. Zhou, Z. Zhou, and H. Hou, "Novel Pd-carrying composite carbon nanofibers based on polyacrylonitrile as a catalyst for Sonogashira coupling reaction," 2008.
- [27] J. Yu and T. Liu, "Preparation of a fibrous catalyst containing palladium nanoparticles and its application in hydrogenation of olefins," *Polym. Compos.*, vol. 29, no. 12, pp. 1346–1349, Dec. 2008.
- [28] K. H. Hong, "Preparation and properties of electrospun poly(vinyl alcohol)/silver fiber web as wound dressings," *Polym. Eng. Sci.*, vol. 47, no. 1, pp. 43–49, Jan. 2007.
- [29] G. Riess, "Micellization of block copolymers," *Prog. Polym. Sci.*, vol. 28, no. 7, pp. 1107–1170, Jul. 2003.
- [30] Y. Shao, Y.-G. Jia, C. Shi, J. Luo, and X. X. Zhu, "Block and Random Copolymers Bearing Cholic Acid and Oligo(ethylene glycol) Pendant Groups: Aggregation,

- Thermosensitivity, and Drug Loading,” *Biomacromolecules*, vol. 15, no. 5, pp. 1837–1844, May 2014.
- [31] Z. Li *et al.*, “Facile synthesis of single-crystal and controllable sized silver nanoparticles on the surfaces of polyacrylonitrile nanofibres,” *Nanotechnology*, vol. 17, no. 3, pp. 917–920, Feb. 2006.
- [32] Q. Zhang, D. Wu, S. Qi, Z. Wu, X. Yang, and R. Jin, “Preparation of ultra-fine polyimide fibers containing silver nanoparticles via in situ technique,” *Mater. Lett.*, vol. 61, no. 19–20, pp. 4027–4030, Aug. 2007.
- [33] A. L. Harreus *et al.*, “2-Pyrrolidone,” in *Ullmann’s Encyclopedia of Industrial Chemistry*, Weinheim, Germany: Wiley-VCH Verlag GmbH & Co. KGaA, 2011.
- [34] M. Demir, I. Yilgor, E. Yilgor, and B. Erman, “Electrospinning of polyurethane fibers,” *Polymer (Guildf.)*, vol. 43, no. 11, pp. 3303–3309, 2002.
- [35] S. Litster and G. McLean, “PEM fuel cell electrodes,” *J. Power Sources*, vol. 130, no. 1, pp. 61–76, 2004.
- [36] L. I. Şanlı, V. Bayram, B. Yarar, S. Ghobadi, and S. A. Gürsel, “Development of graphene supported platinum nanoparticles for polymer electrolyte membrane fuel cells: Effect of support type and impregnation–reduction methods,” *Int. J. Hydrogen Energy*, vol. 41, no. 5, pp. 3414–3427, 2016.
- [37] M. Y. Wang *et al.*, “Ethanol electro-oxidation with Pt and Pt–Ru catalysts supported on carbon nanotubes,” *Carbon N. Y.*, vol. 42, no. 15, pp. 3257–3260, Jan. 2004.
- [38] K. B. Male, S. Hrapovic, Y. Liu, D. Wang, and J. H. Luong, “Electrochemical detection of carbohydrates using copper nanoparticles and carbon nanotubes,” *Anal. Chim. Acta*, vol. 516, no. 1–2, pp. 35–41, Jul. 2004.
- [39] Y. D. Li, L. Q. Li, H. W. Liao, and H. R. Wang, “Preparation of pure nickel, cobalt, nickel–cobalt and nickel–copper alloys by hydrothermal reduction,” *J. Mater. Chem.*, vol. 9, no. 10, pp. 2675–2677, 1999.
- [40] J. van Wonterghem, S. Mørup, C. J. W. Koch, S. W. Charles, and S. Wells,

- “Formation of ultra-fine amorphous alloy particles by reduction in aqueous solution,” *Nature*, vol. 322, no. 6080, pp. 622–623, Aug. 1986.
- [41] L. M. Bronstein *et al.*, “Interaction of metal compounds with ‘double-hydrophilic’ block copolymers in aqueous medium and metal colloid formation,” *Inorganica Chim. Acta*, vol. 280, no. 1–2, pp. 348–354, Oct. 1998.
- [42] S. N. Sidorov *et al.*, “Stabilization of Metal Nanoparticles in Aqueous Medium by Polyethyleneoxide–Polyethyleneimine Block Copolymers,” *J. Colloid Interface Sci.*, vol. 212, no. 2, pp. 197–211, Apr. 1999.
- [43] Gyeong-Man Kim *et al.*, “One-Dimensional Arrangement of Gold Nanoparticles by Electrospinning,” 2005.
- [44] H. K. Lee, E. H. Jeong, C. K. Baek, and J. H. Youk, “One-step preparation of ultrafine poly(acrylonitrile) fibers containing silver nanoparticles,” *Mater. Lett.*, vol. 59, no. 23, pp. 2977–2980, Oct. 2005.
- [45] M. Möller, J. P. Spatz, and A. Roescher, “Gold nanoparticles in micellar poly(styrene)-b-poly(ethylene oxide) films—size and interparticle distance control in monoparticulate films,” *Adv. Mater.*, vol. 8, no. 4, pp. 337–340, Apr. 1996.
- [46] Janne Raula *et al.*, “Synthesis of Gold Nanoparticles Grafted with a Thermoresponsive Polymer by Surface-Induced Reversible-Addition-Fragmentation Chain-Transfer Polymerization,” 2003.
- [47] R. B. Grubbs, “Roles of Polymer Ligands in Nanoparticle Stabilization,” *Polym. Rev.*, vol. 47, no. 2, pp. 197–215, Apr. 2007.
- [48] J. F. Ciebien, R. T. Clay, B. H. Sohn, R. E. Cohen, T. Yamamoto, and R. E. Cohen, “Brief review of metal nanoclusters in block copolymer films,” *New J. Chem.*, vol. 22, no. 7, pp. 685–691, Jan. 1998.
- [49] S. Mo, J. P. Spatz, M. Mo, T. Aberle, rgen Schmidt, and W. Burchard, “Solution Behavior of Poly(styrene)-block-poly(2-vinylpyridine) Micelles Containing Gold Nanoparticles.”

- [50] M. R. Bockstaller, R. A. Mickiewicz, and E. L. Thomas, "Block Copolymer Nanocomposites: Perspectives for Tailored Functional Materials," *Adv. Mater.*, vol. 17, no. 11, pp. 1331–1349, Jun. 2005.
- [51] Limin Qi, and Helmut Cölfen, and M. Antonietti, "Synthesis and Characterization of CdS Nanoparticles Stabilized by Double-Hydrophilic Block Copolymers," 2000.
- [52] A. K. Shukla, K. V. Ramesh, R. Manoharan, P. R. Sarode, and S. Vasudevan, "Preparation and Characterization of Platinized-Carbon Hydrogen Anodes for Alkali and Acid Fuel Cells," *Berichte der Bunsengesellschaft für Phys. Chemie*, vol. 89, no. 12, pp. 1261–1267, Dec. 1985.
- [53] W.-J. Jin, H. K. Lee, E. H. Jeong, W. H. Park, and J. H. Youk, "Preparation of Polymer Nanofibers Containing Silver Nanoparticles by Using Poly(N-vinylpyrrolidone)," *Macromol. Rapid Commun.*, vol. 26, no. 24, pp. 1903–1907, Dec. 2005.
- [54] T. S. and and P. Alexandridis*, "Single-Step Synthesis and Stabilization of Metal Nanoparticles in Aqueous Pluronic Block Copolymer Solutions at Ambient Temperature," 2004.
- [55] T. Teranishi, I. Kiyokawa, and M. Miyake, "Synthesis of Monodisperse Gold Nanoparticles Using Linear Polymers as Protective Agents," *Adv. Mater.*, vol. 10, no. 8, pp. 596–599, May 1998.
- [56] C. Lai, Q. Guo, X.-F. Wu, D. H. Reneker, and H. Hou, "Growth of carbon nanostructures on carbonized electrospun nanofibers with palladium nanoparticles," *Nanotechnology*, vol. 19, no. 19, p. 195303, May 2008.
- [57] G. Taylor, "Electrically Driven Jets," *Proc. R. Soc. London A Math. Phys. Eng. Sci.*, vol. 313, no. 1515, 1969.
- [58] H. Fong, I. Chun, and D. Reneker, "Beaded nanofibers formed during electrospinning," *Polymer (Guildf.)*, vol. 40, no. 16, pp. 4585–4592, Jul. 1999.
- [59] J. Deitzel, J. Kleinmeyer, D. Harris, and N. Beck Tan, "The effect of processing variables on the morphology of electrospun nanofibers and textiles," *Polymer*

- (*Guildf.*), vol. 42, no. 1, pp. 261–272, Jan. 2001.
- [60] N. Zhu and X. Che, “Biofabrication of Tissue Scaffolds,” in *Advances in Biomaterials Science and Biomedical Applications*, InTech, 2013.
- [61] S. I. Marras, K. P. Kladi, I. Tsivintzelis, I. Zuburtikudis, and C. Panayiotou, “Biodegradable polymer nanocomposites: The role of nanoclays on the thermomechanical characteristics and the electrospun fibrous structure,” *Acta Biomater.*, vol. 4, no. 3, pp. 756–765, May 2008.
- [62] P. Gupta and G. L. Wilkes, “Some investigations on the fiber formation by utilizing a side-by-side bicomponent electrospinning approach,” *Polymer (Guildf.)*, vol. 44, no. 20, pp. 6353–6359, Sep. 2003.
- [63] J. S. Lee *et al.*, “Role of molecular weight of atactic poly(vinyl alcohol) (PVA) in the structure and properties of PVA nanofabric prepared by electrospinning,” *J. Appl. Polym. Sci.*, vol. 93, no. 4, pp. 1638–1646, Aug. 2004.
- [64] S. Zhao, X. Wu, L. Wang, and Y. Huang, “Electrospinning of ethyl-cyanoethyl cellulose/tetrahydrofuran solutions,” *J. Appl. Polym. Sci.*, vol. 91, no. 1, pp. 242–246, Jan. 2004.
- [65] Silke Megelski, Jean S. Stephens, and D. Bruce Chase, and John F. Rabolt, “Micro- and Nanostructured Surface Morphology on Electrospun Polymer Fibers,” 2002.
- [66] V. M. Vishnyakov, “Proton exchange membrane fuel cells,” *Vacuum*, vol. 80, no. 10, pp. 1053–1065, Aug. 2006.
- [67] G. J. K. Acres *et al.*, “Electrocatalysts for fuel cells,” *Catal. Today*, vol. 38, no. 4, pp. 393–400, Nov. 1997.
- [68] A. T. Haug *et al.*, “Using Sputter Deposition to Increase CO Tolerance in a Proton-Exchange Membrane Fuel Cell,” *J. Electrochem. Soc.*, vol. 149, no. 7, p. A868, Jul. 2002.
- [69] Z. He, J. Chen, D. Liu, H. Tang, W. Deng, and Y. Kuang, “Deposition and electrocatalytic properties of platinum nanoparticles on carbon nanotubes for

- methanol electrooxidation,” *Mater. Chem. Phys.*, vol. 85, no. 2–3, pp. 396–401, Jun. 2004.
- [70] Y. Shao, J. Sui, G. Yin, and Y. Gao, “Nitrogen-doped carbon nanostructures and their composites as catalytic materials for proton exchange membrane fuel cell,” *Appl. Catal. B Environ.*, vol. 79, no. 1, pp. 89–99, Feb. 2008.
- [71] W. Li, M. Waje, Z. Chen, P. Larsen, and Y. Yan, “Platinum nanoparticles supported on stacked-cup carbon nanofibers as electrocatalysts for proton exchange membrane fuel cell,” *Carbon N. Y.*, vol. 48, no. 4, pp. 995–1003, Apr. 2010.
- [72] Wenzhen Li, Xin Wang, Zhongwei Chen, and Mahesh Waje, and Y. Yan*, “Carbon Nanotube Film by Filtration as Cathode Catalyst Support for Proton-Exchange Membrane Fuel Cell,” 2005.
- [73] S. M. Andersen *et al.*, “Durability of carbon nanofiber (CNF) & carbon nanotube (CNT) as catalyst support for Proton Exchange Membrane Fuel Cells,” *Solid State Ionics*, vol. 231, pp. 94–101, Feb. 2013.
- [74] Gwen Lawrie *et al.*, “Interactions between Alginate and Chitosan Biopolymers Characterized Using FTIR and XPS,” 2007.
- [75] W. Li, B. F. Pierce, N. Scharnagl, C. Wischke, A. L. Sisson, and A. Lendlein, “Influence of co-monomer ratio on the chemical properties and cytotoxicity of poly[acrylonitrile-co-(N-vinylpyrrolidone)] nanoparticles,” *J. Appl. Biomater. Funct. Mater.*, vol. 10, no. 3, pp. 308–314, 2012.
- [76] H. J. Harwood and W. M. Ritchey, “The characterization of sequence distribution in copolymers,” *J. Polym. Sci. Part B Polym. Lett.*, vol. 2, no. 6, pp. 601–607, Jun. 1964.
- [77] M. S. Dresselhaus, A. Jorio, and R. Saito, “Characterizing Graphene, Graphite, and Carbon Nanotubes by Raman Spectroscopy,” *Annu. Rev. Condens. Matter Phys.*, vol. 1, no. 1, pp. 89–108, Aug. 2010.
- [78] C. Kim, J.-S. Kim, W.-J. Lee, H.-S. Kim, D. D. Edie, and K.-S. Yang, “Preparations of PAN-based Activated Carbon Nanofiber Web Electrode by

- Electrostatic Spinning and Their Applications to EDLC,” *J. Korean Electrochem. Soc.*, vol. 5, no. 3, pp. 117–124, Aug. 2002.
- [79] N. Kaerkitcha, S. Chuangchote, and T. Sagawa, “Control of physical properties of carbon nanofibers obtained from coaxial electrospinning of PMMA and PAN with adjustable inner/outer nozzle-ends,” *Nanoscale Res. Lett.*, vol. 11, no. 1, p. 186, Dec. 2016.
- [80] S. H. Joo *et al.*, “Ordered nanoporous arrays of carbon supporting high dispersions of platinum nanoparticles,” *Nature*, vol. 412, no. 6843, pp. 169–172, Jul. 2001.
- [81] F. Dumestre *et al.*, “Shape Control of Thermodynamically Stable Cobalt Nanorods through Organometallic Chemistry,” *Angew. Chemie*, vol. 114, no. 22, pp. 4462–4465, Nov. 2002.
- [82] P. Loof, “Rapid Sintering in NO of Nanometer-Sized Pt Particles on γ -Al₂O₃ Observed by CO Temperature-Programmed Desorption and Transmission Electron Microscopy,” *J. Catal.*, vol. 144, no. 1, pp. 60–76, Nov. 1993.
- [83] C. R. A. Catlow, W. C. Mackrodt, M. J. Norgett, and A. M. Stoneham, “The basic atomic processes of corrosion II. Defect structures and cation transport in transition-metal oxides,” *Philos. Mag. A*, vol. 40, no. 2, pp. 161–172, Aug. 1979.
- [84] P. Forzatti and L. Lietti, “Catalyst deactivation,” *Catal. Today*, vol. 52, no. 2, pp. 165–181, 1999.
- [85] M. Herberhold, E. O. Fischer, and H. Werner, *Specific aspects*. Elsevier, 1974.
- [86] M. C. Smith, J. A. Gilbert, J. R. Mawdsley, S. Seifert, and D. J. Myers, “In Situ Small-Angle X-ray Scattering Observation of Pt Catalyst Particle Growth During Potential Cycling,” *J. Am. Chem. Soc.*, vol. 130, no. 26, pp. 8112–8113, Jul. 2008.
- [87] T. KAWAGUCHI, W. SUGIMOTO, Y. MURAKAMI, and Y. TAKASU, “Particle growth behavior of carbon-supported Pt, Ru, PtRu catalysts prepared by an impregnation reductive-pyrolysis method for direct methanol fuel cell anodes,” *J. Catal.*, vol. 229, no. 1, pp. 176–184, Jan. 2005.
- [88] R. BAKER, “Catalytic oxidation of graphite by platinum and palladium,” *J.*

- Catal.*, vol. 41, no. 1, pp. 22–29, Jan. 1976.
- [89] Y. Li, W. Gao, L. Ci, C. Wang, and P. M. Ajayan, “Catalytic performance of Pt nanoparticles on reduced graphene oxide for methanol electro-oxidation,” *Carbon N. Y.*, vol. 48, no. 4, pp. 1124–1130, 2010.
- [90] A. K. Gupta, D. K. Paliwal, and P. Bajaj, “Acrylic Precursors for Carbon Fibers,” *Polym. Rev.*, vol. 31, no. 1, pp. 1–89, Feb. 1991.
- [91] P. Zorabedian, F. Adar, P. M. Bell, and J. A. Xu, “Measurement of local stress in laser-recrystallized lateral epitaxial silicon films over silicon dioxide using Raman scattering,” *Appl. Phys. Lett.*, vol. 43, no. 2, pp. 177–179, Jul. 1983.
- [92] B. Seger and P. V. Kamat, “Electrocatalytically Active Graphene-Platinum Nanocomposites. Role of 2-D Carbon Support in PEM Fuel Cells,” *J. Phys. Chem. C*, vol. 113, no. 19, pp. 7990–7995, May 2009.
- [93] F.-R. F. Fan and A. J. Bard, “In Situ Scanning Tunneling Microscopy of Polycrystalline Platinum Electrodes under Potential Control,” *J. Electrochem. Soc.*, vol. 136, no. 11, p. 3216, Nov. 1989.
- [94] Guo-Qiang Lu, and Alechia Crown, and A. Wieckowski*, “Formic Acid Decomposition on Polycrystalline Platinum and Palladized Platinum Electrodes,” 1999.
- [95] X. Yu and S. Ye, “Recent advances in activity and durability enhancement of Pt/C catalytic cathode in PEMFC: Part II: Degradation mechanism and durability enhancement of carbon supported platinum catalyst,” *J. Power Sources*, vol. 172, no. 1, pp. 145–154, 2007.
- [96] M. Okamoto, T. Fujigaya, and N. Nakashima, “Design of an Assembly of Poly(benzimidazole), Carbon Nanotubes, and Pt Nanoparticles for a Fuel-Cell Electrocatalyst with an Ideal Interfacial Nanostructure,” *Small*, vol. 5, no. 6, pp. 735–740, Mar. 2009.
- [97] Z. Qi and A. Kaufman, “Low Pt loading high performance cathodes for PEM fuel cells,” *J. Power Sources*, vol. 113, no. 1, pp. 37–43, Jan. 2003.

- [98] S. Gamburgzev and A. J. Appleby, "Recent progress in performance improvement of the proton exchange membrane fuel cell (PEMFC)," *J. Power Sources*, vol. 107, no. 1, pp. 5–12, 2002.
- [99] N. K. Sahu, A. Prakash, and D. Bahadur, "Role of different platinum precursors on the formation and reaction mechanism of FePt nanoparticles and their electrocatalytic performance towards methanol oxidation," *Dalt. Trans.*, vol. 43, no. 12, pp. 4892–4900, Feb. 2014.
- [100] A. de la Hoz, Á. Díaz-Ortiz, and A. Moreno, "Microwaves in organic synthesis. Thermal and non-thermal microwave effects," *Chem. Soc. Rev.*, vol. 34, no. 2, pp. 164–178, 2005.
- [101] W. S. Khan, R. Asmatulu, and M. M. Eltabey, "Dielectric Properties of Electrospun PVP and PAN Nanocomposite Fibers at Various Temperatures," *J. Nanotechnol. Eng. Med.*, vol. 1, no. 4, p. 41017, 2010.
- [102] A. K. Singh and V. S. Raykar, "Microwave synthesis of silver nanofluids with polyvinylpyrrolidone (PVP) and their transport properties," *Colloid Polym. Sci.*, vol. 286, no. 14–15, pp. 1667–1673, Dec. 2008.
- [103] F. Qin and C. Brosseau, "A review and analysis of microwave absorption in polymer composites filled with carbonaceous particles," *J. Appl. Phys.*, vol. 111, no. 6, p. 61301, Mar. 2012.
- [104] H. J. Han, Y. N. Chen, and Z. J. Wang, "Effect of microwave irradiation on reduction of graphene oxide films," *RSC Adv.*, vol. 5, no. 113, pp. 92940–92946, Oct. 2015.
- [105] F. Ko *et al.*, "Electrospinning of Continuous Carbon Nanotube-Filled Nanofiber Yarns," *Adv. Mater.*, vol. 15, no. 14, pp. 1161–1165, Jul. 2003.
- [106] Haoqing Hou *et al.*, "Electrospun Polyacrylonitrile Nanofibers Containing a High Concentration of Well-Aligned Multiwall Carbon Nanotubes," 2005.
- [107] A. Schlange, A. R. dos Santos, U. Kunz, and T. Turek, "Continuous preparation of carbon-nanotube-supported platinum catalysts in a flow reactor directly heated by electric current," *Beilstein J. Org. Chem.*, vol. 7, no. 1, pp. 1412–1420, Oct.

2011.

- [108] M. G. Mason, “Electronic structure of supported small metal clusters,” *Phys. Rev. B*, vol. 27, no. 2, p. 748, Jan. 1983.
- [109] Yael Dror, Wael Salalha, Rafail L. Khalfin, Yachin Cohen, and Alexander L. Yarin, and E. Zussman, “Carbon Nanotubes Embedded in Oriented Polymer Nanofibers by Electrospinning,” 2003.
- [110] T. Maitra, S. Sharma, A. Srivastava, Y.-K. Cho, M. Madou, and A. Sharma, “Improved graphitization and electrical conductivity of suspended carbon nanofibers derived from carbon nanotube/polyacrylonitrile composites by directed electrospinning,” *Carbon N. Y.*, vol. 50, no. 5, pp. 1753–1761, 2012.
- [111] S. Jagannathan, “Process, structure and electrochemical properties of carbon nanotube containing films and fibers,” 2009.
- [112] H. Pan, J. Li, and Y. P. Feng, “Carbon Nanotubes for Supercapacitor,” *Nanoscale Res. Lett.*, vol. 5, no. 3, pp. 654–668, Mar. 2010.
- [113] V. Kumar, S. Kalia, and H. C. Swart, Eds., *Conducting Polymer Hybrids*. Cham: Springer International Publishing, 2017.